2016

Single-Molecule Studies Of tRNA Dynamics During Ongoing Translation

Ryan Jamiolkowski
University of Pennsylvania, ryanjam@mail.med.upenn.edu

Single-Molecule Studies Of tRNA Dynamics During Ongoing Translation

Abstract
The pre-translocation complex of the ribosome can undergo spontaneous fluctuations of mRNA and tRNAs between classical and hybrid states, and occupation of the hybrid tRNA positions has been proposed to precede translocation. The classic and hybrid state tRNA positions been extensively characterized when the ribosome is stalled along the messenger RNA by either the absence or the delayed addition of elongation factor G (EF-G), or by the presence of antibiotics or GTP analogs that block translocation. Surprisingly, during multiple ongoing elongation cycles when both EF-G and ternary complexes are present, we found that tRNA positions in PRE complex ribosome do not fluctuate. Instead, they adopt a stationary intermediate structure between the stalled classical and hybrid tRNA positions, as indicated by single molecule fluorescence resonance energy transfer (FRET) between adjacent tRNAs and between A-site tRNA and ribosomal protein L11. These results indicate that EF-G promotes the formation of an intermediate structure during ongoing translation.

smFRET experiments using labeled EF-G at those concentrations requires zero-mode waveguides (ZMWs), arrays of nanoscale holes in a thin metal film that confine the observation volume to reduce prohibitive background fluorescence. However, the need for specialized nanofabrication equipment has precluded their widespread adoption by the biochemical community. In contrast, nanosphere lithography uses the self-assembly of polystyrene beads into a hexagonal array, forming a natural lithographic mask for the deposition of metallic posts in the interstices between beads, followed by a different metal cladding around the posts and dissolution of the posts to leave a well array. The cross-sectional size of those interstices (and thus subsequent posts and wells) can be finely tuned by fusing the beads at the polystyrene glass transition temperature. That bead lattice serves as a template for creating sub-wavelength ZMWs with little specialized equipment and at a low cost, enabling wide-scale adoption.

Degree Type
Dissertation

Degree Name
Doctor of Philosophy (PhD)

Graduate Group
Bioengineering

First Advisor
Yale E. Goldman

Subject Categories
Biochemistry | Biomedical | Biophysics

SINGLE-MOLECULE STUDIES OF tRNA DYNAMICS DURING ONGOING TRANSLATION

Ryan Jamiolkowski

A DISSERTATION

in

Bioengineering

Presented to the Faculties of the University of Pennsylvania

in

Partial Fulfillment of the Requirements for the

Degree of Doctor of Philosophy

2016

Supervisor of Dissertation

_____

Dr. Yale E. Goldman, Professor of Physiology

Graduate Group Chairperson

_____

Dr. Jason Burdick, Professor of Bioengineering

Dissertation Committee:

Dr. Andrew Tsourkas, Professor of Bioengineering

Dr. Robert Doms, Professor of Pathology and Laboratory Medicine

Dr. Arjun Raj, Professor of Bioengineering

Acknowledgements

Over the course of my time in his lab, Prof. Yale E. Goldman has been an outstanding advisor. His ability to bridge hypothesis-driven basic science with technical prowess in developing optical, electronic, and computational techniques (without losing sight of the big picture) made learning from him a uniquely valuable experience. He has also been an encouraging mentor, making the lab a welcoming home.

Prof. Barry Cooperman has been an invaluable collaborator, whose encyclopedic knowledge of the ribosome field and incisive questioning during lab meetings has played a major role in the direction of these projects. His expertise in the purification of ribosomes and components of the translation machinery have also been indispensable.

I would also like to thank Dr. Jody Dantzig-Brody tremendously for her constant support and encouragement, and always being a source of advice during stressful moments. Without her support, the whole endeavor would have been much more difficult.

Prof. Chunlai Chen was an amazing mentor in my early days in the lab; in addition to teaching me everything I know about smFRET, he continues to this day to be an indispensable source of advice, responding to any emails within a few hours even though he's currently engrossed in building up his own lab in China

Prof. Shawn Pfeil has been an amazing collaborator; our frequent meetings to discuss progress always leave me with great new ideas to try. His perspective as a physicist has been an enormous benefit, and I've enjoyed becoming his friend while working together.

Dr. Vijay Singh has been a true pleasure to work with over the past year, and I am happy to know that the projects we started together are being left in his extremely capable hands. I am very excited to see where he takes them.

Kevin Chen and Alyssa Tate are extremely capable and hardworking undergraduates who have incredibly promising futures ahead of them. They have been an enormous help on these projects, and I have been whole-heartedly impressed with them every step of the way.

I also want to thank Matt Caporizzo, Amy Weil, Xiaonan Cui, Lisa Lippert, Deborah Shroder, Michael Woody, Martin Ng, Michael Hansen, Claire Fishman, Jeffrey Hallock, and Vishaka Karnawat, who have made the Goldman and Cooperman labs such a wonderful place to work.

Throughout this whole process, I've been kept grounded by my parents and my sister, who have been incredibly supportive. There is nothing as rejuvenating as

spending time with them at home playing with our dog Rascal in the living room or in our yard, and having a dinner together as a family.

Finally, my wife Lucie and our son Aiden have been the best things to ever happen to me. Lucie has been my best friend and companion for several years now, and we celebrated both our wedding and the birth of our son while in graduate school. Aiden's giggles and smiles always leave me beaming with happiness.

ABSTRACT

SINGLE-MOLECULE STUDIES OF tRNA DYNAMICS DURING ONGOING TRANSLATION

Ryan Jamiolkowski

Yale E. Goldman

The pre-translocation complex of the ribosome can undergo spontaneous fluctuations of mRNA and tRNAs between classical and hybrid states, and occupation of the hybrid tRNA positions has been proposed to precede translocation. The classic and hybrid state tRNA positions been extensively characterized when the ribosome is stalled along the messenger RNA by either the absence or the delayed addition of elongation factor G (EF-G), or by the presence of antibiotics or GTP analogs that block translocation. Surprisingly, during multiple ongoing elongation cycles when both EF-G and ternary complexes are present, we found that tRNA positions in PRE complex ribosome do not fluctuate. Instead, they adopt a stationary intermediate structure between the stalled classical and hybrid tRNA positions, as indicated by single molecule fluorescence resonance energy transfer (FRET) between adjacent tRNAs and between A-site tRNA and ribosomal protein L11. These results indicate that EF-G promotes the formation of an intermediate structure during ongoing translation.

smFRET experiments using labeled EF-G at those concentrations requires zero-mode waveguides (ZMWs), arrays of nanoscale holes in a thin metal film that confine the observation volume to reduce prohibitive background fluorescence. However, the need for specialized nanofabrication equipment has precluded their widespread adoption by the biochemical community. In contrast, nanosphere lithography uses the self-assembly of polystyrene beads into a hexagonal array, forming a natural lithographic mask for the deposition of metallic posts in the interstices between beads, followed by a different metal cladding around the posts and dissolution of the posts to leave a well array. The cross-sectional size of those interstices (and thus subsequent posts and wells) can be finely tuned by fusing the beads at the polystyrene glass transition temperature. That bead lattice serves as a

template for creating sub-wavelength ZMWs with little specialized equipment and at a low cost, enabling wide-scale adoption.

Table of Contents

List of Tables

List of Illustrations

1. Introduction

1.1 The central dogma of molecular biology and the genetic code

The "central dogma" of molecular biology is a term coined by Francis Crick in 1956, soon after his 1953 discovery (along with James Watson) of the double helix structure of deoxyribonucleic acid (DNA). The central dogma provides a framework to explain the directional conversion of the inheritable information stored in DNA into the polypeptide sequence of proteins. DNA forms double-stranded helices with specific pairing of its nitrogenous bases, allowing it to be robustly replicated from generation to generation of cells. Watson and Crick explained this process as follows (Crick and Watson, 1954):

> Now our model for deoxyribonucleic acid is, in effect, a pair of templates, each of which is complementary to the other. We imagine that prior to duplication the hydrogen bonds are broken, and the two chains unwind and separate. Each chain then acts as a template for the formation onto itself of a new companion chain, so that eventualy we shall have two pairs of chains, were we only had one before. Moreover, the sequence of the pairs of bases will have been duplicated exactly.

Within a cell, the linear genetic information in DNA contains the instructions for a specific protein encoded in the four-letter alphabet of deoxyribonucleotides: adenine (A), guanine (G), cytosine (C), and thymine (T). To be expressed as a functional protein, that genetic information must be converted to the 20-amino acid alphabet that determines a protein's primary structure. An intermediary in this process is messenger ribonucleic acid (mRNA), which is transcribed from the template strand of a DNA gene in a 5'→3' direction by an RNA polymerase. Although mRNA differs from DNA in having a backbone of ribonucleic acid (rather than deoxyribonucleic acid), as well as uracil (U) instead of thymine, the information in mRNA remains

similarly encoded: a four letter-alphabet copied from a template by nucleotide base-pairing. After transcription, the primary mRNA transcript undergoes several modifications to aid the subsequent translation to protein, such as 5' capping, poly (A) tail addition, and the splicing of eukaryotic mRNA.

The "genetic code" refers to the conversion between the 4-letter alphabet of nucleic acids and the 20-amino acid alphabet of proteins, via 3-nucleotide triplets (codons) that each encode for a single amino acid (Table 1.1). This three-to-one conversion was established in an experiment (Crick et al., 1961) that used proflavin-induced mutations of a T4-bacteriophage gene to demonstrate that mutants with insertion or deletion of one, two, or four nucleotides were unable to produce functional protein (due to a shift of reading frame), but could be rescued by using proflavin again to change the total number of nucleotides added or deleted to three. The formation of three-letter words with a four-letter alphabet creates $4^3 = 64$ possible codons, which significantly exceeds the 20 amino acids.

The first codon was then deciphered by synthesizing an artificial mRNA consisting of only uracil. The resulting peptide chain consisted only of phenylalanine (Phe), indicating that the mRNA UUU codon encodes Phe (Nirenberg and Matthaei, 1961). By the mid-1960s, all 64 codons were deciphered to reveal a mapping from codons to amino acids: in other words, all 20 amino acids are represented by at least one codon, with no ambiguity but significant redundancy. The redundancy in the genetic code is not random; in many cases, the codons that are synonyms for the same amino acid differ only in their third base (the "wobble" base). The process of translation is carried out by the ribosome, a sophisticated molecular machine consisting of catalytic RNA and protein.

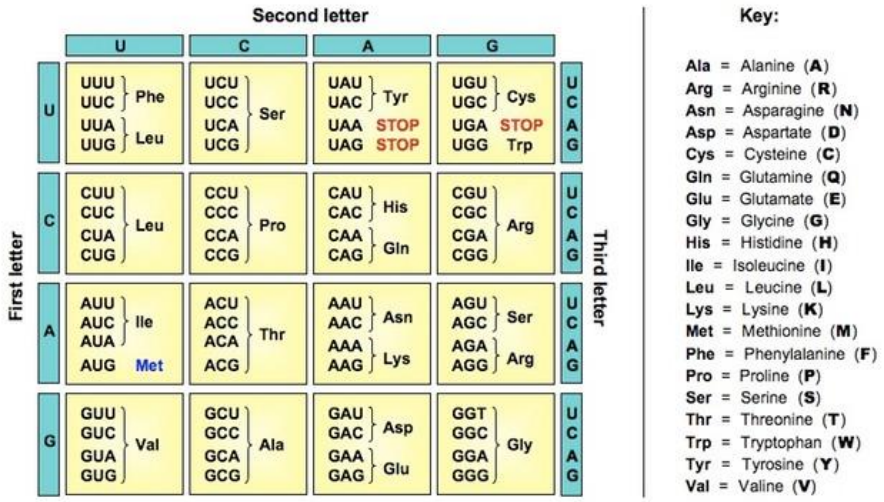

Table 1.1: The genetic code: translation of three nucleotide mRNA codons to the corresponding amino acids. (Reece and Campbell, 2011)

1.2 The ribosome

The ribosome is the ribonucleoprotein complex responsible for converting genetic information from an mRNA sequence into a chain of amino acids, which can then adopt the secondary and tertiary structures of a functional protein. They were first observed via electron microscopy by George Emil Palade as dense particles (Palade, 1955), earning him the 1974 Nobel Prize. The term "ribosome" was proposed by in 1958 as a portmanteau of the phrase "ribonucleoprotein particles of the microsome fraction."(Roberts, 1958)

Ribosomes can be classified as either "free" or "membrane-bound", which have identical structures but different spatial distributions. Membrane-bound ribosomes require an endoplasmic reticulum (ER)-targeting signal sequence on the protein being synthesized, which directs it to a pore complex through which the nascent polypeptide is fed while being translated. The portion of the ER with bound ribosomes is called the “rough” ER, due to its stippled appearance upon electron microscopy. The same

ribosome may be either membrane-bound or free when making different proteins.

The ribosome has large and small subunits comprised of both ribosomal RNA (rRNA) and proteins. Unlike mRNA, the rRNA does not contain instructions for the creation of proteins; instead, it acts as a "ribozyme". The catalysis of peptide bond formation in the prokaryotic ribosome is entirely carried out by catalytic rRNA, as there are no ribosomal protein subunits near the location of peptide bond formation.

Prokaryotic ribosomes are about 20 nm wide and consist of more rRNA than protein, while eukaryotic ribosomes are slightly larger (25-30 nm) and have approximately equal amounts of rRNA and protein. The large and small subunits assemble together on an mRNA when translation is initiated, and dissociate from each other when formation of the polypeptide is complete.

Due to the initial identification of the small and large subunits through sedimentation, they are also commonly known by their coefficient in Svedbeg units of sedimentation velocity (S). For a prokaryotic ribosome, a full 70S particle consists of a large 50S and small 30S subunit, while for a eukaryotic ribosome, the full 80S particle consists of a large 60S and small 40S subunit. The prokaryotic 30S subunit has a 16S rRNA subunit (1540 nucleotides) bound to 21 proteins, while the 50S subunit has a 5S rRNA (120 nucleotides), a 23S rRNA (2900 nucleotides) and 31 proteins.

During translation, the ribosome transits across each codon of the mRNA, pairing it with the appropriate amino acid provided by an aminoacyl-transfer RNA (tRNA), the physical link between the 4-nucleotide alphabet of the genetic code and the 20 amino acids used to construct proteins (Fig 1.2.1).

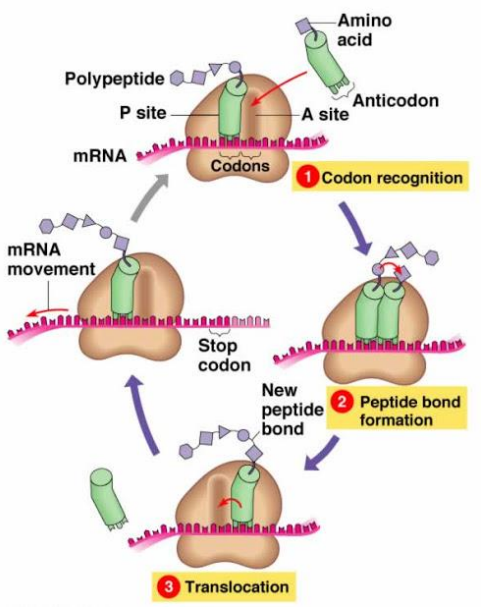

Figure 1.2.1: Simplified schematic of elongation cycle of ribosome during protein synthesis. (Reece and Campbell, 2011)

1.3 Transfer RNA (tRNA)

tRNA molecules are 76-90 nucleotides in length, and form a secondary cloverleaf-shaped structure with several distinct domains that fold into an L-shaped tertiary structure via coaxial stacking of RNA helices (Fig 1.3.1). The anti-codon loop forms three base pairs with the mRNA codon, thus coupling the genetic instructions to the correct amino acid attached to the tRNA's 3' CCA tail. The CCA tail is part of a 7-9 nucleotide acceptor stem that may contain non-Watson-Crick base-pairing (Jahn et al., 1991); the amino acid is covalently bonded to the 3'-hydroxyl group on the CCA tail by amino-acyl tRNA synthetases that recognize specific tRNAs (Ibba and Söll, 2000; Sprinzl and Cramer, 1979).

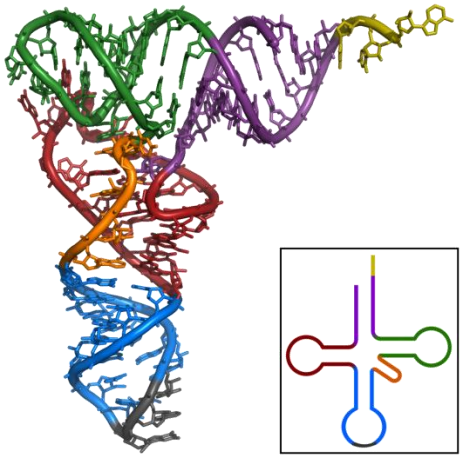

Figure 1.3.1: 3D structure and 2D schematic of tRNA, color-coded with CCA tail in yellow, acceptor stem in purple, variable loop in orange, D-arm in red, anticodon arm in blue, anticodon loop in gray, and T-arm in green. (Shi and Moore, 2000)

Many of the nucleotides in tRNA are chemically modified from the conventional RNA bases; the D-loop contains dihydrouracil (Itoh et al., 2013), while the T-loop contains the sequence TΨC, where Ψ is pseudouridine. Many other bases are methylated, and the wobble base of the anticodon loop is often modified to inosine (from adenine), pseudouridine or lysidine (from cytosine) (McCloskey and Nishimura, 1977). These modified bases can affect the tRNA's interaction with the ribosome, or the base-pairing at the codon-anti-codon recognition site. The tRNAs transit through the ribosome during translation, which consists of three major processes: initiation, elongation, and termination.

1.4 Ribosome structures

Although the ribosome was first observed using electron microscopy (Palade, 1955), structural details emerged with the advent of single particle reconstruction by

cryo-electron microscopy (cryo-EM) (Verschoor et al., 1986), a technique that later was optimized to achieve sub-nanometer resolution (Valle et al., 2003). Parallel to these cryoEM studies, efforts to crystalize the ribosome were a challenge due to the ribosome's size and asymmetry. However, ~3 Å structures of the separate 30S and 50S subunits were achieved first (Ban et al., 2000; Carter, 2001; Harms, 2001; Schluenzen et al., 2000; Wimberly, 2000), followed by a 5.5 Å structure of the 70S ribosome containing mRNA and all three tRNAs (Yusupov, 2001). These seminal ribosome crystal structures earned Ada Yonath, Venkatraman Ramakrishnan, and Thomas Steitz the 2009 Nobel Prize in Chemistry.

Ribosome crystal structures allowed several key insights into ribosome function. For example, the upper part of the 30S body and lower part of its head is the are the main parts of the decoding center, which consists of three long helices of 16S rRNA (h44, h16/17, h7) but *not* ribosomal proteins (Ban et al., 2000; Schluenzen et al., 2000; Wimberly, 2000). This supported the idea that the ribosome is a ribozyme, whose important catalytic functions are carried out by RNA rather than by protein. In addition, the 50S has several protein subunits (L7/L12 and L1) that extend off the ribosome as mobile appendages, and the tRNAs bind at the 30S:50S interface while interacting with both the 30S decoding center and the 50S peptidyl transferase center (Yusupov, 2001), and then transit successively through the A (aminoacyl), P (peptidyl) and E (exit) sites (Fig 1.4.1, 1.4.2).

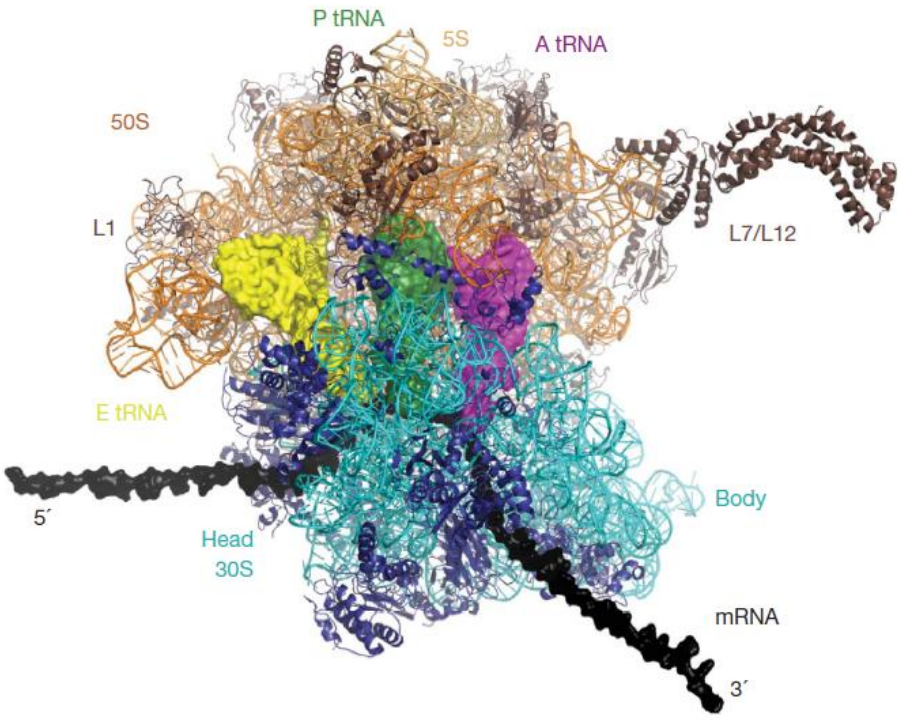

Figure 1.4.1: Crystal structure of 70S prokaryotic ribosome with three tRNAs in the A, P, and E sites (Schmeing and Ramakrishnan, 2009).

Higher resolution (~ 3 Å) crystal structures of the 70S ribosome (Schuwirth et al., 2005; Selmer et al., 2006) then revealed that the 30S subunit can undergo two main types of motions: its head can swivel, while its body can rotate ~ 6° relative to 50S subunit. Several other high resolution X-ray and cryo-EM structures revealed different steps of the elongation cycle, such as mRNA decoding (Demeshkina et al., 2012; Jenner et al., 2010), translocation (Agirrezabala et al., 2008; Connell et al., 2008; Julián et al., 2008; Ratje et al., 2010) and termination (Korostelev, 2008; Laurberg, 2008).

An important series of cryo-EM structures (Frank and Agrawal, 2000) suggested that EF-G binding and subsequent GTP hydrolysis can both lead to rotations of the small 30S subunit relative to the large 50S subunit. The authors proposed a two-step

mechanism of translocation: relative rotation of the subunits and opening of the mRNA channel following binding of EF-G; followed by advance of the mRNA and tRNAs in the direction of the rotation of the 30S subunit, following GTP hydrolysis. In addition to the subunit rotation, the L1 stalk was also observed by single molecule FRET to swing inwards into a closed conformation when the P-site is deacylated (Fei et al., 2008), while the tRNAs can tilt into a hybrid position in which the elbow and AA-acceptor sites of the tRNAs move relative to the ribosomal 50S subunit into the P and E sites to occupy A/P and P/E positions (1st letter is the 30S tRNA position, 2nd letter, the 50S position). It was proposed that tRNA tilting and subunit rotations were coupled together to define two main families of global states: classical unrotated states with untilted tRNAs, and hybrid rotated states with tilted tRNAs (Frank and Gonzalez, 2010). However, recent evidence demonstrates the tRNA tilting and subunit rotations are independent and temporally-distinct processes (Belardinelli et al., 2016; Sharma et al., 2016)

The stalled PRE complex has been observed to fluctuate between a classical state in which the tRNAs occupy corresponding sites in the large and small ribosomal subunits (A/A and P/P, 1st letter is the 30S tRNA position, 2nd letter, the 50S position), and a hybrid state in which the elbow and AA-acceptor sites of the tRNAs have moved relative to the ribosomal 50S subunit into the P and E sites to occupy A/P and P/E positions

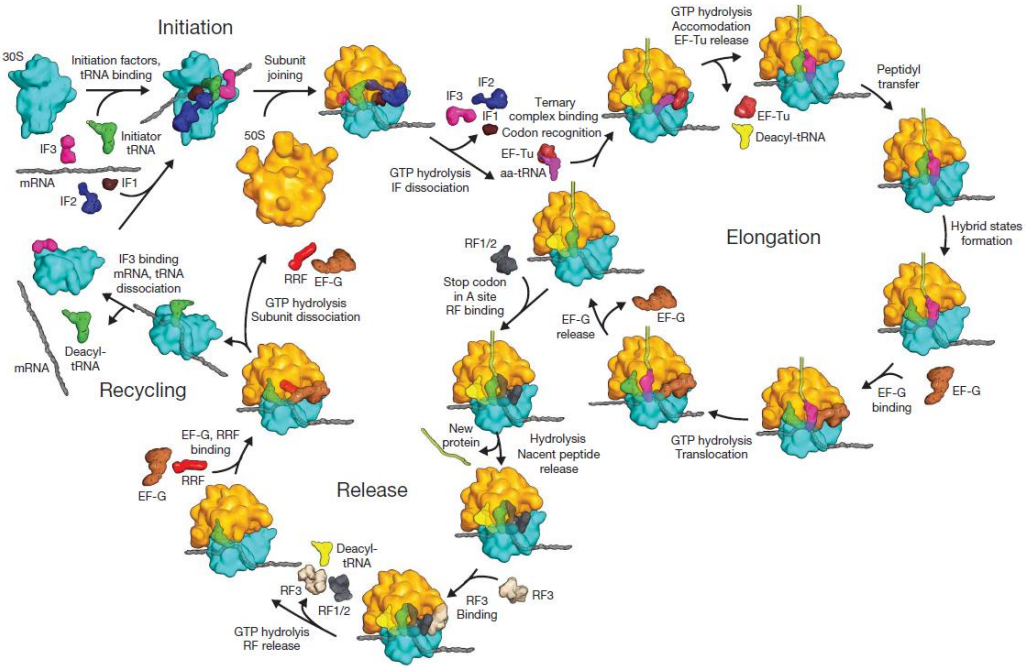

Figure 1.4.2: Detailed schematic of ribosome function during initiation of protein synthesis, elongation, and termination/release (Schmeing and Ramakrishnan, 2009)

1.5 Initiation of protein synthesis in the prokaryotic ribosome

Binding of the mRNA by the ribosome large and small subunits also requires the initiator tRNA fMet-tRNA^{fMet} (which is complementary to the start codon), as well as initiation factors 1-3 (IF1-3). During initiation, the 30S subunit is bound by IF3 and IF1 (which prevents premature binding of the 30S and 50S subunits) and the Shine-Dalgarno sequence of the mRNA (a ribosomal binding site on the mRNA located about 8 bases upstream of the start codon, which helps align the ribosome with the start codon), followed by a complex of IF2 and fMet-tRNA^{fMet}. The dissociation of IF1 and IF3 allows that 30S initiation complex to dock with the 50S subunit, and IF2 hydrolysis of GTP and subsequent dissociation translocates the initator tRNA to the P-site, creating an active initiation complex with a vacant A-site codon.

1.6 Peptide elongation in the prokaryotic ribosome

The elongation cycle has three main steps: decoding, peptide bond formation and translocation. Each cycle begins after a previous cycle has ended, thus the initial state of the cycle is conventionally considered to be the post-translocation (POST) complex with a peptidyl-tRNA in the P-site and an empty A-site.

1.6.1 The pre-translocation (PRE) complex: decoding and peptide bond formation

Elongation factor thermally unstable (EF-Tu) is a GTPase that forms a ternary complex with aminoacyl tRNA and GTP; that ternary complex (TC) delivers the cognate aminoacyl tRNA to the mRNA codon in the A-site of the ribosome (Pape et al., 1998), which forms the pre-translocation (PRE) complex.

The ternary complex is guided to the A-site by the ribosomal L7/L12 stalk, followed by adoption of an A/T state in which the tRNA structure is distorted: the anticodon stem of the tRNA enters the decoding center of the 30S subunit and the acceptor arm and EF-Tu interact with the 50S GTPase activation center, but the tRNA is not yet accommodated into the A-site. This reversible, incomplete accommodation enhances the accuracy of translation; it allows an opportunity for non-cognate tRNA to dissociate from the ribosome before being released by EF-Tu. Once EF-Tu hydrolyzes GTP (allosterically triggered by a cognate codon-anticodon interaction at the decoding center), releases Pi, and dissociates, the tRNA completes its

accommodation into an A/A state. (Voorhees et al., 2009) Peptide bond formation then immediately occurs, with the polypeptide chain transferring from the P-site tRNA to the A-site tRNA and leaving deacylated-tRNA in the P site.

Although some ribosomes in the PRE complex can undergo spontaneous translocation at a very slow rate without catalysis by elongation factor G (Cukras et al., 2003; Fredrick and Noller, 2003; Gavrilova and Spirin, 1971; Gavrilova et al., 1976; Pestka, 1969), most will remain stalled in the PRE complex on the measurement timescale of seconds to minutes (Blanchard et al., 2004). The stalled PRE complex has been observed to fluctuate between a classical state in which the tRNAs occupy corresponding sites in the large and small ribosomal subunits (A/A and P/P, 1st letter is the 30S tRNA position, 2nd letter, the 50S position), and a hybrid state in which the elbow and AA-acceptor sites of the tRNAs have moved relative to the ribosomal 50S subunit into the P and E sites to occupy A/P and P/E positions (Agirrezabala et al., 2008; Blanchard et al., 2004; Chen et al., 2011; Julián et al., 2008; Kim et al., 2007; Moazed and Noller, 1989; Wang et al., 2011) In the classical to hybrid transition, there is also a 6° rotation of the ribosomal subunits relative to each other (Agirrezabala et al., 2008; Frank and Agrawal, 2000) and movement of the L1 stalk towards the deacylated P-site tRNA (Cornish et al., 2009a, 2009b, Fei et al., 2008, 2009, 2011).

The adoption of the hybrid configuration may not occur simultaneously for both tRNAs; intermediate states have been found using stopped flow spectrofluorometry (Pan et al., 2007), single molecule fluorescence resonance energy transfer (smFRET) (Munro et al., 2007a) and cryo-electron microscopy (cryo-EM, Fig 1.6.1) (Fischer et al., 2010), in which the deacylated tRNA adopts the hybrid P/E conformation without the peptidyl tRNA shifting into the A/P state.

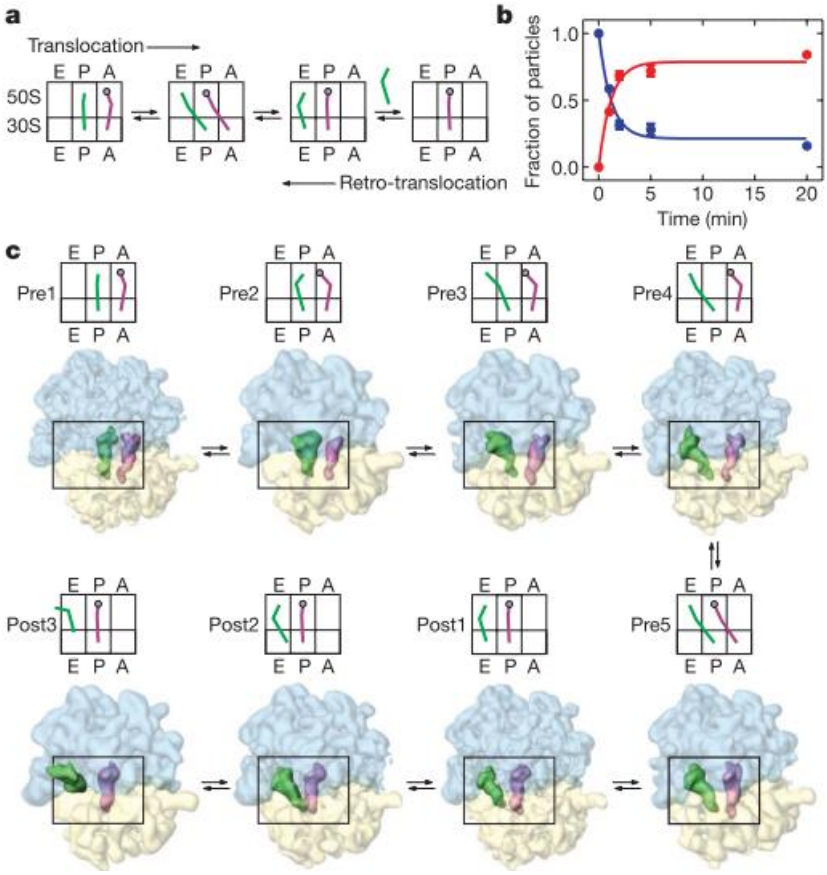

Figure 1.6.1: (A) Schematic of the forward and reverse translocation of tRNAs within the ribosome. (B) Time course of retro-translocation determined from cryo-EM image series with the red symbols indicating the fraction of particles in a PRE state, and the blue symbols indicating the fraction of particles in a POST state. (C) CryoEM states obtained from ribosomes allowed to undergo slow reverse translocation in the absence of EF-G. Several different pre-translocation (PRE) and post-translocation (POST) states were identified. Amongst the PRE states, two had "classical" tRNA positons (A/A and P/P; Pre1 and Pre2), while one had fully "hybrid" tRNA positons (A/P and P/E; Pre5). Pre3 and Pre4 occupied intermediate states in which the A-site tRNA remained A/A, while the P-site tRNA was P/E. (Fischer et al., 2010)

1.6.2 Elongation factor G and translocation

Elongation factor G (EF-G, historically known as translocase) is a GTPase that catalyzes the coordinated movement of tRNA and mRNA through the ribosome. Like

EF-Tu, EF-G is channeled toward the A-site by the L7/L12 stalk on the ribosome (Gao et al., 2009). After EF-G·GTP binds, it rapidly hydrolyzes GTP and releases Pi, releasing energy that promotes the translocation of the tRNAs and mRNA through the ribosome by one codon. In other words, the tRNAs (as well as the mRNA with which it formed codon-anticodon base pairs) move from the the A and P- sites to the P and E-sites via at least two intermediates (Pan et al., 2007).

The manner in which EF-G interacts with a PRE state that can occupy classical or hybrid positions has been a subject of intense study; the hybrid state PRE state is believed to play an important role in EF-G induced translocation. Ribosome toeprinting showed that when EF-G·GTP is added to stalled PRE complexes, the resulting translocation requires the CCA tail of the A-site tRNA to interact with a segment of 23S rRNA in the P site, termed the P-loop, implying occupancy of the A/P state (Dorner et al., 2006). The antibiotic viomycin traps the stalled ribosome in a hybrid state, according to rotation sensitive fluorescence resonance energy transfer (FRET) pairs, suggesting that EF-G promotes the hybrid state (Ermolenko et al., 2007). However, other smFRET evidence showed that EF-G·GTP can bind to either classical or hybrid stalled PRE complexes, resulting in a halt of fluctuations between classical and hybrid states prior to translocation. Hybrid ribosomes can complete translocation directly, whereas EF-G bound ribosomes in the classical state pass through the hybrid state very briefly prior to translocation (Chen et al., 2011, 2013).

Most earlier studies focused on the classical-hybrid equilibrium have used ribosomes stalled or slowed in the absence of EF-G·GTP (Fischer et al., 2010; Kim et al., 2007; Munro et al., 2007a; Ning et al., 2014; Wang et al., 2011), by the use of EF-G·GDPNP (Cornish et al., 2009b; Fei et al., 2008, 2009, 2011), antibiotics (Adio et al., 2015; Lin et al., 2015; Zhou et al., 2014), or by introducing EF-G·GTP to stalled

ribosomes that had already reached a classical-hybrid equilibrium (Adio et al., 2015; Chen et al., 2011). Less is known about the ribosomal PRE complex undergoing translation when EF-G·GTP and ternary complexes are present together in solution and bind in quick succession during multiple elongation cycles.

1.6.3 Termination of protein synthesis

The elongation cycle continues until a stop codon (UAA, UAG or UGA) enters the ribosome's the A-site, which is recognized by release factors RF1 or RF2. Those release factors have a conserved GGQ motif that is positioned in the peptide transfer center, triggering hydrolysis of the polypeptide chain from the amino-acyl P-site tRNA, and release of that polypeptide from the ribosome (Laurberg, 2008; Weixlbaumer, 2008). The ribosome is then recycled for reuse by the actions of RF3 (which hydrolyzes GTP to accelerate the loss of RF1 and RF2 from the ribosome) (Zavialov et al., 2002), by ribosome release factor (RRF), and by EF-G (Hirashima and Kaji, 1973).

1.7 Pharmacological significance of the ribosome

1.7.1 Anti-ribosomal antibiotics

Due to differences in the structures of the prokaryotic and eukaryotic ribosomes and the necessity of protein synthesis for bacterial survival, the prokaryotic ribosome is a major source of targets for antibiotics that target different stages in the translational cycle. For example, linezolid prevents the formation of the initiation complex by blocking 50S subunit association (Swaney et al., 1998), while tetracyclines/doxycycline and tigecycline obstruct the A-site in the 30S subunit, preventing an amino-acyl-tRNA from accommodating (Townsend et al., 2007).

Aminoglycosides and spectinomycin impair proof-reading in the 30S subunit to cause errors in protein synthesis, as well as inducing early termination of a polypeptide chain and impeding translocation (Borovinskaya, 2007; Mingeot-Leclercq et al., 1999). Chloramphenicol prevents peptidyl transfer in the 50S subunit, as do macrolides such as erythromycin (which also prevent translocation) (Mazzei et al., 1993). Streptogramins also inhibit peptidyl transfer at the 50S subunit and promote premature peptide release (Allington and Rivey, 2016), and clindamycin blocks translocation at the 50S subunit (Schlunzen et al., 2001).

1.7.2 Viral programmed ribosomal frameshifting (PRF)

Since mRNA is interpreted in 3-nucleotide codons, each mRNA could code for three different amino acid sequences depending on its reading frame. The reading frame of the start codon is designated the 0-frame, while reading frames shifted by one nucleotide in the upstream (5') or downstream (3') directions are termed the -1 and +1 frames, respectively. The mRNAs of some viruses include sequence and structural elements that induce the ribosome to shift into the +1 or -1 frame. These are the most common frame shifts found in common pathogenic viruses, but others may also occur. Programmed ribosomal frameshifting (PRF) allows viruses to compress more information into their genomes, whose size is restricted by the small volumes of viral capsids (Plant and Dinman, 2006). PRF is also used to regulate the stoichiometry of viral protein production; since small changes in PRF efficiency can alter these ratios and disrupt viral assembly, PRF is a promising target for antiviral drugs.

Viral PRF into the -1 frame is central to the reproductive cycle of IBV, HIV, SARS, and West Nile. A -1 PRF site consists of two components: a 7-nucleotide

slippery sequence where the frameshifting occurs, and a stimulatory downstream mRNA secondary (2°) structure. The slippery sequence alone is capable of inducing PRF, but at very low efficiencies (0-4%). It is only when an mRNA 2° structure is present that efficiency is increased to 10-60% (Brierley, 1995; Farabaugh, 1996). The stimulatory mRNA 2° structure is often a pseudoknot (containing at least two stem-loop structures in which half of one stem is intercalated between the two halves of another stem) located 6–9 nucleotides downstream of the slippery sequence.

1.7.3 Nonsense suppression for genetic diseases caused by premature termination codons

Premature termination codons, also known as nonsense mutations, refer to the replacement of an amino acid codon in mRNA by one of the three universal stop codons (UAA, UGA or UAG)(Keeling et al., 2014; Shalev and Baasov, 2014). Nonsense mutations are responsible for a high percentage of germline and somatic genetic defects that cause cancer (Bordeira-Carriço et al., 2012; Loudon, 2013) particularly metastatic disease (Miyaki et al., 2002; Peltz et al., 2013). In addition, approximately 11% of genetically transmitted disorders in humans are caused by nonsense mutations (Loudon, 2013). Treatment of premature termination codon disorders have been attempted using nonsense suppressors, which stimulate the selective insertion of near cognate tRNAs at the premature stop position, thus restoring the production of full length functional proteins. Since many of the defective proteins (such as dystrophin in Duchenne's muscular dystrophy and CFTR in cystic fibrosis) only require a small level of expression to restore function, even low read-through rates of the premature termination codons may lead to dramatic clinical improvements.

While aminoglycoside antibiotics block translation altogether on the prokaryotic ribosome, some (such as gentamicin and paromomycin) instead induce read-through of premature termination codons by eukaryotic ribosomes. However, many aminoglycosides have significant oto- and nephrotoxicities, caused in part by their inhibition of mitochondrial ribosomes that resemble those of bacteria(Oishi et al., 2015). Clinical trials using gentamicin to treat Duchenne muscular dystrophy or cystic fibrosis were terminated early due to such adverse events.

The most prominent non-aminoglycoside therapeutic for inducing premature stop codon read through is ataluren (previously known as PTC124), which was identified from a high-throughput screen and had very low toxicity. After initially promising results in small scale clinical studies, its efficacy proved to be poor; the FDA declined to consider it for review due to insufficient evidence of benefit, while the EU initially granted approval in 2014, but is considering withdrawing it. Other agents are in preclinical development, but development has been hindered by a lack of knowledge of their mechanism of action (Du et al., 2009, 2013; Gonzalez-Hilarion et al., 2012; Loudon, 2013).

1.8 The Brownian ratchet and power stroke models of translocation

In one of the predominant models in the field. Joachim Frank et al. (Frank and Agrawal, 2000; Frank and Gonzalez, 2010) postulated that the conformational motions of subunit rotation, L1 stalk movement, and tRNA tilting between classical and hybrid positions allows the ribosome to behave as a thermal or Brownian ratchet, rectifying random fluctuations into directional movement.

The original “thermal/Brownian ratchet” model was a 1912 thought experiment by physicist Marian Smoluchowski, later popularized by Richard Feynman in his

"Lectures on Physics" at the California Institute of Technology. Rather than representing an actual physical process, it was meant to illustrate nuances of the second law of thermodynamics ("the total entropy of an isolated system always increases over time") via a paradox; Feynman explained that such a machine cannot exist as originally formulated.

An idealized Brownian ratchet would consist of a rotating gear (the ratchet) that can spin freely in only one direction, since its ability to rotate the opposite direction is obstructed by a pawl. The spinning gear is immersed in a fluid with temperature T_2 connected by axle to a paddle wheel in a fluid fixed at temperature T_1 (a constant heat bath without a heat gradient), while the whole device is small enough that the impulse from single molecular collisions can turn the paddle. Although the paddle can be hit from all directions (which could turn the axle in either direction), the pawl only allows it to turn one way, which would allow it to perform useful work (Fig 1.8.1).

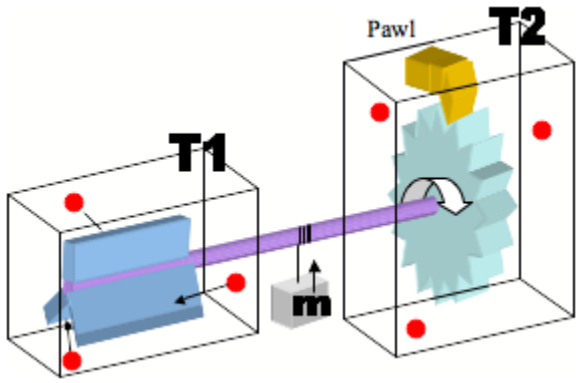

Figure 1.8.1: Schematic of a theoretical Brownian ratchet, with a paddle immersed in fluid of temperature T_1, connected by an axle to a ratchet with a pawl immersed in a fluid of temperature T_2
(https://en.wikipedia.org/wiki/Brownian_ratchet)

If $T_2 = T_1$ (the original formulation of the model), this would violate the second

law of thermodynamics when expressed as the Kelvin-Planck statement, namely that "it is impossible for any device that operates on a cycle to receive heat from a single reservoir and produce a net amount of work." (Halder, 2014) In a heat engine, heat transferred from a high temperature reservoir (Q_H) is split between a component used to perform useful work (W_{net}), and a component that is rejected to a low temperature reservoir (Q_L) to complete the cycle. Conservation of energy thus requires $W_{net} = Q_H - Q_L$, implying that work requires temperature difference between the two reservoirs. As a perpetual motion machine, this thermal ratchet cannot exist. Thus what of this mechanism is overlooked in this thought experiment?

Feynman resolved this apparent paradox by explaining that if the pawl is the same temperature as the paddle, it will also undergo random thermal motions, bouncing up and down to allow the gear to slip backwards, resulting in no net direction of rotation. Thus, a truly functional Brownian ratchet would require a temperature difference between the solution bathing the paddle and the pawl ($T_1 \neq T_2$) in order to be productive.

Thus, a functional Brownian ratchet does require a thermal gradient (in heat engine terms). In biological terms, that means translocation would require an expenditure of energy. For the ribosome undergoing translation in a directional motion along the mRNA, the GTP hydrolysis carried out by EF-G is likely that source of energy. However, despite being the predominant model in the field, the Brownian ratchet is not the only explanation for EF-G's role in converting the energy released by GTP hydrolysis into mechanical motion during translocation. An alternative model is a power stroke, similar to a motor protein like myosin, dynein, or kinesin.

In a power stroke, EF-G hydrolysis of GTP generates force that "pushes" the

tRNAs and mRNA to their next position (tilting the energy landscape to lower both the transition barrier and the energy of the final state). In contrast, a Brownian ratchet would "wait" for spontaneous thermal oscillations to cause that movement over an unchanged energy landscape, and only *after* that spontaneous motion would it raise the transition barrier to reverse translocation via a pawl's locking motion (Fig 1.8.2).

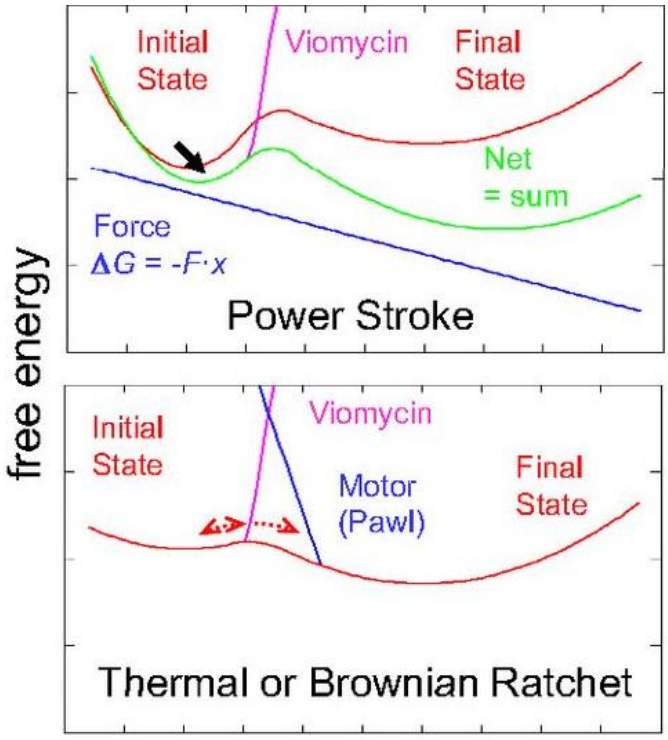

Figure 1.8.2: Reaction coordinates for the power stroke and thermal ratchet models of EF-G catalyzed translocation. (Chen et al., 2016)

Research from our group has studied the rotational motions of a bifunctional fluorescent probe attached to different domains of EF-G, which can be recorded at the single molecule level during translation using polarized total internal reflection fluorescence (polTIRF) microscopy (Chen et al., 2016). That study found that EF-G undergoes a 10° rotation relative to the ribosome after GTP hydrolysis, followed by a larger rotation within domain III of EF-G before it dissociates from the ribosome.

Upon addition of the antibiotic viomycin (which fixes tRNAs in the hybrid conformational state) spontaneous tRNA translocation was blocked but EF-G still had detectable (but diminished) rotational motions, showing that EF-G does not "wait" for spontaneous thermal movement of the tRNAs before acting as a pawl, and instead initiates movement as in a power stroke.

After the initial power stroke, EF-G still undergoes further conformational changes as translocation is completed. Its domain IV may accompany the A-site tRNA into the P site in the 30S subunit or follow it after spontaneous tRNA arrival, but it does not undergo large rotations coupled with domain III. Those later motions of EF-G could proceed via either a power-stroke or Brownian-ratchet mechanism. In those later stages of translocation, the force dependence of translational velocity in an optical trap (Liu et al., 2014) suggest a Brownian ratchet mechanism, which is consistent with the hypothesis that the later steps are driven by the energetics of the ribosome itself (Frank and Gonzalez, 2010). A recent model consistent with this data suggests a combined power-stroke and Brownian ratchet mechanism (Holtkamp et al., 2014).

1.9 Implications of a power stroke model of translocation

The iconoclastic finding of an initial EF-G power stroke by polTIRF (Chen et al., 2016) suggested that EF-G stroke did not wait for the tRNAs to spontaneously move on their own, but rather initiated the motion in translocation. However, those experiments observed only the conformational changes of EF-G, without being able to note the tRNA positions during this process.

Most earlier crystal structures or cryo-EM of EF-G bound ribosomes captured a state after translocation is already complete, with EF-G unable to dissociate because it is locked in place by antibiotics like fusidic acid (Gao et al., 2009; Tourigny et al., 2013; Valle et al., 2003). However, more recent EF-G-bound ribosome structures do show early steps in translocation. One demonstrated the A-site tRNA being "handed" to the P-site (Fig 1.9.1), (Zhou et al., 2014). Rather than tilting into the A/P conformation (translocating in the large subunit before the small subunit), the A-site tRNA incompletely shifted in both subunits to adopt a state termed ap/ap.

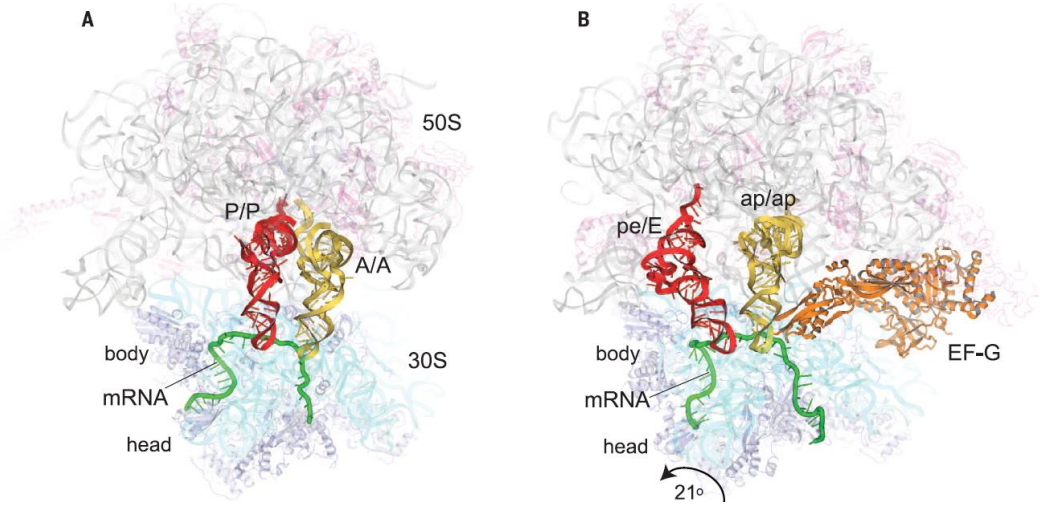

Figure 1.9.1: Comparison of crystal structures of (a) classical PRE state with tRNAs bound in A/A, P/P positions, with (b) an EF-G bound state and tRNAs in ap/ap and pe/E positons (Zhou et al., 2014).

Another recent crystal structure of the EF-G-bound PRE complex suggests the existence of two "superdomains" in EF-G (I-II and III-IV-V) that swivel together to form a compact structure while bound to the PRE complex, and extend into an elongated conformation during translocation (Lin et al., 2015). These snapshots of a dynamic cycle do not reinforce either the power stroke or Brownian ratchet model;

real-time recording of translation at the single molecule level is necessary to understand that process.

tRNAs have long been observed to spontaneously fluctuate between classical A/A, P/P and hybrid A/P, P/E positions when EF-G is absent (Blanchard et al., 2004; Chen et al., 2011). Thus, if they are not testing positions to be rectified by a ratchet pawl, what (if any) role do these fluctuations have during ongoing translation? How would a power stroke affect their positions during the initial steps of translocation? That question is the major focus of the work detailed in this thesis.

1.10 Single molecule FRET and zero mode wavguides (ZMWs)

Single molecule fluorescence techniques are valuable tools in biophysics; by avoiding the averaging inherent in bulk measurements, they can distinguish subpopulations of molecules, directly observe the trajectory and timing of reaction steps without needing to synchronize the whole population, and can study rare events and conformational fluctuations. These techniques include super-resolution microscopy to track single molecule motion, fluorescence resonance energy transfer (FRET) probes to detect nanometer-scale distance changes, and polarized total internal reflectance (polTIRF) microscopy that measures angular changes of a macromolecule. The primary technique used in this work is single molecule Förster (or fluorescence) resonance energy transfer (FRET). During a FRET measurement, an excited donor fluorophore transfers some of its energy to an acceptor fluorophore; the ratio of donor and acceptor emission is sensitive to nanometer-distances and provides a real-time measure of conformation changes (Fig 1.10.1).

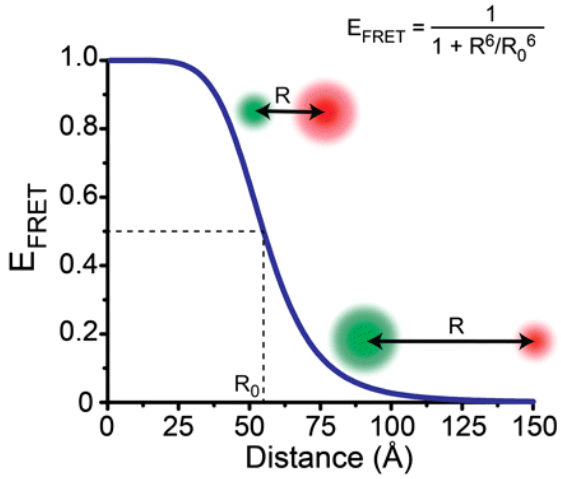

Figure 1.10.1: Schematic showing the sharp distance dependence of FRET efficiency at lengths near the R_0 of the selected FRET pair. The green ball represents the donor fluorophore (such as Cy3), while the red ball represents the acceptor fluorophore (such as Cy5), with their relative sizes indicating the partition of energy between them for fluorescence imagine. FRET can thus be used as a sensitive molecular ruler for lengths within a of roughly 50 Angstroms centered at the R_0 for that FRET pair (Tinoco and Gonzalez, 2011).

Many single molecule fluorescence techniques (including smFRET) utilize total internal fluorescence fluorescence (TIRF) microscopy, in which incident light reaches the glass-water interface at an angle relative to the normal incidence that is greater than the critical angle, and is totally internally reflected. However, a near-field standing wave (the evanescent wave) is created at the interface that decays exponentially with distance from the boundary. This excites only the fluorescent molecules very close (<100 nm) to the glass-water interface, significantly reducing background fluorescence.

Despite the advantages offered by TIRF, background fluorescence from labeled substrates in solution remains a technical challenge in single molecule studies, forcing the substrates to be used at nano-/pico-molar concentrations. Most smFRET experiments (including most in this thesis) are thus conducted at those concentrations of labeled substrate. However, biological processes usually occur at concentrations up to a million-fold greater (micro-/milli-molar), a challenge that can be addressed through the use of zero mode wave guides (ZMWs), nanoscale devices that can allow the use of much higher concentrations of labeled molecules (Uemura et al., 2010).

When studying molecular dynamics, a small observation volume allows higher concentrations of fluorescently-labelled molecules to be used. One method to reduce observation volume is to block detection of emission from part of the illuminated sample, such as the pinhole of a confocal microscopy that blocks light coming from the out-of-focus volume. Similarly, stimulated emission depletion (STED) microscopy uses a second laser source at the fluorescence emission wavelength to darken pat of the illuminated area, allowing the imaging of a subdiffraction-limited spot (Hell and Wichmann, 1994). An example of a far-field excitation technique to limit excitation volume is two-photon microscopy, which relies on the quadratic-decreasing probability of fluorescent molecules being excited by two photons outside of the most intense focal spot (Denk et al., 1990). Another approach is to limit the excitation volume by using near-field techniques, such as near field scanning optical microscopy (NSOM). NSOM scans a sample with an optical fiber probe that is placed close enough to the molecule to be imaged that it is only excited by an evanescent wave coming off the probe's tip (ie, within a wavelength λ of the surface) (Betzig and Chichester, 1993; Xie and Dunn, 1994). Zero mode waveguides use a similar near field effect, but rely on the samples residing inside an array of wells that

can be simultaneously imaged, rather than bringing a probe very close to a single sample at a time.

ZMWs are arrays of holes (30-300 nm diameter) in a thin, opaque metal layer (typically aluminum, chromium, or gold) on a glass substrate.(Moran-Mirabal and Craighead, 2008) These sub-wavelength apertures do not propagate optical modes in the visual spectrum, but illumination will create an evanescent wave (like in TIRF) that decays inside the well (Bethe, 1944; Genet and Ebbesen, 2007) (Fig 1.10.1. 1.10.3). Intuitively, the waveguides act similar to the mesh grating on the transparent door of the microwave; because the openings in conductive mesh are smaller than the wavelength of the contained electromagnetic waves, they are unable to pass through to the outside world to be a risk to the health of nearby people. A more rigorous explanation of this physical phenomenon is detailed in the subsequent section.

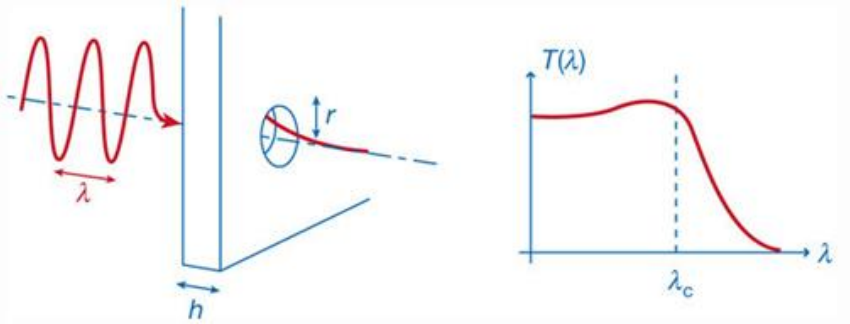

Figure 1.10.2: A cylindrical waveguide with metal film thickness h and a radius r much smaller than the wavelength λ of the incident electromagnetic field results in an exponentially decreasing transmitted intensity as a function of wavelength after the cutoff wavelength λ_c. (Genet and Ebbesen, 2007)

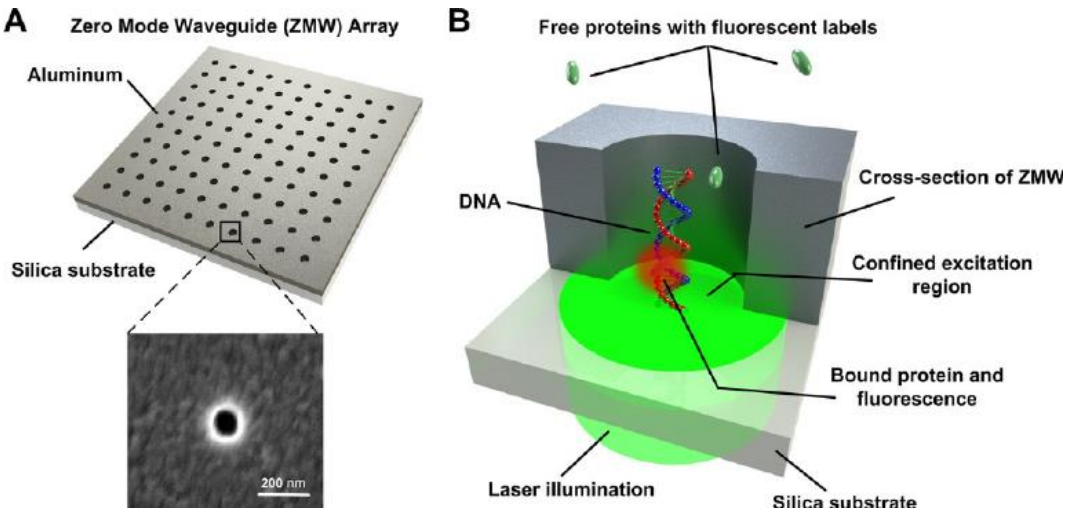

Figure 1.10.3: (A) Zero mode waveguide array consisting of 200 nm diameter holes in an aluminum cladding on a silica substrate, with (B) a schematic of its use for single molecule fluorescence studies of DNA-binding proteins. (Zhao et al., 2014)

1.11 Wave guide theory

1.11.1 Electromagnetic field in a waveguide

If electromagnetic waves are confined in the interior of a hollow pipe made of a conducting material, that pipe will serve as a wave guide that selects particular modes for transmission. In the following derivation adapted from Griffiths (Griffiths, 2012), we can demonstrate the theory underlying this effect in the case of a waveguide made of a perfectly conducting material. The z-axis here is established as the longitudinal axis of the hollow pipe.

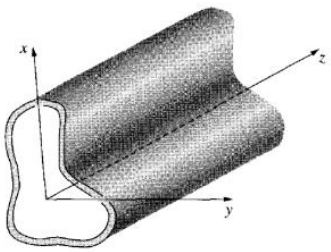

Figure 1.11.1: Schematic of generic hollow pipe waveguide, for waves propagating in the z-direction. (Griffiths, 2012)

As a perfect conductor, all electrons are free to move within the material until every charge experiences a net zero force. Thus, the electric and magnetic fields inside the material must be zero, giving the boundary conditions at the inner wall:

$$\left.\begin{aligned} \boldsymbol{E}^{\parallel} &= 0 \\ \boldsymbol{B}^{\perp} &= 0 \end{aligned}\right\} \qquad \text{(Eq. 1.1)}$$

A waveguide's effects are most evident on waves the propagate down the axis of the tube, this the generic form for the electric and magnetic fields are as follows (where k is the wave number, and ω is the frequency):

$$\left.\begin{aligned} \boldsymbol{E}(x,y,z,t) &= \boldsymbol{E_0}(x,y)e^{i(kz-\omega t)} \\ \boldsymbol{B}(x,y,z,t) &= \boldsymbol{B_0}(x,y)e^{i(kz-\omega t)} \end{aligned}\right\} \qquad \text{(Eq. 1.2)}$$

These electric and magnetic fields must satisfy Maxwell's Equations. In differential form, those equations are:

$$\left.\begin{aligned} \nabla \cdot \boldsymbol{E} &= 0 \\ \nabla \cdot \boldsymbol{B} &= 0 \\ \nabla \times \boldsymbol{E} &= -\frac{\partial B}{\partial t} \\ \nabla \times \boldsymbol{B} &= \frac{1}{c^2}\frac{\partial E}{\partial t} \end{aligned}\right\} \qquad \text{(Eq. 1.3)}$$

Where c represents the speed of light in a vacuum. The task then reduces to a boundary value problem, which seeks to find $\boldsymbol{E_0}$ and $\boldsymbol{B_0}$ such that the fields $\boldsymbol{E}(x,y,t)$

and $\boldsymbol{B}(x, y, t)$ obey Maxwell's differential equations subject to the boundary conditions given above. The details of this derivation are expanded in Griffiths (Griffiths, 2012). In summary, we may express the x and y components of $\boldsymbol{E_0}$ and $\boldsymbol{B_0}$ as functions of E_z, B_z. That solution gives the uncoupled equation:

$$\left.\begin{aligned}\left[\frac{\partial^2}{\partial x^2}+\frac{\partial^2}{\partial y^2}+\left(\frac{\omega}{c}\right)^2-k^2\right]E_z=0\\ \left[\frac{\partial^2}{\partial x^2}+\frac{\partial^2}{\partial y^2}+\left(\frac{\omega}{c}\right)^2-k^2\right]B_z=0\end{aligned}\right\} \qquad \text{(Eq 1.4)}$$

This can then be plugged into the equations for x and y components of $\boldsymbol{E_0}$ and $\boldsymbol{B_0}$ as functions of E_z, B_z that can be found in Appendix A. Note that if $E_z = 0$, the electric field has no component along the waveguide's axis, and is thus called a transverse electric (TE) wave. Similar, if $B_z = 0$, the magnetic field has no component along the waveguide's axis, and is called a transverse magnetic (TM) wave. $E_z = 0$ and $B_z = 0$, the wave is a called a TEM wave, but that cannot occur in a hollow wave guide.

1.11.2 TE fields in a rectangular waveguide

Although the geometry of most zero mode waveguides used for single molecule FRET are circular in cross section, the theory behind electromagnetic attenuation past a cut-off wavelength is most intuitively clear in the derivation for a rectangular waveguide, detailed below, in a derivation is also adapted from Griffiths (Griffiths, 2012).

We can define a hollow rectangular waveguide made of a perfect conductor, with height a and width b.

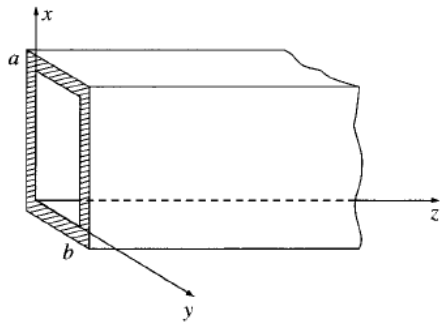

Figure 1.11.2: Schematic of rectangular waveguide, for waves propagating in z-direction. (Griffiths, 2012)

A transverse electric (TE) wave has $E_z = 0$ and $B_z \neq 0$, so all E components are transverse to the direction of propagation. Since $E_z = 0$, once we find B_z we can plug it into the equations for E_x, E_y, B_x, B_y to get all of those components. To calculate the behavior of TE waves in that guide, we must solve:

$$\left[\frac{\partial^2}{\partial x^2} + \frac{\partial^2}{\partial y^2} + \left(\frac{\omega}{c}\right)^2 - k^2\right] B_z = 0 \qquad \text{(Eq. 1.5)}$$

sgain subject to the boundary conditions:

$$\left.\begin{matrix} \boldsymbol{E}^{\parallel} = 0 \\ \boldsymbol{B}^{\perp} = 0 \end{matrix}\right\} \qquad \text{(Eq. 1.6)}$$

This task derivation can be approached with separation of variables, which is detailed in Appendix A. We thus define:

$$B_z(x, y) = X(x)Y(y) \qquad \text{(Eq. 1.7)}$$

Thus,

$$Y\frac{d^2X}{dx^2} + X\frac{d^2Y}{dy^2} + \left[\left(\frac{\omega}{c}\right)^2 - k^2\right] XY = 0 \qquad \text{(Eq. 1.8)}$$

We can now divide by XY and note that the x- and y-dependent terms must be

constant:

$$\left.\begin{aligned}\frac{1}{X}\frac{d^2X}{dx^2} &= -k_x^2\\ \frac{1}{Y}\frac{d^2Y}{dy^2} &= -k_y^2\end{aligned}\right\} \qquad \text{(Eq. 1.9)}$$

Those constants are thus related as follows:

$$-k_x^2 - k_y^2 + \left(\frac{\omega}{c}\right)^2 - k^2 = 0 \qquad \text{(Eq. 1.10)}$$

The system of differential equations that we found above has the general solution:

$$\left.\begin{aligned}X(x) &= Asin(k_x x) + Bcos(k_x x)\\ Y(x) &= Csin\left(k_y y\right) + Dcos\left(k_y y\right)\end{aligned}\right\} \text{ (Eq. 1.11)}$$

We now simply need to apply our boundary conditions to find the constants in those equations. $\boldsymbol{B}^{\perp} = 0$ implies that $B_x = 0$ at $x = 0$ and $x = a$. S since $B_x = \frac{i}{\left(\frac{\omega}{c}\right)^2 - k^2}\left(k\frac{\partial B_z}{\partial x} - \omega\frac{\partial E_z}{\partial y}\right)$, that means that $\frac{\partial B_z}{\partial x} = \frac{dX}{dx} = 0$ at those boundaries. Thus,

$$\left.\frac{dX}{dx}\right|_0 = 0 = Ak_x cos(0) - Bk_x sin(0) = A \qquad \text{(Eq. 1.12)}$$

Plugging in $A = 0$, we also have:

$$\left.\frac{dX}{dx}\right|_a = 0 = -Bk_x sin(k_x a) \qquad \text{(Eq. 1.13)}$$

Which means that $k_x = \frac{m\pi}{a}$ for $(m = 0, 1, 2, \dots)$. The same process can be used for Y, with $k_y = \frac{n\pi}{b}$ for $(n = 0, 1, 2, \dots)$. We thus have the solution (called the TE_{mn} mode):

$$B_z = B_0 \cos\left(\frac{m\pi x}{a}\right)\cos\left(\frac{n\pi x}{b}\right) \qquad \text{(Eq. 1.14)}$$

By plugging our expressions for k_x and k_y back into $-k_x^2 - k_y^2 + \left(\frac{\omega}{c}\right)^2 - k^2 = 0$, we can find our wave number:

$$k = \sqrt{\left(\frac{\omega}{c}\right)^2 - \pi\left[\left(\frac{m}{a}\right)^2 + \left(\frac{n}{b}\right)^2\right]} \quad \text{(Eq. 1.15)}$$

Note that if:

$$\omega < c\pi\sqrt{\left(\frac{m}{a}\right)^2 + \left(\frac{n}{b}\right)^2} \equiv \omega_{mn} \quad \text{(Eq. 1.16)}$$

then the wave number becomes imaginary. In that case, the wave equation $\boldsymbol{B_0}(x,y)e^{i(kz-\omega t)}$ has a real exponent, and thus attenuates rather than oscillates. The ω_{mn} below which the electromagnetic field undergoes this exponential attenuation is called the cutoff frequency. The lowest cutoff frequency for a rectangular waveguide occurs for the TE_{10} mode: $\omega_{10} = \frac{c\pi}{a}$. Any frequencies lower than this cutoff (ie longer wavelengths) will not propagate through the guide at all.

Since the TE_{10} mode is accounts for most of the electromagnetic energy of a wave incident on the waveguide, the lower order terms are of less interest in practical application to using zero mode waveguides for smFRET experiments. The cutoff frequency for that mode is thus:

$$\omega_{10} < c\pi\sqrt{\left(\frac{1}{a}\right)^2} = \frac{c\pi}{a} \quad \text{(Eq. 1.17)}$$

Since $\omega = \frac{c}{\lambda}$, we can re-express that cutoff frequency as a wavelength, a more common unit for optical lasers. We thus find,

$$\lambda_{10} > \frac{a}{\pi} \quad \text{(Eq. 1.18)}$$

For a square waveguide, $\lambda_{10} = \lambda_{01}$, so any light with wavelength longer than its sides divided by pi will not propagate through the guide, but will instead be exponentially attenuated inside it. For a circular waveguide, the derivation is

This effect underlies the usefulness of zero mode waveguides in smFRET. By constraining the observation volume physically (in the x- and y-axes) and optically (in the z-axis), ZMWs give observation volumes on the order of tens of atto-liters, allowing use of micro-/milli-molar fluorescent substrates without prohibitive background fluorescence.(Moran-Mirabal and Craighead, 2008)

1.12 Zero mode waveguide fabrication and functionalization

Various methods have been used to fabricate zero mode waveguides. The most direct approach is to evaporate a uniform metal film onto a glass or quartz substrate, and then make the wells through focused-ion-beam milling (Wenger et al., 2006), but that is a slow process due to the need to create one aperture at a time. Another approach is to deposit and pattern a mask above the metal film, followed by reactive ion etching (Levene et al., 2003). Alternatively, the ZMW wells can be patterned via negative-electron-beam resists on the substrate which are dissolved after metal deposition (Fig 1.12.1). Compared with reactive ion-etching, this metal lift-off method allows various metal cladding to be used without needing to adapt a plasma etch recipe to each specific metal (Foquet et al., 2008).

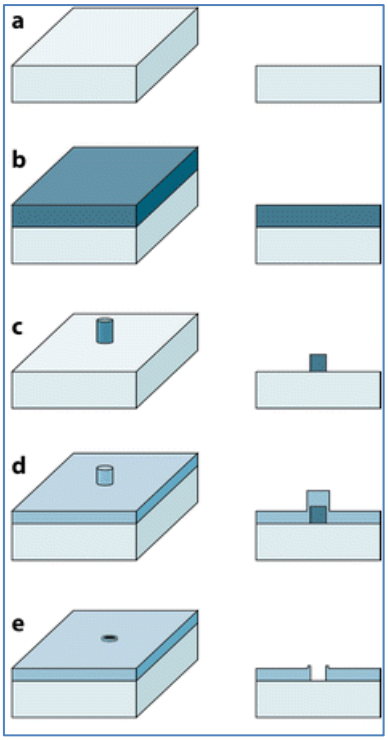

Figure 1.12.1: Schematic of ZMW fabrication via electron beam lithography and metal lift-off method using negative tone resist. (a) A glass or silica substrate is (b) coated with negative tone resist and patterned to result in cross-linked resist, (c) forming pillars and (e) coated with a ~100-nm layer of aluminum. (e) When resist pillars are dissolved, nanoscale ZMW wells remain.(Foquet et al., 2008)

Aluminum is the most commonly used material for the metal cladding, due to its flat transmission and reflection spectrums in the visible wavelengths and its formation of an oxide layer when exposed to the atmosphere. That oxide layer protects the metal from further oxidation, and allows protein adsorption and cell adhesion. Gold has also been used as a common material for ZMWs, particularly when biocompatibility and chemical resistance is beneficial (Liao et al., 2008).

The surfaces of the metal cladding and the glass at the bottom of the wells can be functionalized with different chemical treatments that react non-specifically or specifically to those materials. To study single molecules carrying out complicated reactions in ZMWs, one must fix the enzymes (like the ribosome) onto the glass

surface, rather than allowing them to adsorb to the metal cladding surfaces and side walls. Aluminum surfaces can be blocked against nonspecific protein-surface interactions using bovine serum albumin (BSA)(MacBeath and Schreiber, 2000). However, polyvinyl phosphonic acid (PVPA)(Korlach et al., 2008) provides a more specific method of passivation, which can then be followed by the silane treatment of the glass bottoms of the wells. Silanes are not specific for glass over aluminum when the aluminum had not been previously passivated, emphasizing the importance of the PVPA. The silanes can functionalize the glass bottoms of the wells with molecules like biotin-PEG, providing attachment points for enzymes or other macromolecules for smFRET experiments. An alternative to aluminum and PVPA is to use gold cladding that can be functionalized using thiol chemistry. Thiol reactivity is orthogonal to the silane chemistry used for glass, thus providing another simple passivation scheme (Kinz-Thompson et al., 2013).

2. tRNA fluctuations observed on stalled ribosomes are suppressed during ongoing protein synthesis

2.1 Abstract

The pre-translocation (PRE) complex of the ribosome can undergo spontaneous fluctuations of mRNA and tRNAs between classical and hybrid states, and occupation of the hybrid tRNA positions has been proposed to precede translocation. The classic and hybrid state tRNA positions been extensively characterized when the ribosome is stalled along the messenger RNA by either the absence or the delayed addition of elongation factor G (EF-G), or by the presence of antibiotics or GTP analogs that block translocation. Surprisingly, during multiple ongoing elongation cycles when both EF-G and ternary complexes are present, we found that tRNA positions in PRE complex ribosome do not fluctuate. Instead, they adopt a stationary intermediate structure between the stalled classical and hybrid tRNA positions, as indicated by single molecule fluorescence resonance energy transfer (FRET) between adjacent tRNAs and between A-site tRNA and ribosomal protein L11. These results indicate that EF-G promotes the formation of an intermediate structure during ongoing translation.

2.2 Introduction

During protein synthesis, tRNAs successively occupy three sites on the ribosome: A (aminoacyl), P (peptidyl), and E (exit). After an aminoacylated tRNA (aa-tRNA) enters the A-site, a new peptide bond is formed as the nascent peptide chain is transferred from the P-site tRNA to the A-site tRNA. Translocation of the resulting pre-translocation (PRE) complex of the ribosome, which is a shift of the mRNA by one 3-base codon relative to the ribosome and movement of the tRNAs from the A and P sites to the P and E sites, respectively, is catalyzed by elongation factor G (EF-G). The resulting post-translocation (POST) complex awaits delivery of the next aa-tRNA into the A-site to start a subsequent cycle of elongation.

Although ribosomes in the PRE complex can undergo spontaneous translocation, they do so at a rate orders of magnitude slower than that achieved by EF-G catalysis (Cukras et al., 2003; Fredrick and Noller, 2003; Gavrilova and Spirin, 1971; Gavrilova et al., 1976; Pestka, 1969). The stalled PRE complex formed in the absence of EF-G fluctuates between so-called “classical” and “hybrid” states (Bretscher,1968; Moazed and Noller, 1989; Blanchard et al., 2004). In this earlier work, the “classical” tRNA position referred to the A/A, P/P conformation of bound tRNAs, where the first and second letters represent binding sites on the 30S and 50S subunits, respectively, and the “hybrid” tRNA position referred to a conformation containing tilted tRNAs, in which the tRNAs bound in the A/P and P/E state.

The hybrid state was proposed to be an intermediate between the classical PRE state and the POST complex in which the tRNAs are bound in the P/P and E/E positions. Subsequently, the definition of the hybrid state has broadened, largely as a result of structural studies (Brilot et al., 2013; Fischer et al., 2010; Ramrath et al., 2013) and FRET measurements both at the single molecule (Adio et al., 2015; Chen et

al., 2011, 2013, Cornish et al., 2009a, 2009b, Fei et al., 2008, 2009, 2011, Munro et al., 2007b, 2010a) and ensemble (Belardinelli et al., 2016; Sharma and Chowdhury, 2011) levels. These studies have led to the identification of several distinct hybrid states of the PRE complex containing tRNAs in somewhat different positions on the ribosomes along the path between the classical PRE complex and the POST complex. The large and small subunits exhibit internal rotational movements, and the two subunits rotate ~8° relative to each other(Agirrezabala et al., 2008; Fischer et al., 2010). Frank and Gonzalez (2010) proposed that tRNA tilting and subunit rotations could be considered as coupled, defining two main global states: classical un-rotated states with non-tilted tRNAs, and hybrid rotated states with tilted tRNAs (Frank and Gonzalez, 2010). However, recent evidence demonstrates that tRNA tilting, subunit rotations, and L1 stalk motions are temporally distinct processes (Belardinelli et al., 2016; Munro et al., 2010a, 2010b; Sharma et al., 2016) that are not tightly coupled.

Here we present single molecule fluorescence resonance energy transfer (FRET) measurements focused on changes in tRNA positions on the ribosome during EF-G catalyzed translocation, as determined by changes in FRET efficiency between two ribosome-bound tRNAs, and between a tRNA and L11, a ribosomal protein located near the A-site. Earlier studies of tRNA movement during EF-G catalyzed translocation, obtained with ribosomes that had been stalled or slowed by either the absence of EF-G·GTP (Fischer et al., 2010; Kim et al., 2007; Munro et al., 2007a; Ning et al., 2014; Wang et al., 2011), or the replacement of EF-G·GTP by EF-G·GDPNP (Cornish et al., 2009b; Fei et al., 2008, 2009, 2011), or the addition of antibiotics (Adio et al., 2015; Ermolenko et al., 2007; Lin et al., 2015; Zhou et al., 2014), supported the notion that classical-hybrid transition in PRE complexes plays an important role in translocation. However, by artificially stalling translation, these

systems imperfectly model the translocation process during multiple ongoing elongation cycles, when EF-G·GTP and ternary complexes, (aa-tRNA·EF-Tu·GTP) bind in quick succession. A study that did observe ongoing elongation (Chen et al., 2013) at low EF-G concentrations observed extremely slow fluctuations, but monitored subunit rotations rather than tRNA positions.

In contrast to the results obtained with stalled PRE complexes, our previous single molecule FRET study gave results indicating that tRNA positions in PRE complexes do not fluctuate during ongoing translation of a full-length protein (Rosenblum et al., 2013). However, that study used a time resolution similar to the measured rate of classical-hybrid tRNA fluctuations, which could have prevented their detection, and was only performed at a single EF-G·GTP concentration. In the present work, we overcome these limitations by detecting ongoing translation of a model polypeptide at higher time resolution, and at varying levels of EF-G·GTP. Our new results, presented below, show that at EF-G·GTP concentrations close to that in cells, tRNA positions in PRE complexes do not fluctuate but rather adopt a structure with a single dominant FRET efficiency that falls between the values for the stalled classical and hybrid tRNA positions, or close to the classical value. Fluctuations between classical and hybrid tRNA positions in PRE complexes only become apparent at EF-G·GTP levels well below measured K_m values for the translocation activity of EF-G (Pan et al., 2007; Savelsbergh et al., 2003).

2.3 Results

2.3.1 Design of smFRET experiments

Below we present the results of smFRET experiments designed to test whether fluctuations observed in stalled PRE complexes prior to addition of EF-G are also present in PRE complexes formed during ongoing protein synthesis when EF-G is continuously present. For this purpose we use ribosomes programmed with the two mRNAs shown in Table 2.1, with different fluorescent labelling schemes that reported the dynamics of FRET between A-site tRNA and L11 or between A- and P-site tRNAs. With mRNA-6,7 we used: a) ribosomes labelled with Cy5-L11 and Val-tRNA^{Val}(Cy3) [V^7(Cy3)-L11(Cy5)], b) unlabelled ribosomes with both Phe-tRNA^{Phe}(Cy5) and Val-tRNA^{Val}(Cy3) [F^6(Cy5)-V^7(Cy3)], unlabelled ribosomes with both Phe-tRNA^{Phe}(Cy3) and Val-tRNA^{Val}(Cy5) [F^6(Cy3)-V^7(Cy3)], d) ribosomes labelled with Cy5-L11 and Phe-tRNA^{Phe}(Cy3) [F^6(Cy3)-L11(Cy5)]. With mRNA-2,3 we used: e) ribosomes labelled with Cy5-L11 and Val-tRNA^{Val}(Cy3) [V^3(Cy3)-L11(Cy5)], f) ribosomes labelled with Cy3-L11 and Val-tRNA^{Val}(Cy5) [V^3(Cy5)-L11(Cy3)], g) ribosomes labelled with Cy5-L11 and Phe-tRNA^{Phe}(Cy3) [F^2(Cy3)-L11(Cy5)]. In the text that follows we refer to PRE and POST complexes with numbers that correspond to the length of the ribosome-bound peptide. Thus, for example, the PRE-6 or POST-6 complex has a hexapeptidyl-tRNA bound in the A- or P-site, respectively.

2.3.2 smFRET in stalled PRE complexes

Consistent with previous results of ourselves and others (Blanchard et al., 2004; Chen et al., 2011), many stalled PRE complexes formed in the absence of EF-G·GTP fluctuated between classical and hybrid tRNA positions that have high and low FRET efficiencies, as identified by Hidden Markov analysis (HaMMy program, McKinney et al., 2006). For the V^7(Cy3)-L11(Cy5) (Fig. 2.1A-C) and F^6(Cy5)-

V^7(Cy3) (Fig. 2.2A-C) experiments, Val-$tRNA^{Val}$(Cy3) ternary complex was added to a sample containing stalled POST-6 complexes (with P-site bound fMYYYYF-$tRNA^{Phe}$) in the absence of EF-G. The FRET efficiency distribution for both FRET pairs had two clear peaks that were fit with double Gaussian functions to provide the L11-tRNA and tRNA-tRNA classical and hybrid FRET efficiencies, consistent with previous measurements (Chen et al., 2011). We also used HaMMY to select high and low FRET values from the stalled FRET recordings. The distributions and peak values from the intensities identified as high and low by HaMMy were almost identical to the ones obtained by fitting two Gaussian components to the full distributions. Similar results were obtained for the stalled PRE complexes formed in the F^6(Cy3)-V^7(Cy3) (Table 2.1C, Fig 2.5C), F^6(Cy3)-L11(Cy5) (Table 2.1D, Fig 2.6C), V^3(Cy3)-L11(Cy5) (Table 1E, Fig 2.5J), V^3(Cy5)-L11(Cy3) (Table 1F, Fig 2.5Q), F^2(Cy3)-L11(Cy5) (Table 1G, Fig 2.6L) experiments.

2.3.3 smFRET in PRE complexes formed during ongoing translation at 2 μM EF-G

When the V^7(Cy3)-L11(Cy5) experiment was performed during ongoing translation (Fig. 2.1D-F), Val-$tRNA^{Val}$(Cy3) ternary complex binding to the A-site of the transiently formed POST-6 complex generated an initial FRET efficiency centered at 0.65 (Fig 2.1F), attributable to PRE-7 complex formation, and was succeeded by a period with much lower FRET efficiency (<0.15), as expected for translocation of peptidyl-$tRNA^{Val}$(Cy3) to the P-site (Fig. 2.1E). No FRET signal was observed when Phe-$tRNA^{Phe}$, cognate to codon 6, was omitted from the reaction mixture, demonstrating that the observed FRET events depend on translation through codon 7 cognate to Val-$tRNA^{Val}$(Cy3). Importantly, contour plots derived from ongoing traces

synchronized to the start or end of the FRET events (Fig. 2.1H, I) show a single dominant state throughout their duration, with no detectable transition to a lower efficiency similar to hybrid V^7(Cy3)-L11(Cy5) FRET prior to translocation**.** The tRNA-L11 FRET efficiencies in ongoing PRE complexes are intermediate between the corresponding stalled classical and hybrid FRET efficiencies (Table 2.1), but closer to the classical value. Similar results were obtained during ongoing translation in the F^6(Cy3)-L11(Cy5) (Table 2.1D, Fig 2.6F), V^3(Cy3)-L11(Cy5) (Table 2.1E, Fig 2.5M), V^3(Cy5)-L11(Cy3) (Table 2.1F, Fig 2.5T), F^2(Cy3)-L11(Cy5) (Table 2.1G, Fig 2.6O) experiments.

To distinguish whether the single FRET state in ongoing translation is the result of immediate binding of the ternary complex (TC) to the previous POST state or due to the presence of EF-G when the TC binds, we caused elongation to pause in the POST-6 complex in the V^7(Cy3)-L11(Cy5) by waiting 5 minutes before injecting Val-$tRNA^{Val}$(Cy3)·EF-Tu·GTP, and EF-G·GTP together. This experiment gave the same single, non-fluctuating intermediate FRET state, and very similar translocation kinetics as the true ongoing translation case (Figs. 2.1E, F, 2.7C). This result indicates that fluctuation suppression and intermediate FRET state formation both depend on the presence of EF-G, and that such co-dependence is not a result of the short lifetime of the POST complex during ongoing translation.

During ongoing translation, the F^6(Cy5)-V^7(Cy3) experiment (Fig. 2.2D-F) also displays a single, non-fluctuating FRET signal (Figs. 2.2E, F) centered at an efficiency of 0.59, also intermediate to the values found for the classical and hybrid tRNA positions (Table 2.1B, Fig 2.2C). We attribute this FRET signal to both the initially formed PRE-7 complex and the initially formed POST-7 complex following translocation, and its disappearance to dissociation of $tRNA^{Phe}$(Cy5) from the

ribosome. Similar results were obtained during ongoing translation in the F^6(Cy3)-V^7(Cy5) experiment (Table 2.1C, Figs. 2.5, A-G). That the PRE-7 complex and the initially formed POST-7 complex are not distinguishable based on tRNA-tRNA FRET efficiency is not surprising, since we have previously shown that the FRET efficiency in a POST complex formed on addition of EF-G to a stalled PRE complex(Chen et al., 2011), like the FRET efficiency of the ongoing PRE complex measured in this work (Table 2.1), has an intermediate value between those found for the classic and hybrid PRE complexes.

For all of the FRET pairs at 2 μM EF-G, dwell time distributions of the ongoing PRE complexes had fast phases averaging <500 ms (Fig 2.7, Table 2.4), comparable to previous measurements of *in vitro* PRE complex occupancy (Rosenblum et al., 2013; Takahashi et al., 2012; Uemura et al., 2010; Underwood et al., 2005), as well as components averaging 1.2 – 2.5 s that represent a slower-translocation subpopulation, as previously reported (Wang et al., 2012; Wasserman et al., 2016). We found that for each FRET pair, the fast and slow translocating ribosomes have the same, non-fluctuating, intermediate FRET value (not shown).

The synchronized contour plots shown in Figs. 2.1H, 2.1I, 2.2H and 2.2I provide strong evidence for the non-fluctuating nature of the PRE complex FRET signals during ongoing translation at the 30 s^{-1} time scale of the experiment. Many ongoing PRE complexes would have been observed to fluctuate had the classical-hybrid kinetics remained the same for ongoing PRE complexes as in the stalled case (Table 2.2, estimated as described in Methods, "Dwell time fitting and comparison"). At 2 μM EF-G, ≤ 5% of the ongoing traces in this study fluctuated during their average PRE state lifetimes of 1-2 s, which would require a fluctuation rate slower than 0.03 s^{-1}, rather than the 0.6-2.3 s^{-1} that we observe here in stalled ribosomes. In

earlier studies of stalled conditions, we observed that binding of EF-G suppresses classic-hybrid fluctuations 5-60-fold from rates of 0.6 - 1 s^{-1} (Chen et al., 2011, 2012), a range compatible with the suppression of fluctuations noted here in ongoing conditions. While those earlier results demonstrated that EF-G terminated fluctuations that were already underway, our present results demonstrate that EF-G also prevents the initiation of such fluctuations.

Additional evidence was provided by determining the cross-correlation between the donor and acceptor intensities during PRE complex dwell time (Figs. 2.1J, 2.2J; also see Supplementary Information, Donor-acceptor cross-correlation). Decreased inter-probe distance within a FRET pair causes the acceptor emission to increase and the donor emission to decrease, due to increased energy transfer. Conversely, increased distance lowers acceptor fluorescence and increases donor intensity. Thus, distance fluctuations are associated with anti-correlated donor and acceptor intensities. The stalled traces exhibited negative cross correlation due to their fluctuations, as expected (Fig. 2.1J, 2.2J first red data point at lag = 0). In contrast, the ongoing traces showed non-negative cross-correlation at the 30 s^{-1} time scale (Fig 2.1J, 2.2J, first green data point at lag = 0), demonstrating that the ongoing PRE complex does not fluctuate.

That conclusion is further supported by time lag analysis of the decay of cross-correlations (Figs. 2.1J and 2.2J, Table 2.6). A temporal cross-correlogram was calculated by relative shifting of the two recordings by successive frame numbers and re-calculating the cross-correlation coefficient for each shift (ie lag). For the stalled traces, their anti-correlation decays to zero as a function of lag, with an average correlation time that is equal to the reciprocal of the sum of the fluctuating rate constants, here 0.52 s and 0.31 s (Figs. 2.1J and 2.2J, red curves, Table 2.6). For

ongoing PRE complex traces, the first point in the cross-correlogram (the covariance) is positive due to fluctuations in laser intensity, and the rest of the cross-correlogram is zero when that effect of common mode noise is eliminated and absence of any donor-acceptor correlation is confirmed.

The non-fluctuating intermediate FRET state was also clearly shown in histograms displaying the average FRET efficiencies of all traces (Fig. 2.8,A-D, event histograms) as in histograms plotted from all frames (temporal histograms, Figs. 2.1F, 2.2F, 2.5F, M, T, 2.6F, O). Event histograms reduce frame-to-frame noise that could have resulted in an apparent merger of FRET distributions arising from a bimodal population of PRE complexes, indicating that the ongoing PRE FRET state is not an artifactual merger of the classical and hybrid tRNA positions.

2.3.4 Lowering EF-G concentration during ongoing translation increases fluctuation within the PRE complex.

The experiments displayed in Figs. 2.1 and 2.2 demonstrate nearly complete absence of fluctuations (1-4%) in PRE complexes formed during ongoing translation in the presence of 2 μM EF-G. However, as EF-G concentration is decreased these percentages rise (Fig. 2.1K, 2.2K, Table 2.3), presumably due to delayed binding of EF-G to the PRE complex. Further, the PRE complexes that did fluctuate at lower EF-G concentrations followed a classical-hybrid trajectory (Fig 2.8, J-O pre-synchronized) as in the absence of EF-G (Fig 2.8, E-G). Fluctuating PRE complexes at low EF-G concentrations translocated from either state as previously observed (Adio et al., 2015; Chen et al., 2011, 2013), with the proportion of translocation from the hybrid tRNA positions gradually increasing at lower EF-G concentrations (Fig 2.8, J-O, post-synchronized).

mRNA	Row letter	Fluorescent Labeling Scheme	FRET Pair (green = Cy3, red = Cy5)	FRET Efficiencies			$\frac{E_{ongoing} - E_{hybrid}}{E_{classical} - E_{hybrid}}$
				Stalled-PRE Classic	Stalled-PRE Hybrid	Ongoing	
mRNA-6,7	A	AUG UAU UAU UAU UAU UUC GUG CGU UAU UAU UAU UAU UAU fMet Tyr Tyr Tyr Tyr Phe Val Arg Tyr Tyr Tyr Tyr Tyr 1 2 3 4 5 6 7 8 9 10 11 12 13	V^7 - L11	0.73 ± 0.008 (Fig 1C)	0.49 ± 0.020 (Fig 1C)	0.65 ± 0.004 (Fig 1F)	0.67
	B	AUG UAU UAU UAU UAU UUC GUG CGU UAU UAU UAU UAU UAU fMet Tyr Tyr Tyr Tyr Phe Val Arg Tyr Tyr Tyr Tyr Tyr 1 2 3 4 5 6 7 8 9 10 11 12 13	F^6 - V^7	0.68 ± 0.007 (Fig 2C)	0.39 ± 0.009 (Fig 2C)	0.58 ± 0.012 (Fig 2F)	0.66
	C	AUG UAU UAU UAU UAU UUC GUG CGU UAU UAU UAU UAU UAU fMet Tyr Tyr Tyr Tyr Phe Val Arg Tyr Tyr Tyr Tyr Tyr 1 2 3 4 5 6 7 8 9 10 11 12 13	F^6 - V^7	0.73 ± 0.007 (Fig S1C)	0.40 ± 0.013 (Fig S1C)	0.57 ± 0.018 (Fig S1F)	0.52
	D	AUG UAU UAU UAU UAU UUC GUG CGU UAU UAU UAU UAU UAU fMet Tyr Tyr Tyr Tyr Phe Val Arg Tyr Tyr Tyr Tyr Tyr 1 2 3 4 5 6 7 8 9 10 11 12 13	F^6 - L11	0.73 ± 0.006 (Fig S2C)	0.43 ± 0.009 (Fig S2C)	0.69 ± 0.014 (Fig S2F)	0.87
mRNA-2,3	E	AUG UUC GUG CGU UAU UAU UAU UAU UAU UAU UAU UAU UAU fMet Phe Val Arg Tyr Tyr Tyr Tyr Tyr Tyr Tyr Tyr Tyr 1 2 3 4 5 6 7 8 9 10 11 12 13	V^3 - L11	0.73 ± 0.005 (Fig S1J)	0.46 ± 0.018 (Fig S1J)	0.66 ± 0.011 (Fig S1M)	0.75
	F	AUG UUC GUG CGU UAU UAU UAU UAU UAU UAU UAU UAU UAU fMet Phe Val Arg Tyr Tyr Tyr Tyr Tyr Tyr Tyr Tyr Tyr 1 2 3 4 5 6 7 8 9 10 11 12 13	V^3 - L11	0.70 ± 0.009 (Fig S1Q)	0.49 ± 0.030 (Fig S1Q)	0.63 ± 0.020 (Fig S1T)	0.67
	G	AUG UUC GUG CGU UAU UAU UAU UAU UAU UAU UAU UAU UAU fMet Phe Val Arg Tyr Tyr Tyr Tyr Tyr Tyr Tyr Tyr Tyr 1 2 3 4 5 6 7 8 9 10 11 12 13	F^2 - L11	0.74 ± 0.007 (Fig S2L)	0.43 ± 0.009 (Fig S2L)	0.68 ± 0.012 (Fig S2O)	0.82

Table 2.1: mRNAs and labeling schemes for comparison of tRNA position when stalled or during ongoing translation via smFRET. mRNA-6,7 and mRNA-2,3 displayed in the table were used to program unlabelled ribosomes(rows b,c), L11(Cy5) ribosomes (rows a, d, e, g), and L11(Cy3) ribosomes (row f) for smFRET experiments using the FRET pairs stated in the table, corresponding to the red or green codons in the sequences. PRE complexes were stalled by the absence of EF-G and used to form two-peaked FRET distributions fit with double Gaussian functions, giving the high and low FRET peaks corresponded to the classical and hybrid tRNA positions. The cumulative peak centers of those experiments (as well as the SEMs of the peaks from multiple replicate experiments) are displayed in the table. Experiments were also conducted during ongoing translation in the presence of 2 μM EF-G, which yielded single-peaked FRET distributions whose cumulative peak centers and SEM from multiple replicate experiments are also displayed. Those single peaks during ongoing translation had FRET efficiencies between the stalled classical and hybrid values, as expressed in the ratio $(E_{ongoing} - E_{hybrid})/(E_{classical} - E_{hybrid})$.

Figure 2.1

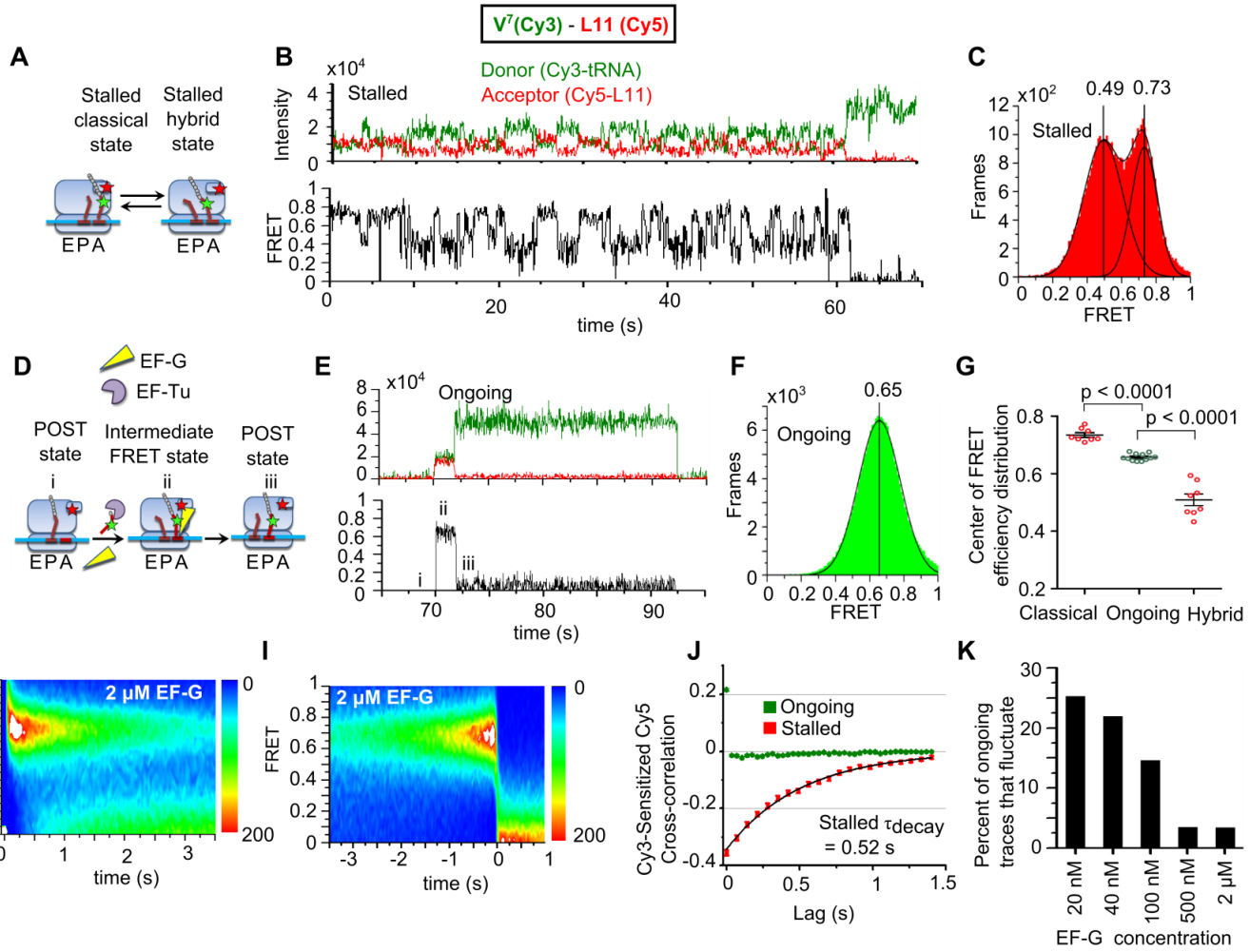
A
Stalled classical state
Stalled hybrid state
EPA
EPA
B
V7(Cy3) - L11 (Cy5)
x10^4
Stalled
Donor (Cy3-tRNA)
Acceptor (Cy5-L11)
Intensity
FRET
time (s)
C
x10^2
0.49 0.73
Stalled
Frames
FRET
D
EF-G
EF-Tu
POST state
Intermediate FRET state
POST state
i
ii
iii
EPA
EPA
EPA
E
x10^4
Ongoing
time (s)
F
x10^3
0.65
Ongoing
Frames
FRET
G
p < 0.0001
p < 0.0001
Center of FRET efficiency distribution
Classical
Ongoing
Hybrid
H
2 μM EF-G
FRET
time (s)
I
2 μM EF-G
FRET
time (s)
J
Ongoing
Stalled
Stalled τdecay = 0.52 s
Cy3-Sensitized Cy5 Cross-correlation
Lag (s)
K
Percent of ongoing traces that fluctuate
20 nM
40 nM
100 nM
500 nM
2 μM
EF-G concentration

Figure 2.1: L11(Cy5) ribosomes were programmed with mRNA-6,7 (Table 1) and undergo FRET with Val-tRNA^{Val}(Cy3). **(A)** Schematic of classical/hybrid equilibrium of a stalled ribosome. **(B)** Representative FRET recording**. (C)** Frames of fluctuating stalled traces formed a two-peaked distribution fit with a double Gaussian function (n = 592 molecules). For **(D-K),** 2 μM EF-G was present during ongoing translation. **(D)** Reaction scheme for ongoing translation, **(E**) a representative trace with the following FRET states: **(i)** the POST state after the ribosome has translated through the 5th (Tyr) and 6th (Phe) codons, and peptidyl-tRNA^{Phe} residing in the P-site; **(ii)** the single, non-fluctuating intermediate PRE state; and **(iii)** the POST complex following translocation. **(F)** Frames of traces during ongoing translation formed a peaked PRE state distribution fit with a single Gaussian component (n = 3664 molecules). **(G)** FRET distribution peak centers for ongoing translation were statistically different from the stalled classical and hybrid peaks over multiple replicate experiments (mean ± SEM)**.** FRET recordings were shifted in time to synchronize their beginnings (**H**, pre-synchronized) or terminations (**I**, post-synchronized) and overlaid to form contour plots**. (J)** Cross-correlation of donor and acceptor intensities as a function of temporal lag for stalled ribosomes (red) and ribosomes during ongoing translation (green); SEM <0.01, too small to be visible on the graph. **(K)** Lowering EF-G concentration increased the percentage of fluctuating PRE complexes during ongoing translation

Figure 2.2

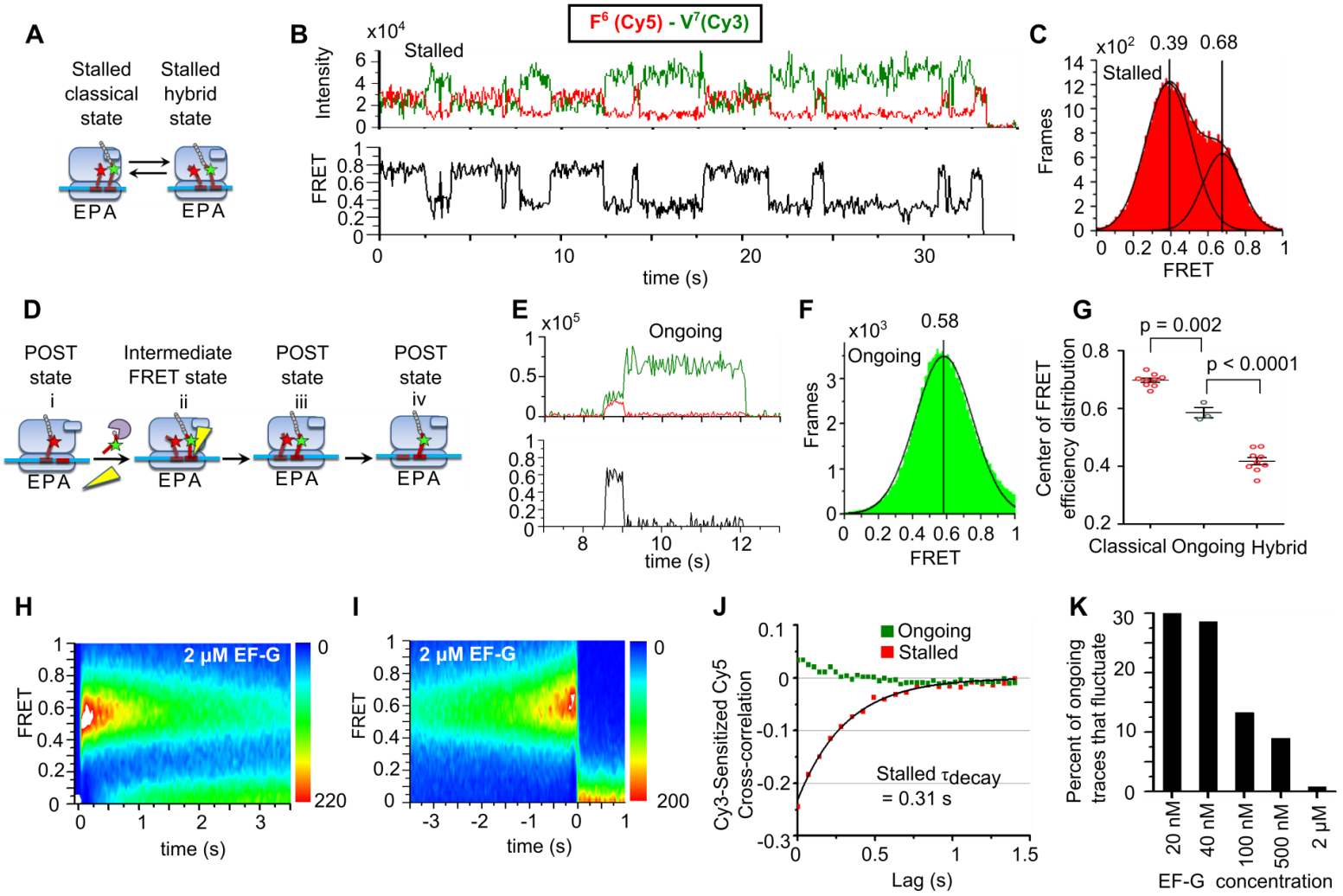
A
Stalled classical state
Stalled hybrid state
EPA
EPA
B
F6 (Cy5) - V7(Cy3)
x10^4
Stalled
Intensity
FRET
time (s)
C
x10^2
0.39
0.68
Stalled
Frames
FRET
D
POST state i
Intermediate FRET state ii
POST state iii
POST state iv
EPA
EPA
EPA
EPA
E
x10^5
Ongoing
time (s)
F
x10^3
0.58
Ongoing
Frames
FRET
G
p = 0.002
p < 0.0001
Center of FRET efficiency distribution
Classical
Ongoing
Hybrid
H
2 µM EF-G
FRET
time (s)
I
2 µM EF-G
FRET
time (s)
J
Ongoing
Stalled
Cy3-Sensitized Cy5 Cross-correlation
Stalled τdecay = 0.31 s
Lag (s)
K
Percent of ongoing traces that fluctuate
20 nM
40 nM
100 nM
500 nM
2 µM
EF-G concentration

Figure 2.2: Unlabelled ribosomes were programmed with mRNA-6,7 (Table 1) and Phe-tRNA^{Phe}(Cy5) at codon 6 undergoes FRET with Val-tRNA^{Val}(Cy3) at codon 7. **(A)** Schematic of classical/hybrid equilibrium of a stalled ribosome. **(B)** Representative FRET recording**. (C)** Frames of fluctuating stalled traces formed a two-peaked distribution fit with a double Gaussian function (n = 531 molecules). For **(D-K),** 2 μM EF-G is present during ongoing translation. **(D)** Reaction scheme for ongoing translation, **(E**) a representative trace with the following FRET states: **(i)** the POST state after the ribosome has translated through the 5th (Tyr) and 6th (Phe) codons, with peptidyl-tRNA^{Phe} residing in the P-site; **(ii, iii)** the single non-fluctuating intermediate PRE state and the initial POST state, which have similar FRET efficiencies (Chen et al., 2011); and **(iv)** the POST state following dissociation of tRNA^{Phe}(Cy5) from the E-site. **(F)** Frames of traces during ongoing translation formed a peaked PRE state distribution fit with a single Gaussian component (n = 2359 molecules). **(G)** FRET distribution peak centers for ongoing translation were statistically different from the stalled classical and hybrid peaks over multiple replicate experiments (mean ± SEM)**.** FRET recordings were shifted in time to synchronize their beginnings (**H**, pre-synchronized) or terminations (**I**, post-synchronized) and overlaid to form contour plots**. (J)** Cross-correlation of donor and acceptor intensities as a function of temporal lag for stalled ribosomes (red) and ribosomes during ongoing translation (green); SEM <0.01, too small to be visible on the graph. **(K)** Lowering EF-G concentration increased the percentage of fluctuating PRE complexes during ongoing translation**.**

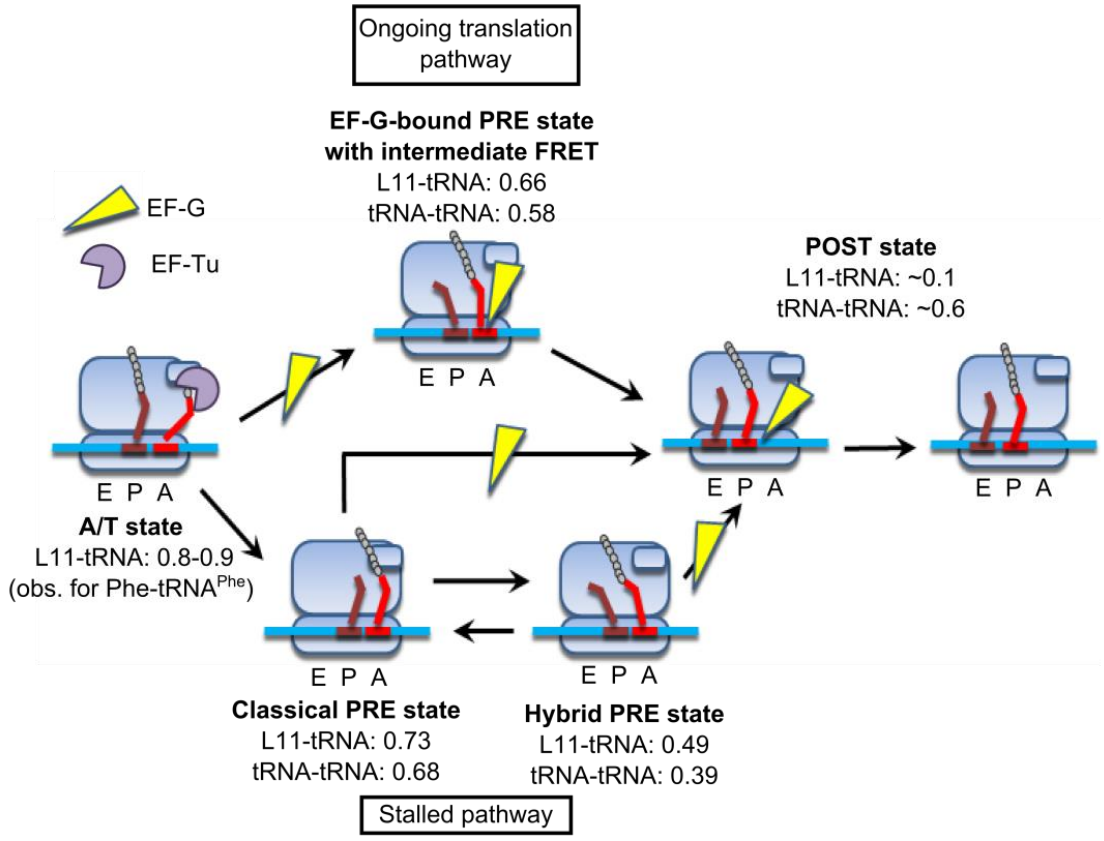

Figure 2.3. **Schematic of divergent translocation pathways**. In the ongoing translation pathway (top), newly formed PRE complexes occupy at an intermediate FRET state in the presence of EF-G, and quickly translocate. In the stalled pathway (bottom), relaxation of newly formed PRE complexes to a reversible distribution between stalled classical and hybrid tRNA positions in the absence of EF-G at low EF-G concentration. EF-G can interact with either state to promote translocation.

Figure 2.5

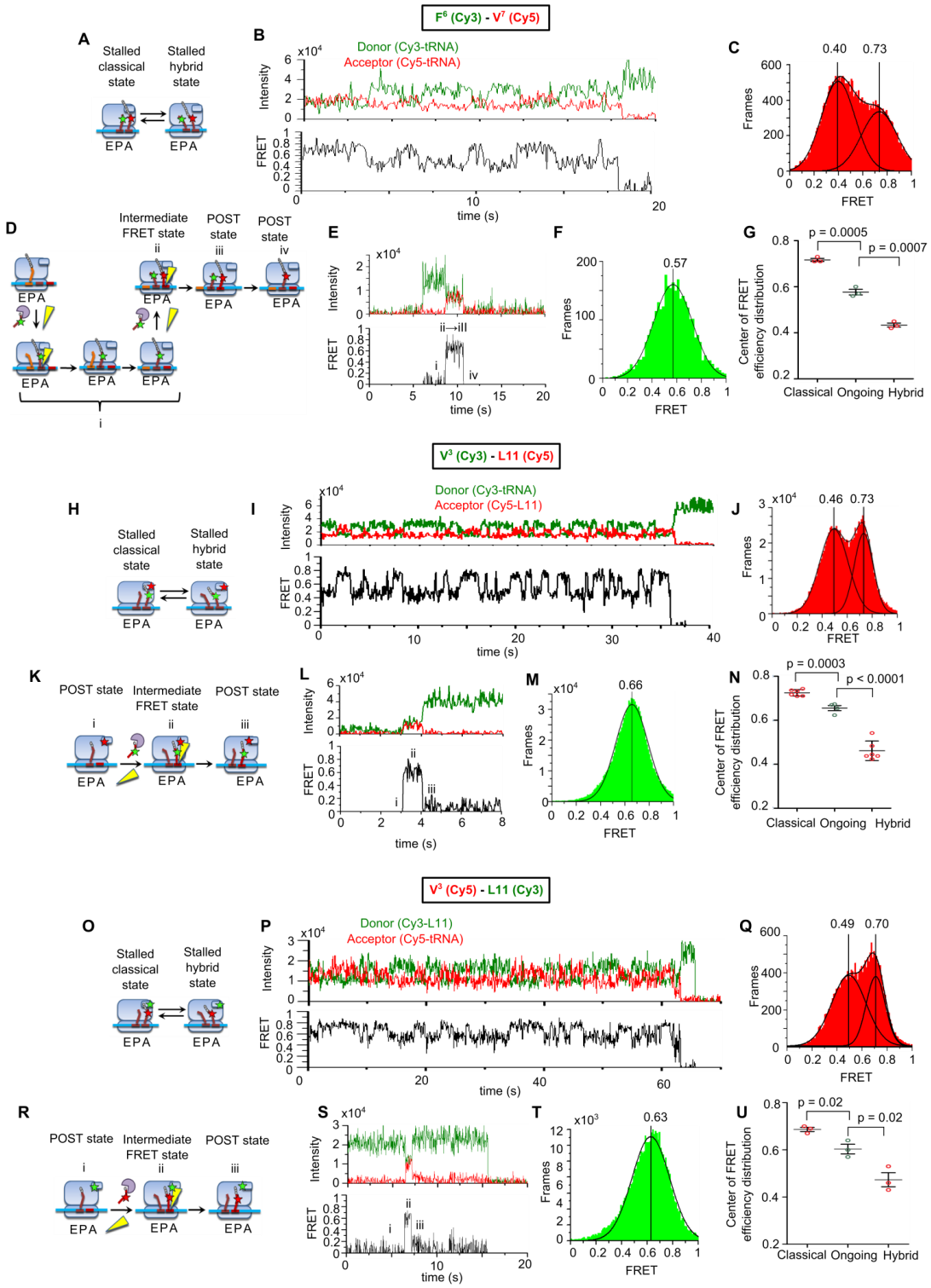
F6 (Cy3) - V7 (Cy5)
A
Stalled classical state
Stalled hybrid state
EPA
EPA
B
Donor (Cy3-tRNA)
Acceptor (Cy5-tRNA)
Intensity
FRET
time (s)
C
0.40
0.73
Frames
FRET
D
Intermediate FRET state
ii
POST state
iii
POST state
iv
i
E
ii→iii
F
0.57
G
p = 0.0005
p = 0.0007
Center of FRET efficiency distribution
Classical
Ongoing
Hybrid
V3 (Cy3) - L11 (Cy5)
H
I
Donor (Cy3-tRNA)
Acceptor (Cy5-L11)
J
0.46
0.73
K
POST state
Intermediate FRET state
POST state
L
M
0.66
N
p = 0.0003
p < 0.0001
V3 (Cy5) - L11 (Cy3)
O
P
Donor (Cy3-L11)
Acceptor (Cy5-tRNA)
Q
0.49
0.70
R
S
T
0.63
U
p = 0.02
p = 0.02

Figure 2.5. Unlabelled ribosomes were programmed with mRNA-6,7 (Table 1) and Phe-tRNA^{Phe}(Cy3) at codon 6 underwent FRET with Val-tRNA^{Val}(Cy5) at codon 7. **(A)** Schematic of classical/hybrid equilibrium of a stalled ribosome with **(B)** representative FRET recording**.** **(C)** Frames of fluctuating stalled traces formed a two-peaked distribution fit with a double Gaussian function (n = 497 molecules). For **(D-F),** EF-G was present at 2 μM during ongoing translation. **(D)** Reaction scheme for ongoing translation, **(E**) a representative trace with the following FRET states: **(i)** an entire translocation cycle with Phe-tRNA^{Phe}(Cy3) entering the A-site and translocating to the P-site, resulting in a POST state after the ribosome has translated through the 5th (Tyr) and 6th (Phe) codons; **(ii, iii)** the single non-fluctuating intermediate PRE state and the initial POST state, which have similar FRET efficiencies (Chen et al., 2011); and **(iv)** the POST state following dissociation of tRNA^{Phe}(Cy5) from the E-site. **(F)** Frames of traces during ongoing translation formed a peaked PRE state distribution fit with a single Gaussian component (n = 200 molecules). **(G)** FRET distribution peak centers for ongoing translation were statistically different from the stalled classical and hybrid peaks over multiple replicate experiments (mean ± SEM)**.** Ribosomes with labeled L11 were programmed with mRNA-2,3 (Table 1) and underwent FRET with Val-tRNA^{Val}; **(H-N)** corresponds to V^3(Cy3)-L11(Cy5) FRET, while **(O-T)** corresponds to V^3(Cy5)-L11(Cy3) FRET. **(H, O)** Schematic of classic/hybrid equilibrium of stalled ribosomes with **(I, P)** representative FRET recordings**. (J, Q)** Frames of fluctuating stalled traces formed two-peaked distributions fit with double Gaussian functions (**J,** n = 541 molecules, **Q,** n = 139 molecules). For **(K-M)** and **(R-T),** EF-G was present at 2 μM during ongoing translation. **(K, R)** Reaction scheme for ongoing translation, **(L, S)** representative FRET recordings with the following FRET states: **(i)** the POST state after the ribosome has translated through the 1st (fMet) and 2nd (Phe) codons, with peptidyl-tRNA^{Phe} residing in the P-site; **(ii)** the single, non-fluctuating intermediate PRE state; and **(iii)** the POST complex following translocation. **(M, T)** Frames of traces during ongoing translation formed peaked PRE state distributions each fit with a single Gaussian component (**M,** n = 2157 molecules; **T,** n = 319 molecules). **(N, U)** FRET distribution peak centers for ongoing translation were statistically different from the stalled classical and hybrid peaks over multiple replicate experiments (mean ± SEM)**.**

Figure 2.6

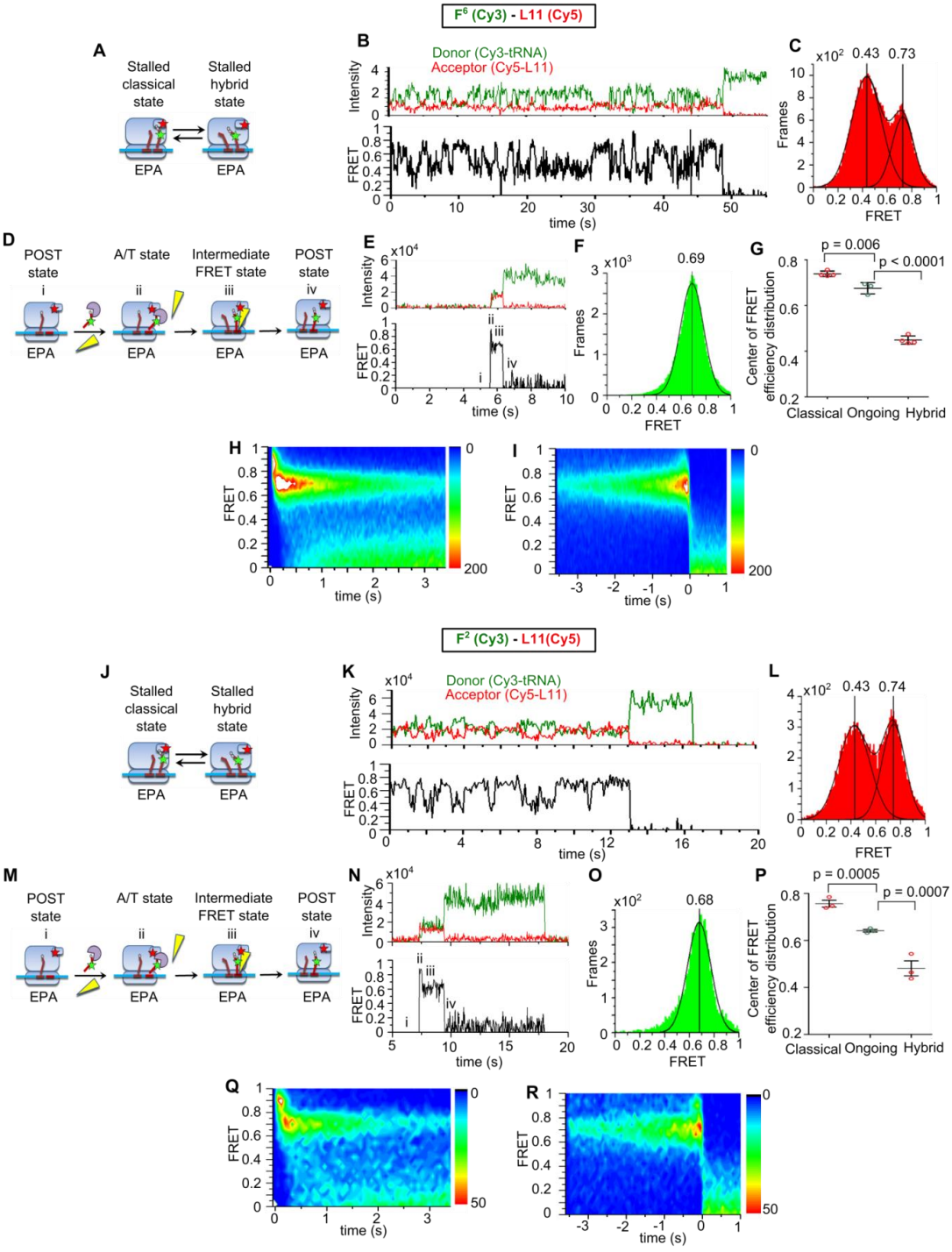
F6 (Cy3) - L11 (Cy5)
A
Stalled classical state
Stalled hybrid state
EPA
EPA
B
Donor (Cy3-tRNA)
Acceptor (Cy5-L11)
Intensity
FRET
time (s)
C
x10² 0.43 0.73
Frames
FRET
D
POST state i
A/T state ii
Intermediate FRET state iii
POST state iv
E
x10⁴
Intensity
FRET
time (s)
F
x10³ 0.69
Frames
FRET
G
p = 0.006
p < 0.0001
Center of FRET efficiency distribution
Classical Ongoing Hybrid
H
FRET
time (s)
I
FRET
time (s)
F2 (Cy3) - L11(Cy5)
J
Stalled classical state
Stalled hybrid state
EPA
EPA
K
x10⁴
Donor (Cy3-tRNA)
Acceptor (Cy5-L11)
Intensity
FRET
time (s)
L
x10² 0.43 0.74
FRET
M
POST state i
A/T state ii
Intermediate FRET state iii
POST state iv
N
x10⁴
Intensity
FRET
time (s)
O
x10² 0.68
Frames
FRET
P
p = 0.0005
p = 0.0007
Center of FRET efficiency distribution
Classical Ongoing Hybrid
Q
FRET
time (s)
R
FRET
time (s)

Figure 2.6. L11(Cy5) ribosomes were programmed with **(A-I)** mRNA-6,7 or **(J-R)** mRNA-2,3 and underwent FRET with Phe-tRNA^{Phe}(Cy3). **(A, J)** Reaction schemes of classical/hybrid equilibrium of stalled ribosomes. **(B, K)** Representative stalled FRET recordings. **(C, L)** Frames of fluctuating stalled traces formed two-peaked distributions fit with double Gaussian functions (**C**, n = 451 molecules, **L,** n = 237 molecules). For **(D-I, M-R),** EF-G was present at 2 μM during ongoing translation. **(D, M)** Reaction schemes for ongoing translation. **(E, N**) Representative traces with the following FRET states: **(i)** the POST state with peptidyl-tRNA^{Tyr} at the 5th codon **(D, E)** or fMet-tRNA^{fMet} at the 1st codon **(M, N)** residing in the P-site; **(ii)** the very high FRET A/T state during Phe-tRNA^{Phe} delivery but before full accommodation (seen in ~20% of traces) as reported by others using Phe-tRNA^{Phe}- L11 FRET (Geggier et al., 2010). A similar state was seen in a small minority (<5%) of Val-tRNA^{Val}- L11 FRET traces during ongoing translation, but was much less prominent; **(iii)** the single, non-fluctuating intermediate PRE state; and **(iv)** the POST complex following translocation. **(F, O)** Frames of traces during ongoing translation formed peaked PRE state distributions each fit with a single Gaussian component (**F**, n = 1423 molecules; **O**, n = 204 molecules). **(G, P)** FRET distribution peak centers for ongoing translation were statistically different from the stalled classical and hybrid peaks over multiple replicate experiments (mean ± SEM). FRET recordings were shifted in time to synchronize their beginnings (**H**, **Q**, pre-synchronized) or terminations (**I, R**, post-synchronized) and overlaid to form contour plots. The color maps indicate number of frames recorded at each FRET value and time.

Figure 2.7

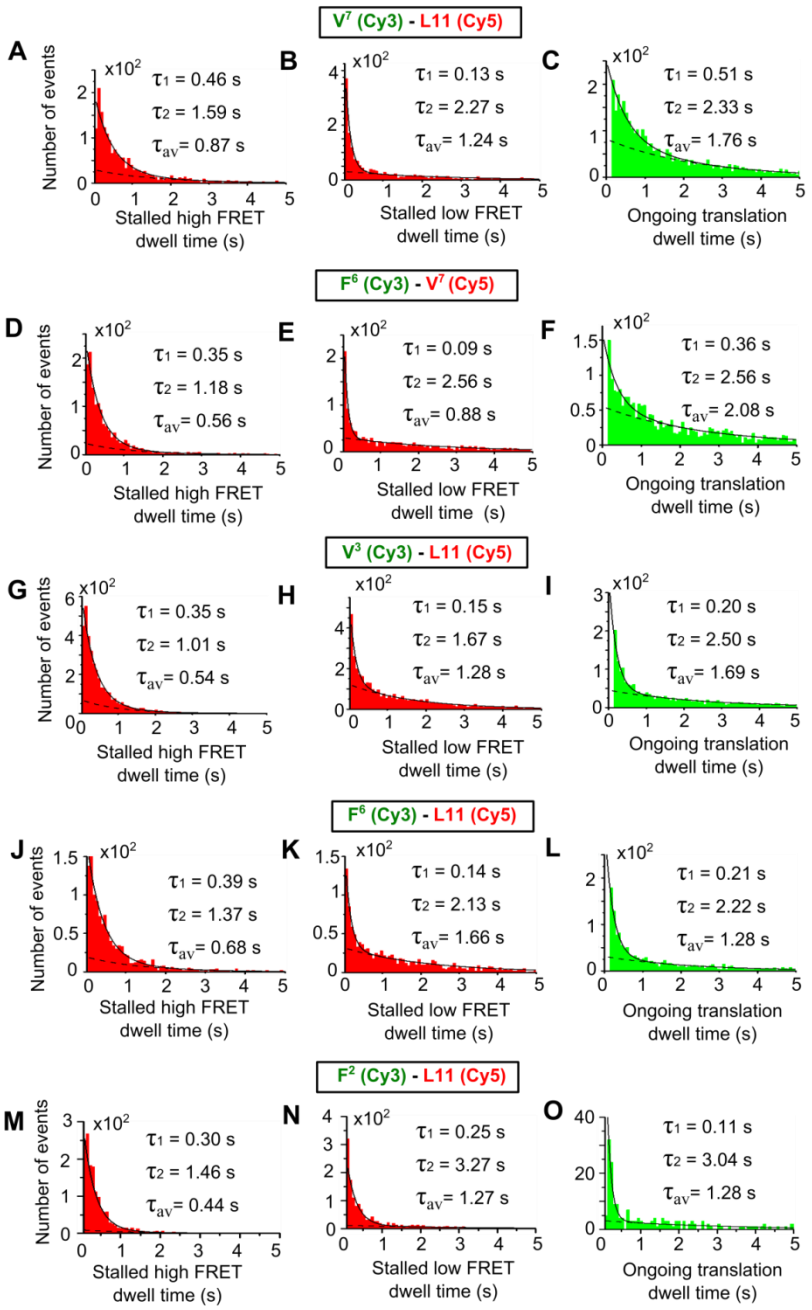

Figure 2.7. **Dwell times for the stalled classical and hybrid tRNA positions, and the ongoing intermediate state at 2 µM EF-G**. Double exponential fitting gave fast and slow phases for the lifetimes of each state, and weighted average durations, τ_{av}, according to Eq. 2.5.

Figure 2.8

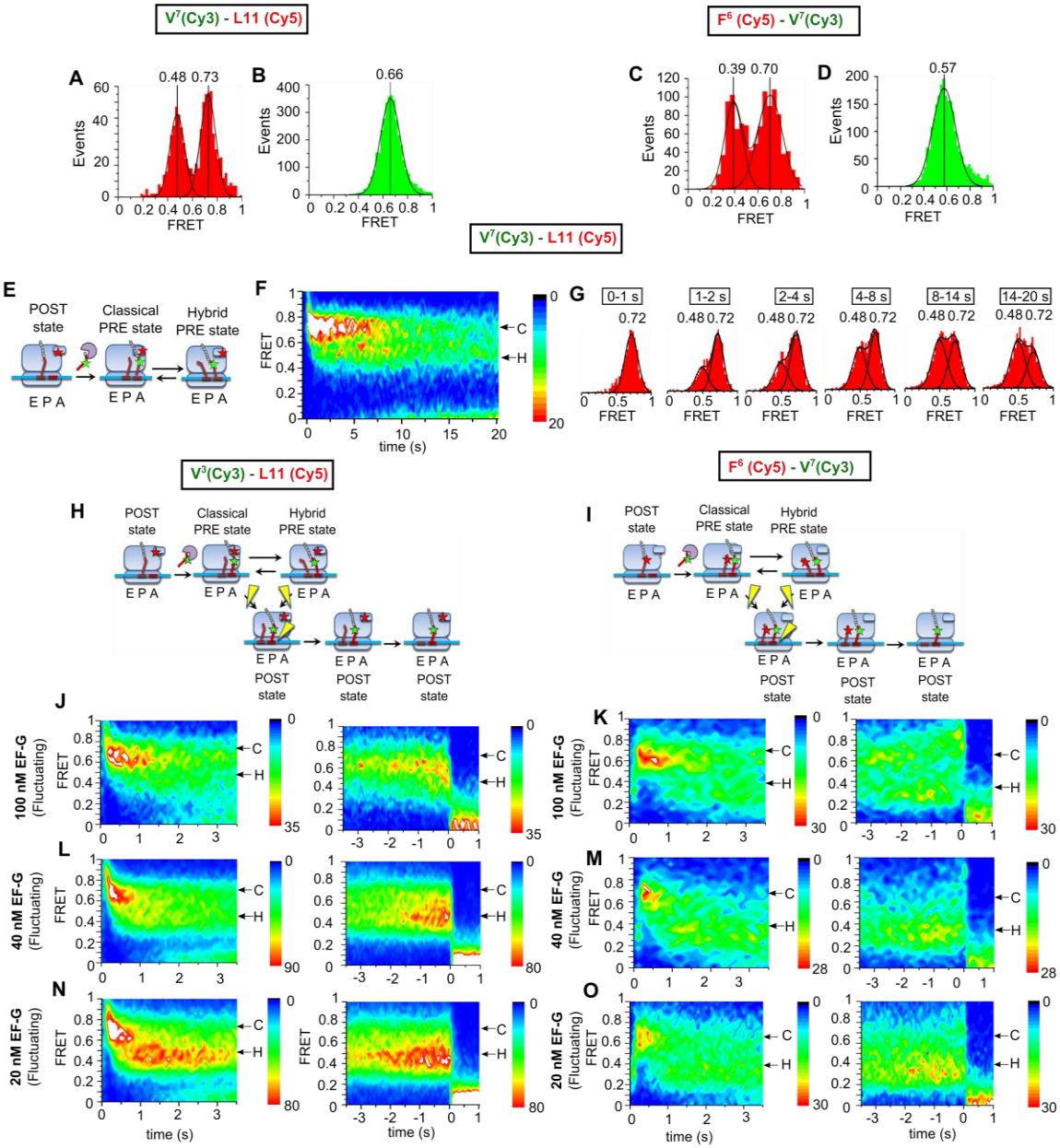
V7(Cy3) - L11 (Cy5)
F6 (Cy5) - V7(Cy3)
A
B
C
D
Events
FRET
0.48 0.73
0.66
0.39 0.70
0.57
V7(Cy3) - L11 (Cy5)
E
POST state
Classical PRE state
Hybrid PRE state
E P A
F
FRET
time (s)
C
H
G
0-1 s
1-2 s
2-4 s
4-8 s
8-14 s
14-20 s
0.72
0.48 0.72
V3(Cy3) - L11 (Cy5)
F6 (Cy5) - V7(Cy3)
H
I
POST state
J
K
L
M
N
O
100 nM EF-G (Fluctuating)
40 nM EF-G (Fluctuating)
20 nM EF-G (Fluctuating)
time (s)

Figure 2.8: For both V^7(Cy3)-L11(Cy5) and F^6(Cy3)-V^7(Cy5) experiments, the average FRET efficiencies of the high and low FRET states from each stalled trace formed two-peaked event distributions **(A,C)**, while the average FRET efficiencies of each ongoing trace form a single-peaked event distribution **(B, D)**. These distributions are more narrow than the temporal histograms presented in the main text, because frame-to-frame noise (due to photon counting, camera amplification and laser noise) are averaged out in these pre-averaged (event) histograms. The peaks of their distributions are the same as the temporal histograms, demonstrating that those positions are not biased by the frame-to-frame noise. **(E)** Formation of the PRE complex in the absence of EF-G was observed by injecting Val-$tRNA^{Val}$(Cy3) ternary complex by itself into flow chambers containing stalled L11-labeled ribosomes with peptidyl-Phe-$tRNA^{Phe}$ in their P-sites and vacant A-sites**.** The subsequent FRET recordings lasting from tRNA until photobleaching, and were used to form a pre-synchronized 2D contour plot **(F)** and histograms of cross-sections through the 2D contour plot at designated times **(G).** The tRNA-L11 FRET pair (**F**, G, n =192 molecules) initially exhibits high (classical) FRET efficiency before partitioning into a classical-hybrid equilibrium without adopting the intermediate state seen during ongoing translation at 2 μM EF-G. At lower EF-G concentrations (20 nM to 100 Nm) during ongoing translation (**H - O**), a minority of the traces fluctuated between classical and hybrid states before translocating, despite the majority adopting a non-fluctuating intermediate FRET efficiency. **(H, I)** Reaction schemes indicating that EF-G can bind to either the classical or hybrid state to catalyze translocation. Pre- and post-synchronized contour maps for tRNA-L11 **(J-N)** and tRNA-tRNA **(K-O)** FRET demonstrate that at reduced EF-G concentrations, the hybrid state is more prominent and becomes the primary state from which translocation occurs.

	FRET Efficiency, Ongoing	σ_F, Ongoing	FRET Efficiency, Stalled Classical tRNA Position	σ_F, Stalled Classical	FRET Efficiency, Stalled Hybrid tRNA Position	σ_F, Stalled Hybrid
V^7(Cy3) - L11(Cy5), (Fig. 1C,F)	0.65	0.12	0.73	0.08	0.49	0.11
F^6(Cy5) - V^7(Cy3), (Fig. 2C,F)	0.59	0.16	0.68	0.10	0.39	0.12
F^6(Cy3) - V^7(Cy5) (Fig S1C,F)	0.57	0.16	0.73	0.12	0.40	0.15
F^6(Cy3)-L11(Cy5), (Fig. S2C,F)	0.69	0.09	0.73	0.09	0.43	0.12
V^3(Cy3) - L11(Cy5), (Fig. S1J,M)	0.66	0.12	0.73	0.09	0.46	0.11
V^3(Cy5) - L11(Cy3) (Fig S1Q,T)	0.63	0.14	0.70	0.08	0.49	0.14
F^2(Cy3)-L11(Cy5), (Fig. S2L,O)	0.68	0.09	0.74	0.09	0.43	0.13

Table 2.2: FRET efficiency distribution peak centers and standard deviations.

[EF-G]	V^3(Cy3) - L11(Cy5)	F^6(Cy5) - V^7(Cy3)
2 μM	74 / 2057 = 3.6 %	11 / 1423 = 0.8 %
500 nM	33 / 934 = 3.5 %	31 / 346 = 9.0 %
100 nM	144 / 836 = 17.2 %	139 / 1045 = 13.3 %
40 nM	269 / 1229 = 21.9 %	150 / 524 = 28.6 %
20 nM	125 / 494 = 25.3 %	195 / 651 = 30.0%

Table 2.3: Percentages of traces that fluctuate before translocating at various EF-G concentrations.

FRET pair	τ_{fast}	Proportion fast	τ_{slow}	Proportion slow	τ_{av}
V^7(Cy3) - L11(Cy5)	0.46 s	0.63	1.59 s	0.37	0.87 s
F^6(Cy5) - V^7(Cy3)	0.35 s	0.74	1.18 s	0.26	0.56 s
F^6(Cy3)-L11(Cy5)	0.39 s	0.70	1.37 s	0.30	0.68 s
V^3(Cy3) - L11(Cy5)	0.35 s	0.75	1.01 s	0.25	0.54 s
F^2(Cy3)-L11(Cy5)	0.30 s	0.88	1.46 s	0.12	0.44 s

FRET pair	τ_{fast}	Proportion fast	τ_{slow}	Proportion slow	τ_{av}
V^7(Cy3) - L11(Cy5)	0.13 s	0.48	2.27 s	0.52	1.24 s
F^6(Cy5) - V^7(Cy3)	0.09 s	0.26	2.56 s	0.74	0.88 s
F^6(Cy3)-L11(Cy5)	0.14 s	0.24	2.13 s	0.76	1.66 s
V^3(Cy3) - L11(Cy5)	0.15 s	0.30	1.67 s	0.70	1.28 s
F^2(Cy3)-L11(Cy5)	0.25 s	0.69	3.27 s	0.31	1.27 s

FRET pair	τ_{fast}	Proportion fast	τ_{slow}	Proportion slow	$\tau_{weighted}$
V^7(Cy3) - L11(Cy5)	0.51 s	0.31	2.33 s	0.69	1.76 s
F^6(Cy5) - V^7(Cy3)	0.36 s	0.35	2.56 s	0.64	2.08 s
F^6(Cy3)-L11(Cy5)	0.21 s	0.47	2.22 s	0.53	1.28 s
V^3(Cy3) - L11(Cy5)	0.20 s	0.21	2.50 s	0.79	1.69 s
F^2(Cy3)-L11(Cy5)	0.11 s	0.61	3.04 s	0.39	1.28 s

Table 2.4: Dwell times for stalled and ongoing experiments calculated by fitting double exponential functions to the unbinned dwell time data using maximum likelihood estimation as. τ_{av} is calculated using Eq. 2.5 in Supplemental Methods.

FRET pair	Fraction of ongoing traces observed fluctuating	Fraction of ongoing traces predicted to fluctuate if intermediate state were classical
V^{7}(Cy3) - L11(Cy5)	184 / 3664 = 0.050	0.65
F^{6}(Cy5) - V^{7}(Cy3)	100 / 2359 = 0.042	0.75
F^{6}(Cy3) - V^{7}(Cy5)	10 / 200 = 0.050	0.49
F^{6}(Cy3)-L11(Cy5)	11 / 1423 = 0.008	0.55
V^{3}(Cy3) - L11(Cy5)	74 / 2157 = 0.034	0.65
V^{3}(Cy5) - L11(Cy3)	18 / 319 = 0.056	0.58
F^{2}(Cy3)-L11(Cy5)	5 / 204 = 0.025	0.50

Table 2.5: Fraction of ongoing ribosome population expected to fluctuate based on stalled fluctuation dwell times.

FRET pair	$\frac{1}{k_{high\rightarrow low} + k_{low\rightarrow high}}$ from weighted dwell times of fluctuating stalled ribosomes	τ_{decay} from cross-correlation as a function lag for fluctuating stalled ribosomes
V^7(Cy3) - L11(Cy5)	0.51 s	0.52 s
F^6(Cy5) - V^7(Cy3)	0.34 s	0.31 s

Table 2.6: τ_{decay} from exponential fitting of cross-correlation as a function of lag (Eq. 2.7) for fluctuating stalled ribosomes (Fig 2.1J, 2.2J), compared to the expected rate constant calculated from the sum of the classical and hybrid FRET tRNA position dwell times.

As the mentioned in the main text, stalled fluctuating traces had anti-correlated donor and acceptor intensities, while ongoing traces did not (Fig 1J, 2J), thus ruling out fluctuations slower than 30 s^{-1}. This analysis can be extended by calculating the cross-correlation as a function of lag in the time domain. Also called a "sliding inner product" or cross-correlogram, the two signals are shifted in time with respect to each other before calculating the cross-correlation for different amounts of shift (Eq. 2.7), a technique commonly used in signal processing to search a long signal for a shorter or encoded feature, or determine the time delay between signals (Lathi, 2004). In this context, a shift of integer numbers of camera frames between donor and acceptor intensities reduces positive or negative correlations towards zero, since stochastic changes of the two channels' intensities become out of sync as they are shifted relative to each other. In fact, the negative cross-correlation of the stalled traces decayed to zero at a rate consistent with the sum its kinetic constants ($k_{classic\rightarrow hybrid} + k_{hybrid\rightarrow classic}$, Table 6) as expected (Guttfreund, 1995). In contrast, the positive cross-correlation of the ongoing translation intensities decayed to zero within one frame of lag (Fig 2.1J, 2.2J), consistent with common-mode noise (eg. laser intensity fluctuations), rather than rapid distance fluctuations.

2.4 Discussion

Previous studies have demonstrated that stalled PRE complexes undergo classical-hybrid fluctuations ((Chen et al., 2011; Cornish et al., 2009b; Fei et al., 2008; Kim et al., 2007; Munro et al., 2010b; Wang et al., 2011) on a time scale of 0.5 – 2 s^{-1}, that added EF-G could catalyze translocation by binding to either PRE complex (Adio et al., 2015; Chen et al., 2011, 2013) and that added EF-G terminated such fluctuations (Adio et al., 2015; Chen et al., 2011, 2013). Here we report that during ongoing translation, when ternary complexes and 2 μM EF-G are present together in the reaction mixture, PRE complex tRNA positions do not fluctuate between the classical and hybrid states but rather adopt a structure with a single dominant FRET efficiency, whether measured by tRNA-L11 or tRNA-tRNA interaction.

These results, which are consistent with earlier, less definitive results (Rosenblum et al., 2013) about tRNA fluctuations during the brief occupancy of the PRE complex during the active elongation cycle. The results demonstrate that at high EF-G concentration, it drives newly formed PRE complexes directly into a non-fluctuating intermediate FRET state, bypassing the classical ↔ hybrid fluctuations that have been previously observed for stalled PRE complexes. Given our frame rate of 30 s^{-1}, if any fluctuations did occur, they would require fluctuation rates during ongoing translation at least 15- to 30-fold faster than the canonical classical-hybrid fluctuations observed in Figs. 2.1B, 2.2B, 2.5B, 2.5I, 2.5P, 2.6B, 2.6K and reported in the references cited above. That is less likely than EF-G suppressing fluctuations (as occurs when EF-G is added to stalled PRE complexes) (Chen et al., 2011, 2012). However, if it did occur, that would

define a new PRE state with vastly different dynamics than that observed in stalled ribosomes.

Chen et al. (Chen et al., 2013) have reported smFRET fluctuations that monitored subunit rotations during ongoing translation. However, these fluctuations were extremely, slow with dwell times greater than 10s and were observed at 200-500 nM EF-G, a range in which we also observed that fluctuations are not fully supressed (Figs. 2.1K, 2.2K, Table 2.3), presumably resulting from more time elapsing between ternary complex arrival at the A-site and EF-G binding. Moreover, as noted above, subunit rotations are temporally distinct processes (Belardinelli et al., 2016; Sharma et al., 2016), from the tRNA movements under focus in this study.

The non-fluctuating FRET efficiencies, while intermediate between those found in the classical and hybrid PRE complexes, are generally closer to the classical than to the hybrid tRNA position (Table 2.1) and suggest the formation of a translocation intermediate not previously observed in smFRET or structural studies. Adio et al. (Adio et al., 2015) have identified an intermediate FRET state on addition of EF-G to pre-equilibrated PRE complexes, but this intermediate was only detected when translocation was slowed down or prevented by using functionally impaired EF-G mutants, replacing GTP with the non-hydrolyzable GTP analog, GTP-γS, or by adding the antibiotic fusidic acid. Moreover, this intermediate had a FRET efficiency value lower than either the hybrid or classic PRE complexes and so it does not correspond to the intermediate we observed. Several high resolution structures (Ramrath et al., 2013; Zhou et al., 2014) show that tRNAs in EF-G-bound ribosomal complexes, stabilized by antibiotics and/or non-hydrolysable GTP analogs prior to formation of the POST complex, in some cases

adopt states in which various regions of the tRNAs are associated with different sites in the two ribosome subunits. These so-called chimeric states, while corresponding to neither classical nor hybrid states, have tRNA-tRNA and tRNA-L11 distances, 45-50 Å and 70-80 Å, respectively (Ramrath et al., 2013; Zhou et al., 2014), which are very similar to those of the hybrid state, also different from what we observe during ongoing translation.

How does relatively high EF-G concentration drive formation of the non-fluctuating intermediate state as the PRE complex is formed? A possible explanation is that ternary complex binds to a ribosome containing EF-G. EF-G interacts directly with L11 and with the carboxy-terminal domain of L12 when trapped in the POST-translocation complex (Gao et al., 2009). Binding of EF-G or EF-Tu to ribosomal elements between translation steps is known to be important for GTPase activation, and could also serve to channel factors into their binding sites and facilitate rapid translation (Diaconu et al., 2015; Kothe et al., 2004). Another example of such channelling is the multiple profilin binding sites on the actin-binding protein, formin, which channel actin subunits into the filament tip, thereby accelerating polymerization (Goode and Eck, 2007). In translation, when a high concentration of EF-G is present simultaneously with the tRNA ternary complexes, as is true *in vivo* ([EF-G] = 10 – 20 μM, Munishkin and Wool, 1997), EF-G might associate with one of the multiple copies of L7/L12 prior to ternary complex arrival at L11, and allosterically modulate the conformation that the PRE complex will occupy once the next tRNA arrives.

In summary, our current observations, taken with our previous results others, suggest that translocation proceeds via either the ongoing or stalled pathway, with the partitioning

between the two pathways depending on the concentration of EF-G (Fig 2.4). Both pathways begin with initial ternary complex binding, with the aminoacyl-tRNA rapidly traversing the A/T state, hydrolyzing GTP and EF-Tu·GDP dissociation (Geggier et al., 2010). At high [EF-G], which is physiologically relevant, the ongoing pathway dominates, and the initially formed PRE complex is rapidly driven into a single, non-fluctuating intermediate state (Fig 2.4, top) before the tRNAs are translocated into the P- and E-sites. In contrast, in the stalled pathway, which is dominant only when EF-G is either absent during PRE complex formation or present at very low (≤100 nM) concentration (Table 2.3), the PRE complex enters into the well-characterized equilibrium between the classical and hybrid tRNA positions (Fig 2.4, bottom), from which subsequent binding of EF-G·GTP catalyzes translocation (Adio et al., 2015; Chen et al., 2011).

2.5 Experimental procedures

2.5.1 Summary of procedures

In brief, 70S initiation complexes were formed using a 5′-biotinylated mRNA (Dharmacon RNAi Tech, sequences in Supplemental Information), and fluorescent-labelled ternary complexes were pre-formed from EF-Tu, GTP, and charged tRNAs labelled with either Cy3 or Cy5 at dihydrouridine positions in the D loop (Kaur et al., 2011) For stalled experiments, the unlabelled ternary complexes (TCs), as well as the Cy5-labeled Phe ternary complex in the case of tRNA-tRNA FRET experiments, 2 μM EF-G, and 3 mM GTP were added to the initiation complexes and incubated for 5

minutes, followed by immobilization of the resulting POST complexes on a streptavidin/biotin-PEG coated glass surface (Chen et al., 2011; Roy et al., 2008). Unbound reaction components including EF-G were then washed out of the channel. Cy3-labeled ternary complex was then added in the absence of EF-G to form a new PRE complex, with image stacks recorded either during the addition or after washing away unbound Cy3-labeled ternary complexes. For ongoing experiments, the initiation complexes alone were immobilized on the slide, and all cognate TCs (labeled and unlabeled) were added in the presence of 2 μM EF-G and 3 mM GTP while recording.

Cy3 and Cy5 fluorescence intensities (allowing calculation of FRET between Cy3 and Cy5) were collected using the alternating laser excitation (ALEX) mode to switch between 532 nm and a 640 nm lasers on an objective-type TIRF microscope (Chen et al., 2011). Except as otherwise indicated, stalled experiments were recorded with ALEX at 35 ms integration time per frame resulting in a net time resolution of 70 ms, while ongoing translation experiments were recorded solely with 532 nm excitation, giving 35 ms time resolution. All translation experiments were carried out with buffer TAM_{15} (15 mM $MgAc_2$, 50 mM Tris-HCl pH 7.5, 30 mM NH_4Cl, 70 mM KCl, and 1 mM DTT) at 23 °C. More extensive details of materials preparation, the experimental setup, FRET measurement, and data analysis are described below.

2.5.2 mRNA sequences

5'-biotin-labeled mRNA (Dharmacon, Inc.) had the following sequences:

FVR at beginning of message: AUU UAA AAG UUA AUA AGG AUA CAU ACU *AUG UUC GUG CGU UAU UAU UAU UAU UAU UAU UAU UAU UAU.* The

italicized sequence codes for MFVRYYYYYYYYY.

FVR several codons into message: AUU UAA AAG UUA AUA AGG AUA CAU ACU *AUG UAU UAU UAU UAU UUC GUG CGU UAU UAU UAU UAU UAU.*The italicized sequence codes for MYYYYFVRYYYYY.

The underlined sequence is a strong Shine-Dalgarno region.

2.5.3 Initiation complex formation

Double variant C38S/S87C-L11 was constructed via site-directed mutagenesis of the N-terminal His-tagged L11 used previously (Qin et al., 2009; Seo et al., 2006; Wang et al., 2007), purified and labeled with Cy5-maleimide (GE) as previously described (Chen et al., 2011). To reconstitute L11 ribosomes, a 2-fold molar excess of C38S/S87C-L11Cy5 was incubated with 2 μM AM77 70S ribosomes lacking L11 in TAM_{15} buffer (50 mM Tris- HCl [pH 7.5], 15 mM $Mg(OAc)_2$,30 mM NH_4Cl, 70 mM KCl, 1 mM DTT) (Chen et al., 2011)) with 5 mM additional $Mg(OAc)_2$ for 15 min at 37 °C. The reconstituted ribosomes then underwent ultracentrifugation as previously described (Qin et al., 2009; Wang et al., 2007). 70S initiation complex was formed by incubating 1 μM 70S ribosomes, 4 μM biotin-mRNA (sequences listed above), 1.5 μM each of IF1, IF2, IF3 and fMet-$tRNA^{fMet}$, and 1 mM GTP in TAM_{15} buffer for 25 min at 37 °C.

2.5.4 tRNAs and ternary complex formation

Labeled tRNAs were prepared using the reduction and charging protocols previously described (Chen et al., 2011; Pan et al., 2009) starting with E. coli $tRNA^{fMet}$, $tRNA^{Tyr}$,

$tRNA^{Val}$, and yeast $tRNA^{Phe}$ purchased from Chemical Block (Moscow). $tRNA^{Phe}$ and $tRNA^{Val}$ were labeled with Cy3, and $tRNA^{Val}$ with Cy5, via a dihydroU-hydrazine linkage as described (Kaur et al., 2011). Ternary complex was formed by incubating 4 μM EF-Tu, 2 μM dye-labeled and charged tRNA, 3 mM GTP, 1.3 mM phosphoenolpyruvate, and 5 μg/mL pyruvate kinase in TAM_{15} buffer for 15 min at 37 °C.

2.5.5 Flow chamber construction

The sample flow chambers (8 μL) were formed on slides with holes drilled using a 1.25 mm diamond-tipped drill bit. Double-sided tape laid between the drilled holes served as spacers and separated the flow chambers. Polyethylene tubing with 0.97 mm outer diameter (Warner Instruments) was inserted into each hole and sealed with 5 min epoxy. The coverslips were then sealed in place via the double-sided tape and epoxy at their edges. These flow chambers allow fast injection of reaction mixtures into the channels while recording image series.

2.5.6 smFRET: General conditions

smFRET studies were carried out at 23 °C in TAM_{15} buffer . An enzymatic deoxygenation system of 0.3% (w/v) glucose, 300 μg/ml glucose oxidase (Sigma-Aldrich), 120 μg/ml catalase (Roche), and 1.5 mM 6-hydroxy-2,5,7,8-tetramethyl-chromane-2-carboxylic acid (Trolox, Sigma-Aldrich) was added to the final single-molecule imaging solutions to reduce fluorophore photobleaching and blinking (Chen et al., 2011). Microscope slides and coverslips were coated with polyethylene glycol (m-

PEG-SVA-2000; Laysan Bio) to prevent nonspecific binding, as well as 1-5% biotinylated-PEG (biotin-PEG-SC-2000; Laysan Bio, (Roy et al., 2008)), and flow chambers were constructed as described above. 0.5 mg/ml Streptavidin was applied to the surface and washed away with TAM_{15} buffer before 1-5 nM initiation complex was added and immobilized on the surface via biotin-mRNA. Unbound initiation complex was washed away with TAM_{15} buffer. Image stacks were recorded on a custom-built objective-type total internal reflection fluorescence (TIRF) microscope based on a commercial inverted microscope (Eclipse Ti-E, Nikon) and equipped with the ability to perform alternating-laser excitation (ALEX) between 532 nm and 640 nm beams (Chen et al., 2011).

2.5.7 Stalled ribosome smFRET

After immobilizing the initiation complex on the slides, solutions with 10 nM unlabeled TC, 2 μM EF-G, and 3 mM GTP in TAM_{15} were injected to allow the ribosome to translate through all of the codons preceding the codon corresponding to the labeled tRNA. For Val-$tRNA^{Val}$(Cy3)-L11(Cy5) experiments, the codons preceding Val required unlabeled Tyr-$tRNA^{Tyr}$ and Phe-$tRNA^{Phe}$ TCs, whereas for Phe-$tRNA^{Phe}$(Cy3)-L11(Cy5) experiments, only Tyr-$tRNA^{Tyr}$ TC was required. For Phe-$tRNA^{Phe}$(Cy5)-Val-$tRNA^{Val}$(Cy3) experiments, the Phe-$tRNA^{Phe}$(Cy5) TC was injected along with the unlabeled Tyr-$tRNA^{Tyr}$ ternary complex; thus the P-site was occupied with Cy5-labeled $tRNA^{Phe}$ in the POST state.

The unbound ternary complex and EF-G were then washed out with TAM_{15} buffer, and the vacant A-sites of the ribosomes were filled by injecting 10 nM labeled cognate

TC, forming a stalled PRE state. Finally, unbound ternary complex was washed out by TAM_{15} buffer with imaging buffer, and image stacks were acquired at 35 ms per frame using ALEX illumination, resulting in a net 70 ms time resolution. For the experiments observing PRE complex formation in real time, the labeled cognate ternary complex was injected while recording with only 532 nm laser illumination.

2.5.8 Ongoing translation smFRET

After the initiation complex was immobilized on the slides via biotin-streptavidin linkage as described above, unbound initiation complex was washed out with TAM_{15} buffer. While recording image stacks, imaging buffer solution was injected containing 2 μM EF-G, 3 mM GTP, 10 nM Tyr-$tRNA^{Tyr}$ ternary complex, and 10 nM each of Phe-$tRNA^{Phe}$ and Val-$tRNA^{Val}$ TC (labeled or unlabeled depending on the experiment). Ongoing translation experiments were recorded with 532 nm excitation at 35 ms time resolution.

2.5.9 Calculation of FRET efficiency

FRET efficiency was calculated according to (Ha et al., 1999):

$$E = \left(1 + \frac{I_D}{I_A - \chi I_D}\gamma\right)^{-1} = \frac{(I_A - \chi I_D)}{(I_A - \chi I_D) + \gamma I_D} \qquad \text{(Eq 2.1)}$$

where I_D and I_A are the raw fluorescence intensities of the donor and acceptor, χ is the cross-talk of the donor emission into the acceptor recording channel, and γ accounts for the ratios of quantum yield and detection efficiency between the donor and the acceptor. Widths of the apparent FRET efficiency distributions are given as s.d. values in Table S4.

Based on bootstrapping with 1000 iterations, the 95% confidence intervals for the peaks of the FRET efficiency distributions are all <0.005.

2.5.10 Compensating FRET efficiencies for 532 nm excitation of Cy5

The excitation spectrum for Cy5 includes a small component at 532 nm, leading to a very low amount of direct excitation of Cy5 by the 532 nm laser. For ongoing translation experiments with Cy3-labeled tRNAs arriving at ribosomes already containing a Cy5-labeled L11 subunit or Cy5-labeled tRNA in the P-site, that excitation of Cy5 at 532 nm was taken into account by zeroing the very low sensitized acceptor intensity immediately before the event begins. Subsequently, the FRET efficiency during ongoing translation can be directly calculated according to Equation S1. However, for the stalled traces in which the PRE complex was formed before the recording began, zeroing the acceptor intensity to eliminate that component was not possible.

To quantitatively compare the stalled traces to ongoing traces, a correction factor φ representing this cross-excitation was calculated using the stalled traces in which Cy3 bleached before Cy5:

$$\varphi = \frac{I_{A,after\ event}}{\left(I_{A,during\ event} - \chi I_{D,during\ event}\right) + \gamma I_{D,during\ event}} \qquad \text{(Eq. 2.2)}$$

Values of φ formed distributions that were fit with single Gaussian components, and the corresponding peak center values were used to calculate FRET efficiency as follows:

$$E = \frac{I_A - \chi I_D - \varphi(I_A - \chi I_D + \gamma I_D)}{I_A - \chi I_D - \varphi(I_A - \chi I_D + \gamma I_D) + \gamma I_D} \qquad \text{(E1. 2.3)}$$

This cross-excitation correction reduced the reported peak FRET efficiencies of the stalled classical and hybrid tRNA positions by approximately 0.02.

2.5.11 Photobleaching

The dwell times for the PRE state during ongoing translation (Fig. 2.7) were much shorter than the bleaching times of the fluorophores (8.6-14 s), thus a Val-tRNA^{Val}(Cy3) – L11(Cy5) experiment with ALEX showed that 83% of the traces translocated before photo-bleaching. This result is consistent with the 85-88% calculated for the entire population of ongoing FRET events; if the analysis is restricted to the most biologically significant fast phase subpopulation, that percentage is even higher (94-98% translated before photobleaching). Since photobleaching constitutes a minority of our ongoing population, we chose not use alternating laser excitation to detect photobleaching in ongoing translation experiments; ALEX worsens the effective time resolution 2-fold, a disadvantage in efforts to detect fast fluctuations or transient states.

2.5.12 Hidden Markov analysis of smFRET traces

Image stacks were converted to intensity recordings using an ImageJ plugin written in-house (Chen et al., 2011). FRET traces were analyzed by a Hidden Markov Model-based software (HaMMy)(McKinney et al., 2006); for the stalled traces no more than two FRET states were identified by the program in any of the individual traces, and recordings with two FRET states were termed fluctuating traces. Ongoing traces were analyzed by the same program, which identified multiple states in a very small proportion (1% – 4%) of

recordings at 2 μM EF-G (Table S4), but did find more fluctuating examples at lower EF-G concentrations (Table S2).

2.5.13 Selection of stalled ribosome smFRET traces Markov analysis of smFRET traces

To determine the high and low FRET values associated with the classical and hybrid tRNA positions of stalled ribosomes, only ribosomes fluctuating between two FRET states (as identified by HaMMy) were used. That population is enriched for higher translational activity; approximately 80% of the ribosomes identified as fluctuating are capable of translocating after the injection of EF-G, whereas less than 25% of ribosomes that do not fluctuate while stalled complete translocation (Chen et al., 2011).

2.5.14 Dwell time fitting and comparison

Dwell times for each of the states were poorly fit by single exponential decays, as well as double exponential decays that failed to take into account the digitization caused by only recording dwell times as finite numbers of camera frames. This problem is especially pronounced when one of the two time components is of similar magnitude to the frame rate at which the data is recorded. Efforts to address this technical challenge gave rise to an entirely new computational methods project, which developed a method of convolving the probability with the camera instrument response function to account for that finite camera framing (Appendix A).

The equation used for the fitting takes the form:

$$\frac{1}{\Delta t}\frac{C\tau_1\left(1-e^{-\frac{\Delta t}{\tau_1}}\right)^2 e^{-\frac{\Delta t}{\tau_1}(f-1)} + (1-C)\tau_2\left(1-e^{-\frac{\Delta t}{\tau_2}}\right)^2 e^{-\frac{\Delta t}{\tau_2}(f-1)}}{C\tau_1\left(1-e^{-\frac{\Delta t}{\tau_1}}\right)e^{-\frac{\Delta t}{\tau_1}(f_{min}-1)} + (1-C)\tau_2\left(1-e^{-\frac{\Delta t}{\tau_2}}\right)e^{-\frac{\Delta t}{\tau_2}(f_{min}-1)}} \quad \text{(Eq. 2.4)}$$

which is the Eq A.7 derived in the course of Appendix A. In this equation, τ_1 and τ_2 are the dwell times that we seek to fit, along with the coefficients C and $(1-C)$. Δt represents the frame rate at which the data was recorded, while f_{min} is the minimum number of frames required for an event to meet the selection criteria of a true event, and f is the actual recorded duration of a particular event.

This equation was fit to unbinned dwell time data by maximum likelihood estimation (Bevington and Robinson, 2002; Woody et al., 2016), a process that can be summarized as follows: for a given set of values for parameters τ_1, τ_2, C, a log-likelihood score is calculated based on the individual probabilities (calculated using Eq 2.4 for every event, each with their own dwell time f) that an event of duration f would be measured according to that parameter set τ_1, τ_2, C. The values of those parameters τ_1, τ_2 and C are then varied to explore the parameter space and optimize that score.

For the dynamic case, that implantation used $f_{min} = 4$, but for the stalled case, $f_{min} = 1$ (due to the trace selection criteria). Thus, a further normalization correction was required for the stalled experiments, as $f_{min} = 1$ presents a special case detailed in Appendix A.4.6.

The resulting fitting parameters were combined to estimate the average dwell time

according to:

$$\tau_{av} = C\ \tau_{fast} + (1 - C)\tau_{slow} \qquad \text{(Eq. 2.5)}$$

To separately analyze the FRET traces belonging to the faster component, a time threshold was determined such that that the proportion of the double exponential distribution with dwell times below the threshold matches the fraction (*C*) that the fast phase contributes to the whole distribution.

To estimate the numbers of ongoing traces that would have switched state if the ongoing FRET values were canonical classical or hybrid tRNA positions, the transition rates of these processes were compared with the observed PRE dwell time. For two competing exponential processes (fluctuation from the initial state and translocation), we seek the probability that a trace will fluctuate before translocation. Taking the dwell times for both translocation and fluctuation as double exponential decays, the probability of a fluctuation before translocation is given by:

$$P[t_f < t_d] = \int_{t_d=0}^{\infty} \int_{t_f=0}^{t_d} \left[\frac{C_f}{\tau_{f1}} e^{\frac{-t_f}{\tau_{f1}}} + \frac{(1 - C_f)}{\tau_{f2}} e^{\frac{-t_f}{\tau_{f2}}}\right]\left[\frac{C_d}{\tau_{d1}} e^{\frac{-t_d}{\tau_{d1}}} + \frac{(1 - C_d)}{\tau_{d2}} e^{\frac{-t_d}{\tau_{d2}}}\right] dt_f dt_d \qquad \text{(Eq. 2.6)}$$

Where t_f is the time until the stalled ribosome fluctuates, t_d is the time until the ongoing PRE state translocates, τ_{f1} and τ_{f2} are the fast and slow phase time constants for the classical state of fluctuating stalled ribosomes, C_f and $(1 - C_f)$ are their respective contributions, τ_{d1} and τ_{d2} are the fast and slow phase time constants for the PRE state

occupancy during ongoing translation, and C_d and $(1 - C_d)$ are their respective contributions. Values for this probability are given in Table S4, indicating that many more ongoing ribosomes would have exhibited fluctuations than were observed if the ongoing FRET state is one of the canonical classical or hybrid tRNA positions with normal transition rates.

2.5.15 Donor-Acceptor cross-correlation

The cross-correlation, C_k, between the donor (I_d) and acceptor (I_a) intensity traces of length n with a lag of k frames was calculated by concatenating the donor vector with a second copy of itself and using the following equation (Weisstein, 2002), in which $\overline{I_d}$ and $\overline{I_a}$ represent the average acceptor and donor intensities of each trace, while σ_d and σ_a represent the standard deviations of those intensities throughout that trace.

$$C_k = \frac{\sum_{i=1}^{n}\left[\left(I_{a_{i+k}} - \overline{I_a}\right)\left(I_{d_i} - \overline{I_d}\right)\right]}{n\sigma_a\sigma_d} \qquad (Eq.\,2.7)$$

3. Nanosphere lithography of zero mode wave guides for single molecule fluorescence microscopy

3.1 Abstract

In single molecule fluorescence studies, background fluorescence from labeled substrates often requires them to be used at concentrations several orders of magnitude less than physiologic. One approach to address this challenge is the use of nanofabricated zero-mode waveguides (ZMWs), arrays of nanoscale holes in a thin metal film that physically and optically confine the observation volume and allow higher concentrations of labeled substrates to be used. However, the need for expensive and specialized nanofabrication equipment has precluded their widespread adoption by the biochemical community. In contrast, nanosphere lithography allows the fabrication of thousands of ZMWs in parallel, using little sophisticated equipment. A suspension of polystyrene microspheres dropped onto a glass slide self-assemble into a hexagonal array, forming a natural lithographic mask for the deposition of metallic posts in the interstices between beads. The cross-sectional size of those interstices (and thus subsequent posts) can be finely tuned in a range of 150-300 nm by fusing the beads for different amounts of time at the polystyrene glass transition temperature. After dissolving the beads in methylene chloride, a gold cladding is deposited around the posts and the posts are dissolved, leaving behind an array of 150-300 nm wide, 140 nm deep ZMWs. By using colloidal self-assembly, a laboratory with little specialized equipment can produce sub-wavelength ZMWs for single molecule fluorescence experiments at a low cost that will enable wide-scale adoption.

3.2 Introduction

Single molecule fluorescence techniques are valuable tools in biophysics; by avoiding the averaging inherent in bulk measurements, they can distinguish subpopulations of molecules, directly observe the trajectory and timing of reaction steps without needing to synchronize the whole population, and can enable study of rare events and conformational fluctuations. These techniques include super-resolution microscopy to track single molecule motion, fluorescence resonance energy transfer (FRET) probes to detect nanometer-scale distance changes (measured using either TIRF or confocal microscopy), and polarized total internal reflectance (polTIRF) microscopy that measures angular changes of a macromolecule. All single-molecule fluorescence techniques require careful optimization for signal-to-noise due to inherently limited signal.

Many single molecule fluorescence techniques utilize total internal fluorescence fluorescence (TIRF) microscopy, in which incident light reaches the glass-water interface at an angle greater than the critical angle, and is totally internally reflected. However, a near-field standing wave (the evanescent wave) is created at the interface that decays exponentially with distance from the boundary. This excites only the fluorescent molecules very close (<100 nm) to the glass-water interface, significantly reducing background fluorescence.

Despite the advantages offered by TIRF, background fluorescence from labeled substrates in solution remains a technical challenge in single molecule studies, requiring the substrates to be used at nano-/pico-molar concentrations. However, biological

processes usually occur at concentrations up to a million-fold greater (micro-/milli-molar). A potential solution is nanofabricated zero-mode waveguides (ZMWs),(Uemura et al., 2010) arrays of holes (30-300 nm diameter) in a thin, opaque metal layer (typically aluminum, chromium, or gold) on a glass substrate.(Moran-Mirabal and Craighead, 2008) These sub-wavelength apertures do not propagate optical modes in the visual spectrum, but illumination will create an evanescent wave (like in TIRF) that decays inside the well.(Bethe, 1944; Genet and Ebbesen, 2007)

The lateral dimensions of an idealized, perfectly conducting waveguide define a cutoff wavelength λ_c, above which light transmission is exponentially cut off. However, real metals have skin depths (due to electromagnetic field penetration into the walls of the waveguide), which results in a continuous shift from the propagating to the evanescent regimes with longer wavelengths.(Genet and Ebbesen, 2007)

For fluorescence microscopy, ZMWs are most useful when their size is sufficiently small that the lasers being used occupy the evanescent regime. By constraining the observation volume physically (in the x- and y-axes) and optically (in the z-axis), ZMWs give observation volumes on the order of tens of atto-liters, allowing use of micro-/milli-molar fluorescent substrates without prohibitive background fluorescence.(Moran-Mirabal and Craighead, 2008)

ZMWs have been produced by directly patterning the metal layer using ion beam milling,(Fore et al., 2007; Rigneault et al., 2005) or via electron beam lithography and subsequent dry-etching(Levene et al., 2003; Samiee et al., 2005) or metal lift-off.(Craighead, 2007; Leutenegger et al., 2006; Perentes and et al., 2005; Samiee et al., 2006) Although the presence of thousands of wells on each substrate allow a parallel

collection of data during an experiment, each well of the ZMW is fabricated in series; a slow and expensive process. Here, we describe a method of fabricating ZMWs through colloidal templating of polystyrene beads, using the self-assembly of an ordered structure to pattern arrays of nanoscale wells. Not only is this method faster and less expensive than ion beam milling or electron beam lithography, it requires very little specialized equipment and allows ZMWs to be widely accessible to any lab conducting single molecule fluorescence experiments.

3.3 Results and Discussion

3.3.1 Nanofabrication of ZMWs

ZMWs were fabricated using colloidal lithography according to the schematic in Figure 3.1. After thorough cleaning of glass coverslips (see Detailed Methods), suspensions of 1 μm polystyrene beads at a 12% v/v in 1:400 TritonX:EtOH were pipetted as 5 μL droplets onto the centers of the coverslips, which had been kept at 85% humidity. The bead suspensions spread into 2 cm circular puddles, whose evaporation drove the self-assembly of a 2D crystal. The resulting thin films of polystyrene beads (Fig 3.2A) were arranged in a hexagonal lattice, with thin voids between large domains of different lattice orientations (Fig 3.1H,I). A 2D crystal with the grain sizes obtained here (~10 μm across on average) uniformly covering 2 cm areas represents a significant technical advance, useful not only for the fabrication of ZMWs, but possibly also in developing materials for batteries and energy storage (Wang, 2006) and fabricating nanowires for semiconductor devices (Peng et al., 2007).

The top surfaces of the beads acts as a diffractive surface grating; the viewing angle determines the apparent spacing of the spheres in a range < 1000 nm (the diameter of the beads, and thus their actual spacing in the lattice). Thus, different wavelengths of reflected visible light undergo constructive or destructive interference based on the viewing angle, and the hexagonal lattices appeared to be different colors from different angles, a form of structural coloration similar to the iridescence of peacock feathers, oyster shells, and the wings of butterflies and beetles (Ball, 2012; Vukusic and Sambles, 2003). Prior to aluminum deposition, this structural coloration is most apparent when the beads are exposed to strong back-lighting (Fig3.1G).

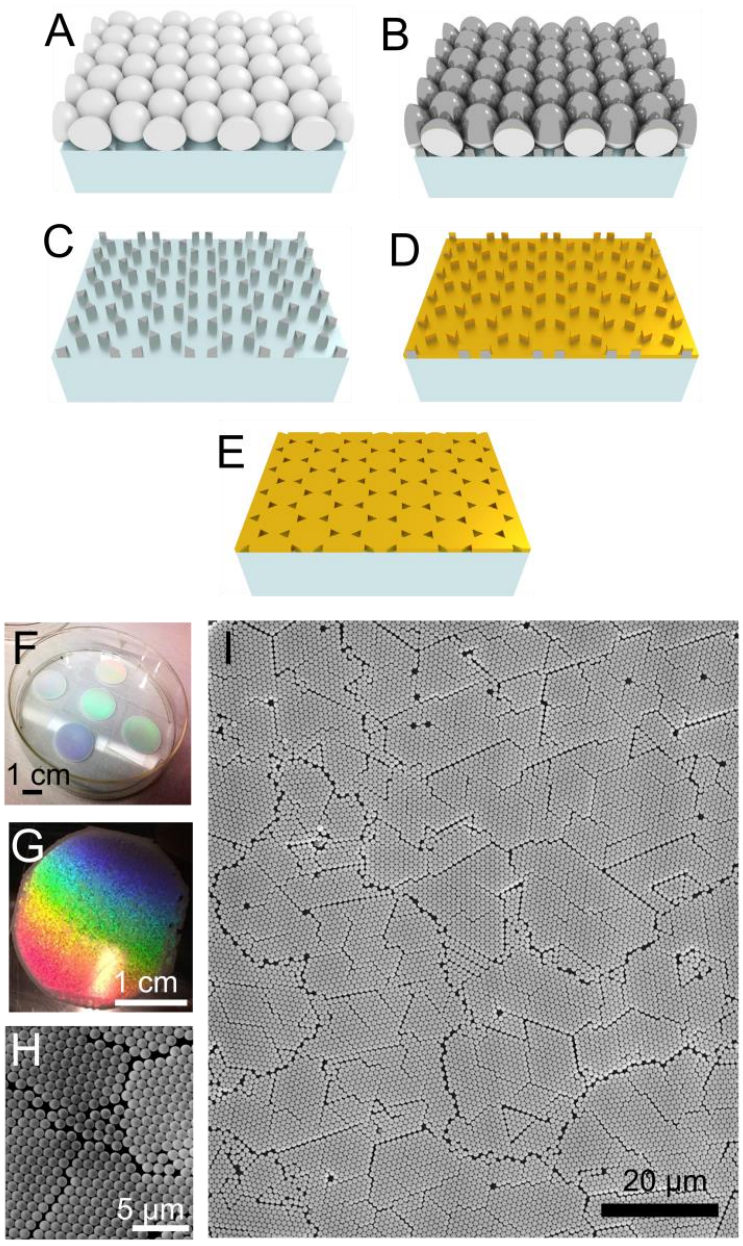

Figure 3.1. Schematic of ZMW fabrication via colloidal lithography. **(A)** 1 μm polystyrene beads deposited onto glass coverslip form close-packed hexagonal array. **(B)** Aluminum evaporated onto bead array. **(C)** Polystyrene beads dissolved, leaving aluminum posts that had formed in bead interstices. **(D)** Gold cladding evaporated over posts. **(E)** Aluminum posts etched away, leaving wells in gold. **(F,G)** Coverslips with monolayers of polystyrene beads deposited on surface. **(H,I)** SEM images of polystyrene beads in hexagonal lattice, with grain boundaries between domains of different lattice orientations.

Since the interstices between the beads will ultimately determine the cross-sectional size of the ZMW wells, one method to make the wells narrower and less triangular is to briefly heat the polystyrene beads to their glass transition temperature (approximately 107 °C) (Rieger), allowing the beads to fuse with one another at their contact points. Simply substituting the 1 μm beads with smaller beads would not solve this issue, as that would reduce the spacing between the wells and prevent them from being optically resolvable from one another. For a range of treatment times from zero to 30 seconds (at which the beads fuse together completely), there is a reproducible relationship between melting time and the Feret diameter (the greatest distance between the two parallel planes restricting the object perpendicular to that direction) of the pores measured using SEM (Fig 3.2). This procedure allows the pore size to be easily tailored for diameters between 350-100 nm, which is essential for constructing waveguides with cutoff wavelengths adequate for the lasers used in single molecule fluorescence In addition, a round profile of the wells is also important; in non-cylindrical waveguides, the transmission is polarization sensitive (Degiron et al., 2004).

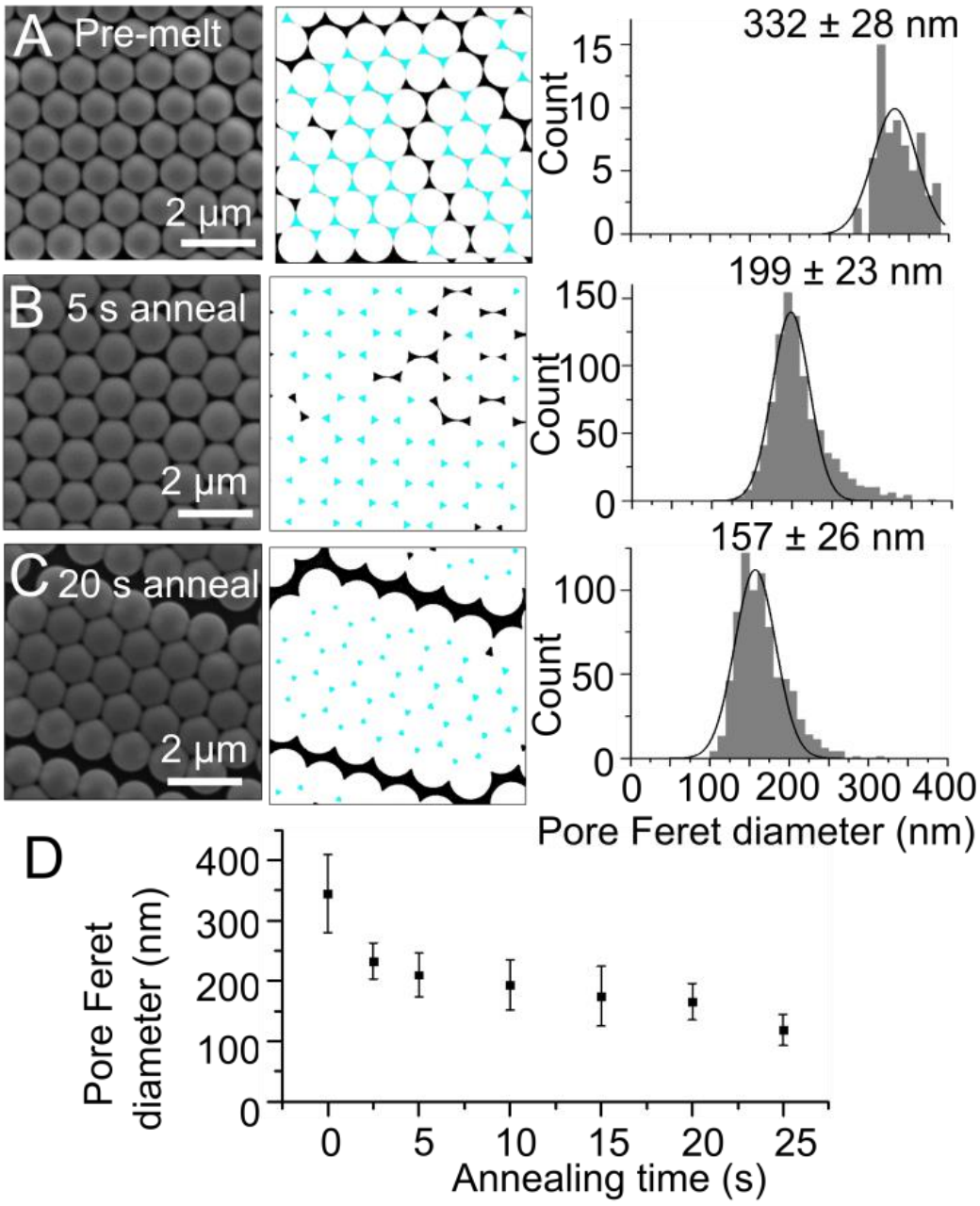

Figure 3.2. Annealing of beads to tune pore size. SEM images of beads that were not heated **(A),** or were heated at 107 °C for 5 s **(B)** or 20 s **(C),** with corresponding interstitial areas selected (cyan) and Feret diameter histograms for the measured areas. **(D)** Interstitial Feret diameter from SEM images as a function of melting time

After the hexagonal lattice of beads was formed and annealed, the colloidal films were used as lithographic masks during line-of-sight vapor thermal evaporation of aluminum. 3 nm of titanium was deposited first to serve as an adhesion layer between the aluminum and the glass, followed by a 300 nm film of aluminum that reached the glass surface only in the interstices between the beads (schematic, Fig 3.1B). The mirrored top surfaces of the beads also enhanced the structural coloration, giving a vibrant rainbow appearance (Fig 3.3A).

After 20 min plasma cleaning to disrupt the attachment of aluminum to the top of the polystyrene beads, Scotch tape was used to remove the aluminum from tops of those beads. The beads were then dissolved in methylene chloride to leave a hexagonal array of aluminum posts (schematic, Fig 3.1C, AFM, Fig 3.3B-C) with heights of 250-300 nm. Since the annealing of the beads reduced the Feret diameter of the interstices between the beads, it likewise reduced the profile of the posts deposited in those interstices. To measure the size of the wells, we used the maximum Feret diameter In samples that were not annealed, the posts were large (Feret diameter ~300) and triangular (Fig 3.3B), while the samples that were annealed had smaller (Feret diameter ~130 nm) and rounder posts (Fig 3.3C,D). The distribution of post Feret diameters had a dominant narrow peak, but a small population with diameters between 200 nm and 250 nm, likely due to incomplete fusing of the beads during annealing.

140 nm of gold cladding was then deposited around the aluminum posts. To selectively remove the posts and leave ZMW arrays in the gold cladding, the coverslips were sonicated in aluminum etchant for 2 hours. The final ZMWs formed a 1.5-2 cm circular array in the middle of the glass coverslips (Fig. 3.3E) with the surrounding areas

that were not coated with beads (and thus coated with aluminum) remaining bare glass. AFM confirmed that most of the posts were broken and dissolved, although <5% remained intact (Fig 3.3F), and demonstrated that the wells were approximately 140 nm deep (Fig. 3.3G), as expected based on the thickness of cladding deposited. Finally, the Feret diameters of the wells had a biomodal population that could be fit with two Gaussians (Fig. 3.3H): a main population with an average 133 nm diameter, as well as a minor population with 230 nm diameter (similar to the minor population of posts seen earlier). Both well populations had distributions that were wider than at the post stage, since each successive processing step introduced further variance. In summary, the main population of wells were approximately 140 nm wide and 140 nm deep, similar to the dimensions of gold ZMWs made by others.(Kinz-Thompson et al., 2013)

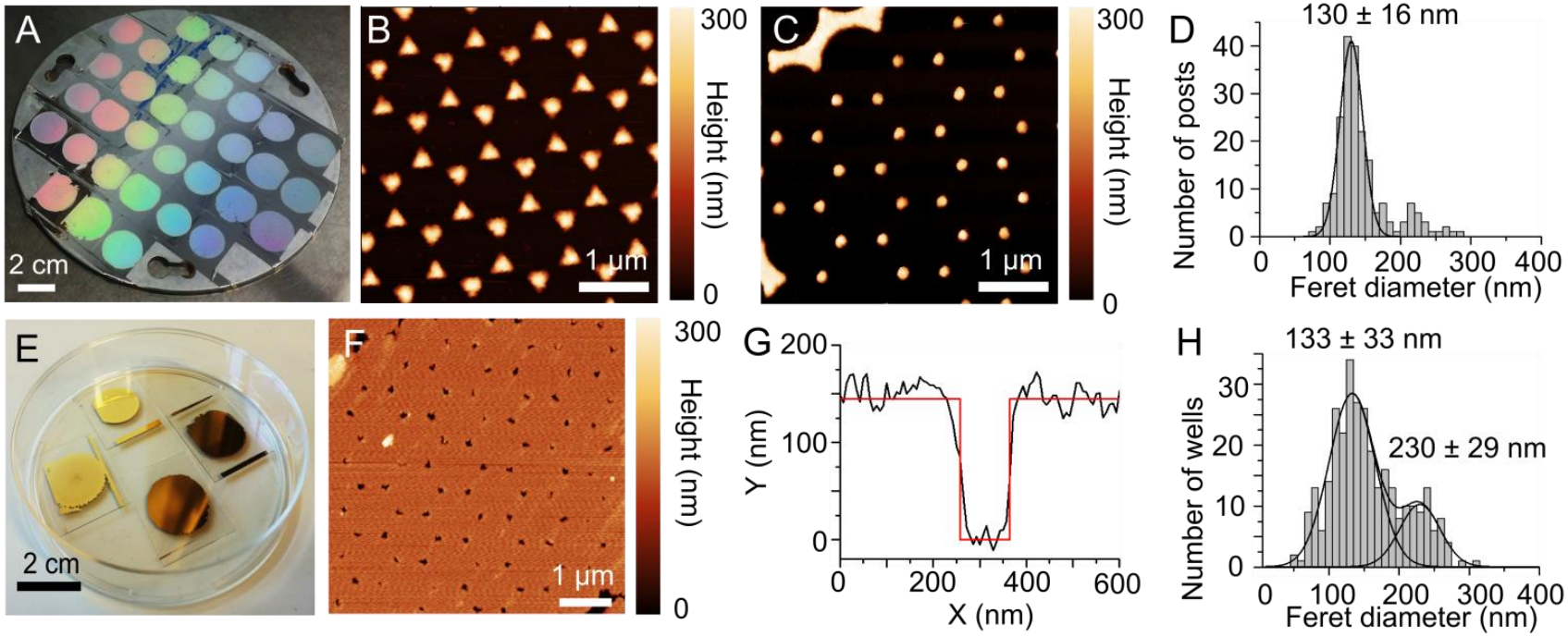

Figure 3.3. Posts and wells fabricated using nanosphere template. **(A)** Structural coloration from the bead diffraction pattern following Al evaporation. **(B)** Large, triangular posts formed by Al deposition without bead annealing. **(C)** Smaller, circular posts formed after beads were annealed for 20 s. **(D)** Distribution of Feret diameter of posts formed using a bead template annealed for 20 s. **(E)** Completed gold ZMWs. **(F)** AFM of ZMW wells formed after dissolving the narrow Al posts. **(G)** AFM profile of depth of individual well. **(D)** Distribution of Feret diameter of wells formed with a bead template that was annealed for 20 s.

3.3.2 Optical properties of ZMWs

To predict the behavior of these ZMWs under illumination with different wavelengths of light, finite element modeling of the electric field was conducted using COMSOL Multiphysics software, which numerically solved Maxwell's equations for an electromagnetic wave at normal incidence to the waveguide. The simulation was first validated by confirming that its results when using a perfect conductor in a vacuum were consistent with the analytical solution for a cylindrical waveguide (Jackson, 1999). Subsequently, the simulation was run with the parameters for the real materials (glass, gold, and water) for a waveguide with the geometry for beads that had not been melted, i.e. roughly triangular with concave sides and legs of approximately 400 nm. Even for a well that was an excessive 1200 nm deep, that ZMW was unable to attenuate a 600 nm wavelength electromagnetic field inside the lumen of the well (Fig. 3.4A). Thus, the melting step described earlier is essential for proper ZMW function.

To test how well narrower, circular wells would work, we repeated those simulations using a geometry like that of our physical wells; 140 nm deep and 200 nm wide (a conservative estimate of diameter representing the division between the main population of smaller wells, averaging 133 nm, and the population of larger wells averaging 230 nm). At 450 nm wavelength, a 600 nm wavelength electromagnetic field was attenuated inside the well, gradually decreasing intensity from the entrance to the exit of the ZMW (Fig 3.4B). For 700 nm wavelength, attenuation of that same electromagnetic wave was more abrupt, as expected (Fig 3.4C).

To validate this theoretical finding, we then measured the transmission of light of through our guides using several bandpass filters in line with the white lamp on the

illumination tower of our TIRF/epifluorescence microscope. To see the geometric pattern of the wells, an image was taken using that white light with no filters and turned to a high intensity, allowing the wells to be imaged despite their attenuation of transmitted electromagnetic waves. The representative half of a microscope field (Fig. 3.4D) was imaged using the same dual view two-channel simultaneous imaging system used for FRET. The image thus displays the number and arrangement of wells accessible in a typical smFRET experiment. Such an array contains 1500-2000 usable wells, as well as several transparent, bright defects where the grain boundaries of the bead domains had been located. Although those defects do not provide functional data from ZMW-bound molecules, they do not interfere with signals from the other wells, and aid in registration of multi-channel images.

Bandpass filters were then applied to restrict the wavelengths used. Each filter had a bandwidth of 10 nm, and filters were used for wavelengths spanning 450 nm to 700 nm, in increments of 50 nm. To account for an uneven spectrum of the white lamp and the camera sensitivity, the transmission through the guides at each wavelength was normalized to the transmission through large defects, where no attenuation is expected. The wells are dimly distinguishable at short wavelengths, like 450 nm (Fig 3.4E), but nearly invisible at longer wavelengths, like 700 nm (Fig 3.4F). As predicted, the transmission through the wells were all <8%, and exhibited a generally decreasing trend with longer wavelengths. An exception is a peak at 500 nm; for which gold is known to have a greater transmission.(Houston and Moore, 1928)

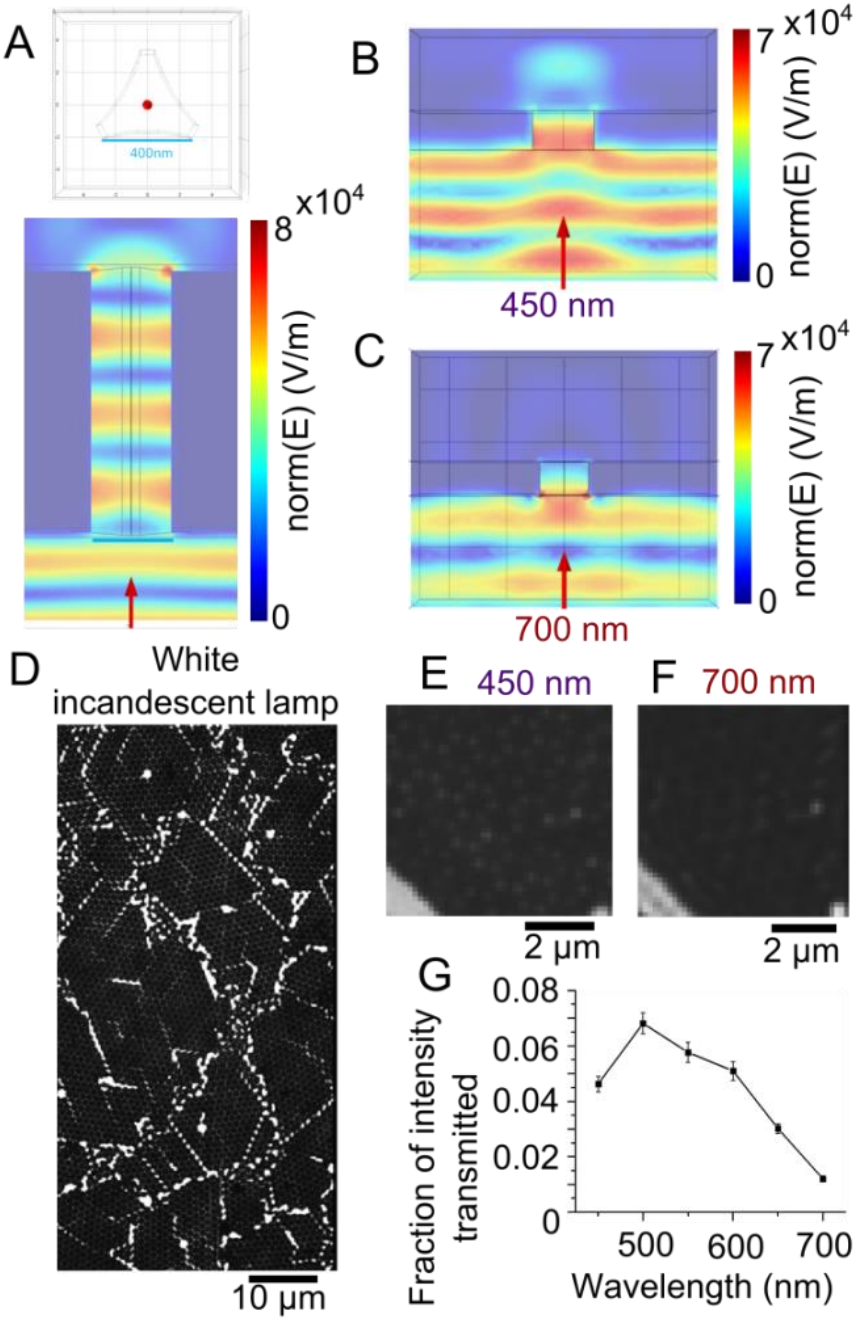

Figure 3.4. Simulation and empirical measurement of ZMW transmission of light of various wavelengths. **(A)** Cross-section of FEM model of unmelted, triangular ZMW with ~400 nm width and 1200 nm depth, which fails to attenuate light with 600 nm wavelength. FEM simulation demonstrating **a**ttenuation of 450 nm light **(B)** and 700 nm light **(C)** in circular well that is 200 nm wide and 140 nm deep. **(D)** White light illumination of ZMW array. Transmission of **(E)** 450 nm and **(F)** 700 nm light through ZMWs, which follows overall decreasing trend for longer wavelengths **(G).**

This greater transmission through the wells at 500 nm is *not* due to the actual transmission through the solid gold film away from the wells; that value is part of the background intensity that is subtracted when normalizing all of the measured intensities. Instead, that transmission is indicative of greater the permittivity and permeability of the gold at that wavelength, which has a role in determining the attenuation of the electric field within the ZMW. Nontheless, that attenuation remains substantial even at 500 nm.

3.3.3 Functionalization of ZMWs and application to single molecule fluorescence microscopy

We then subjected the gold and glass surfaces of these ZMWs to orthogonal surface treatments: we first passivated the gold cladding with a self-assembled monolayer (SAM) of methoxy-terminated, thiol-polyethylene glycol (PEG), and then functionalized the glass surface at the bottom of the wells with a 16:1 mixture of methoxy- and biotin-terminated silane-PEG. This passivation scheme was demonstrated to be more compatible with labeled proteins than poly(vinyl)phosphoric acid (PVPA),(Kinz-Thompson et al., 2013) which reduces the adsorption of negatively charged nucleic acids to the metallic surface and used for single molecule sequencing applications (Korlach et al., 2008).

Since smFRET applications could require these ZMWs to be used with fluorescently labeled proteins or nucleic acids, we loaded the wells with either Cy5-streptavidin (a protein), or a biotinylated DNA duplex with Cy3 and Cy5 on opposite strands (a nucleic acid), in positions known to give a FRET efficiency of approximately

0.5-0.6. The Cy5-streptavidin is able to directly bind the biotin-PEG-Si used to functionalize the glass bottoms of the wells (Fig. 3.5A), while the biotinylated DNA oligo requires the surface to be first treated with unlabeled streptavidin, which links the biotin on the PEG to that on the oligo using two of its four binding sites (Fig. 3.5C). After a 10 minute incubation at 100 pM concentration of labeled molecules, the number of wells containing single fluorescent proteins or DNA duplexes is maximized. Greater loading is obtained at higher concentrations, but many of the wells contain multiple molecules.

The Cy5-streptavidin gave clear fluorescence with single molecule photobleaches after 20-30 seconds of emission (Fig. 3.5B), while the biotin-Cy3-Cy5 DNA duplexes gave approximately 0.5 FRET for roughly the same amount of time before photobleaching, consistent with the values measured on bare glass (Fig 3.5E). Those durations of emission prior to photobleaching are approximately double that over bare glass, which has a measured bleaching time of about 10 seconds for both fluorophore schema used above. Finally, experiments are currently ongoing to quantify the reduction in background fluorescence that occurs (relative to bare glass) when freely-diffusing Cy3- or Cy5- labeled DNA duplexes are added to the described samples.

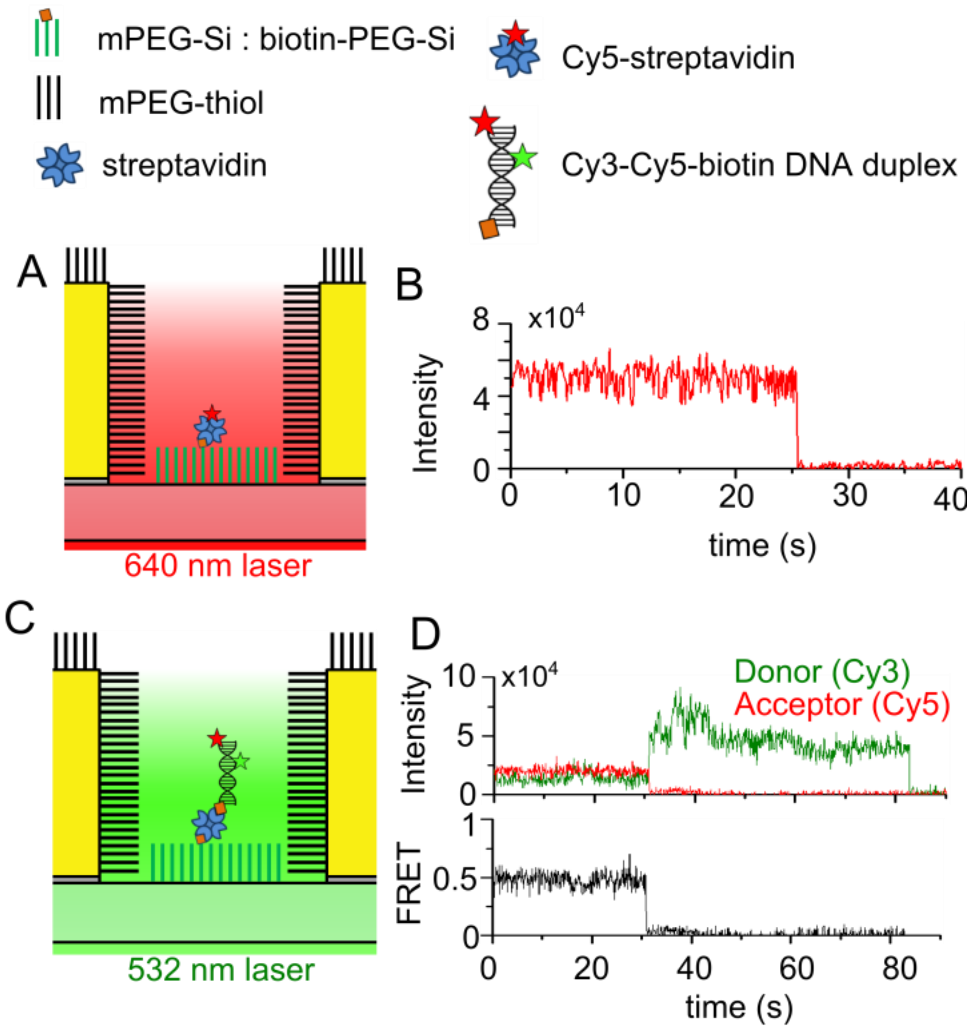

Figure 3.5. Single molecule fluorescence and FRET in passivated ZMWs. (A) Diagram of a ZMW fluorescence microscopy experiment in a gold well passivated with mPEG-thiol, as well as mPEG-Si and biotin-PEG-Si on the glass surface at the bottom of the well. A single molecule of Cy5-streptavidin resides at the bottom of the well, and is illuminated with a 640 nm laser. **(B)** Single molecule fluorescence trace from Cy5-streptavidin immobilized in a ZMW. **(C)** Diagram of a ZMW smFRET experiment in which a single molecule of biotin-Cy3-Cy5 DNA duplex is immobilized at the bottom of the well. **(D)** Donor and acceptor intensities (top) and FRET efficiency (bottom) for a biotin-Cy3-Cy5 duplex**.**

3.4 Conclusions

In single molecule fluorescence studies (like smFRET), background fluorescence from labeled substrates often requires their use at concentrations several orders of magnitude less than physiologic. That shortcoming can be addressed through the use of zero-mode waveguides that attenuate background fluorescence by restricting the observation volume. However, the need for expensive and specialized nanofabrication equipment to fabricate ZMWs has precluded their widespread adoption by the biochemical community. Here, we adopt nanosphere lithography to fabricate thousands of ZMWs in parallel, with sizes that are tunable via controlled fusing of polystyrene beads at their glass transition temperature. These robust and inexpensive structures can be made with minimal equipment, requiring only thermal evaporation beyond typical biology laboratory supplies. In addition, the droplet deposition method that we developed to form 2D crystal lattices can create very large (> 2cm) domains with large grain sizes (>10 μm), which potentially has important materials science applications including energy storage and semiconductor nanowire fabrication.

3.5 Detailed Methods

3.5.1 Slide cleaning

Borosilicate coverslips (No 1.5, Fisherbrand) were cleaned by 10 min sonication in acetone at 40 °C and rinsed three times with diH_2O, followed by a repeat of those

steps. They were then sonicated in 200 mM KOH for 20 min, rinsed six times with diH_2O, sonicated in ethanol for 10 min, rinsed three times with diH_2O, and dried with N_2.

3.5.2 Bead deposition

The following protocol describes the formation of 2D crystal lattices of beads on the coverslip surfaces, thus forming the mask for colloidal lithography. The cleaned coverslips were each placed in empty petri dishes with their slides tilted ajar, and placed underneath an overturned, transparent plastic storage box (76.2 cm x 48.6 cm x 34 cm) along with a small electric fan and a humidity meter (Fig. S1). To prepare the beads (Polybead® Microspheres 1.00 μm, Polysciences), 215 μL of bead suspension (in water, as provided by the manufacturer) was centrifuged in a 1.5 mL Eppendorf tube for 5 min at 15000 RCF at room temperature, and the water supernatant was removed by pipet. A beaker containing 200 mL of 75 °C H_2O was then added to the inside of the storage box humidity chamber and the fan was turned on, causing the humidity to steadily rise. In the meantime, the beads were resuspended in 220 μL of 1:400 TritonX:ethanol. When the humidity inside the plastic box reached the target of 90%, the lids of the Petri dishes were quickly closed. For each deposition, the plastic tub was briefly lifted to allow the pipetting of 6 uL of bead suspension into the center of a coverslip, with the lid of that Petri dish then replaced and the plastic container lowered back down. Each bead suspension puddle initially spread over a 20 second period, and then receded over the course of 3-5 minutes as the ethanol evaporated, leaving a 2D crystal lattice on the coverslip surface.

3.5.3 Bead annealing

A flat, milled aluminum plate was placed on top of a hot plate that was heated to 107 °C (the glass transition temperature of polystyrene), as verified by thermocouple with leads placed on the aluminum plate. When the temperature was stabilized, coverslips with 2D crystal lattices of beads were placed (one-at-a-time) on the surface for 5-25 s and then moved to another aluminum plate at room temperature for rapid cooling.

3.5.4 ZMW fabrication

Coverslips with 2D crystalline bead monolayers underwent thermal or e-beam evaporation (Kurt Lesker) of 3 nm Ti to serve as an adhesion layer, followed by evaporation of 300 nm of Al. The samples were then plasma treated for 30 min, followed by a delamination of the Al on top of the beads by a Scotch-tape lift-off. The polystyrene beads were dissolved by soaking in methylene chloride for 6 hours, followed by a methylene chloride and two isopropanol rinses. They samples (then containing Al posts) were plasma treated for 30 min, followed by thermal or e-beam deposition of a 3 nm Ti adhesion layer and 140 nm of Au cladding. The Al posts were then dissolved in Type A Al etchant (Transene) during 2 hrs of sonication, and the presence of wells was validated by AFM. If a larger than typical percentage of posts remained (>10%), the surfaces were lightly buffed using lens paper (Thor labs) to disrupt gold caps on the Al posts, and subjected to one more hour in Al etchant.

3.5.5 ZMW functionalization

The following protocol describes the use of orthogonal thiol chemistry to passivate the gold cladding, and silane chemistry to functionalize the glass bottoms of the wells. The fabricated ZMWs underwent a repeat of the cleaning process used for the initial coverslips (see "Slide Cleaning"), but with no diH_2O rinse following sonication in ethanol. Instead, they were treated with 100:5:1 methanol : glacial acetic acid : 3-aminopropyl-triethoxysilane overnight, followed bythree diH_2O rinses, 1 min sonication in EtOH, and were allowed the air dry. The samples then were treated for 3 hrs with 250 mg/mL polyethylene glycol (PEG) in 100 mM $NaHCO_3$. 95% of the PEG used was mPEG-succinimidyl valerate (MW 2,000, Laysan), while 5% was biotin-PEG-succinimidyl carbonate (MW 2,000, Laysan). The unbound PEG was rinsed with diH_2O, followed by drying with N_2. The samples were then treated overnight with 5 μM mPEG-thiol (MW 2,000, Laysan) in ethanol, before being rinsed and dried again with N_2. Functionalized ZMWs were vacuum sealed and stored at -20 °C until use.

3.5.6 Fluorescence microscope

A custom-built objective-type total internal reflection fluorescence (TIRF) microscope was used with the incidence angle adjusted to be normal to the sample, to illuminate the ZMWs in epifluorescence rather than TIRF mode. The microscope was based on a commercial inverted microscope (Eclipse Ti, Nikon) with a 1.49 N.A.100× oil immersion objective (Apo TIRF; Nikon) . Excitation of Cy3 (and sensitized Cy5 during FRET) was achieved with a 532 nm laser,(CrystaLaser, Inc., while a 640 nm laser

(Coherent, Inc.) was used to directl excite Cy5. Fluorescence intensities of Cy3 channel (550-620 nm) and Cy5 channel (660-720 nm) were separated by a Dual View splitter (Photometrics) and recorded with an electro multiplying charge-coupled device (EM-CCD) camera (Cascade II, Photometrics)

3.5.7 Microscopy buffers

Single molecule fluorescence recordings were carried out at 23 °C in buffer consisting of 50 mM Tris- HCl [pH 7.5], 15 mM $Mg(OAc)_2$,30 mM NH_4Cl, 70 mM KCl. An enzymatic deoxygenation system of 0.3% (w/v) glucose, 300 μg/ml glucose oxidase (Sigma-Aldrich), 120 μg/ml catalase (Roche), and 1.5 mM 6-hydroxy-2,5,7,8-tetramethyl-chromane-2-carboxylic acid (Trolox, Sigma-Aldrich) was added to the final single-molecule imaging solutions to reduce fluorophore photobleaching and blinking(Chen et al., 2011).

3.5.8 Biotin-Cy3-Cy5 DNA duplex

DNA oligos from Integrated DNA Technologies (IDT) had the following sequences, based on previously published data (McCann et al., 2010):

CGT GTC GTC GTG CGG CTC CCC AG/iCy3/G CGG CAG TCC

/5Cy5/GGA CTG CCG CCT GGG GAG CCG CAC GAC GAC ACG ACA AAG/3Bio/

These single-stranded DNA oligos were mixed together at a 1 μM concentration and

annealed by placing in a heating block at 95 °C, which was turned off to allow the samples to gradually cool to room temperature and then they were placed at 4 °C.

3.5.9 ZMW fluorescence microscopy

All imaging was conducted at 100 ms time resolution unless otherwise noted. Cy5 streptavidin (Thermofisher) was added to the ZMW array at 100 pM concentration and allowed to diffuse into the wells for 10 min before being rinsed away by illumination buffer (with deoxygenation components) described above. For experiments using biotin-Cy3-Cy5 DNA duplex, 0.5 mg/mL of unlabeled streptavidin was added to the ZMWs first. After 10 min incubation, the slides were rinsed with buffer, and 100 pM of the labeled, biotinylated duplex was added. After another 10 min of incubation, the unbound duplex was washed away with illumination buffer.

3.5.10 Data processing

Fluorescence traces were extracted from recorded image stacks using ImageJ using lab software (Chen et al., 2011), and analyzed using Matlab**.** FRET efficiency was calculated according to (Ha et al., 1999):

$$E = \left(1 + \frac{I_D}{I_A - \chi I_D}\gamma\right)^{-1}$$

where I_D and I_A are the raw fluorescence intensities of the donor and acceptor, χ is the cross-talk of the donor emission into the acceptor recording channel, and γ accounts for

the ratios of quantum yield and detection efficiency between the donor and the acceptor. ImageJ was also used to identify the location of defects in the ZMW array using images of the microscope fields taken with the white light lamp on the illumination tower. The locations of those defects were used to exclude fluorescence traces originating from the defects.

4. Conclusions

Protein synthesis by the ribosome is a fundamental process carried out by all cells and essential to life. As an RNA enzyme, or ribozyme, the ribosome is hypothesized to have played a unique role as a lynchpin connecting the "RNA World" of self-replicating RNAs that function in both catalysis and information storage, with the world of proteins that would later evolve (Copley et al., 2007; Neveu et al., 2013; Robertson and Joyce, 2012). The RNA World refers to the general idea that evolution based on RNA replication preceded the advent of protein synthesis, and was first proposed (Crick, 1968; Orgel, 1968; Woese, 1967) before knowledge of extant RNA catalysts. The later discoveries of such ribozymes (Guerrier-Takada et al., 1983; Kruger et al., 1982) triggered extensive discussion of RNA's role in the origin of life (Pace and Marsh, 1985; Sharp, 1985), culminating in the coining of the term "RNA World" (Gilbert, 1986). The ribosome structures showing the absence of protein involvement in peptide transfer (Ban et al., 2000; Wimberly, 2000; Yusupov, 2001) were considered crucial evidence leading to

widespread acceptance of this theory. In addition, studies of ribosomal rRNA sequences demonstrated they may not have been merely catalytic, but may also store sufficient information to themselves be self-replicating (Root-Bernstein and Root-Bernstein, 2015), and thus have predated the existence of DNA and cells.

Thus, an understanding of how the ribosome converts the chemical energy of environmental metabolites into mechanical motion is of fundamental importance. The thermodynamics of translation transcends the ribosome's pharmacological significance in antibiotics, viral frameshifting, and stop-codon read-through for genetic diseases, but has a deeper significance in understanding the origin of life and its relationship to free energy and entropy (Schrödinger, 1943).

The idea that EF-G can act as a motor protein (like myosin, dynein, or kinesin) whose power stroke drives translocation appears to ascribe a more active role to that protein than the Brownian ratchet mechanism. In the prevailing Brownian ratchet model, spontaneous thermal fluctuations of the tRNAs, mRNA, and rRNA would undergo the initial motion required for translocation independent of EF-G, the ratchet pawl. However, Feynman demonstrated in his discussion of the hypothetical Brownian ratchet that the pawl cannot be passive, there must still be a temperature difference or an energy contribution for the ratchet to progress unidirectionally. In the case of a Brownian ratchet like that proposed by Frank et al (2000, 2010), EF-G still actively converts chemical metabolic energy into mechanical motion. Although the tRNAs may move spontaneously (in rough concert with rotations of the large and small subunits with respect to each other) that must still be followed by EF-G locking out reverse translocation, which necessarily requires a significant energy contribution (like GTP

hydrolysis) according to the Second Law of Thermodynamics.

Our group has strongly diverged from the field's consensus on the Brownian ratchet model, first demonstrating that EF-G will attempt the start of a rotational motion even when the tRNAs are blocked from moving on their own by viomycin (Chen et al., 2016) , and here demonstrating that under ongoing translation and rapid turnover, the tRNAs do not even undergo the motions that have been so intensively studied by the field for the past decade. In fact, those fluctuations only become observable when using non-physiologically low concentrations of EF-G that delay the onset of EF-G binding. That delay allows tRNA to explore conformations that are not reflective of their actual physiological trajectory. However, our FRET pairs did not assess the rotation of the large and small subunits with respect to one another, a process that could still occur.

The EF-G concentration at which translation is studied is thus more than a quantitative consideration; it directly determines which branch of a mechanistic pathway translation follows. That is a crucial qualitative distinction, and underscores the importance of conducting smFRET experiments with high concentrations of labeled substrates. Such experiments are impeded by technical barriers; a physiologic 10-20 μM concentration of fluorescently-labeled EF-G would give a saturating level of background fluorescence with conventional TIRF microscopy.

The use of zero-mode waveguides can attenuate that background fluorescence by restricting the observation volume, thus allowing labeled EF-G to be used at micromolar concentrations. However, the need for expensive and specialized nanofabrication equipment to make ZMWs has prevented their widespread adoption by the biophysical community. To address that concern, we developed a method using benchtop nanosphere

lithography to fabricate thousands of ZMWs in parallel, with sizes that are tunable via controlled fusing of polystyrene beads at their glass transition temperature. Those robust and inexpensive structures can be made with minimal equipment, and provide a critical tool to study processes that behave fundamentally differently in different concentration regimes.

5. Future Directions

5.1 Prokaryotic translation: Monitoring fluorescently labeled EF-G with simultaneous tRNA-L11 or tRNA-tRNA FRET

To further study the dynamics of EF-G and tRNAs on the ribosome during ongoing translation, we will use those ZMWs along with EF-G labeled with an orthogonal fluorophore to the Cy3 and Cy5 used for tRNA-tRNA and tRNA-L11 FRET. We have labeled a S453C mutant of EF-G with Bodipy-FL via a maleimide-cysteine conjugation, and verified that it is active *in vitro*. That fluorophore is excited by the 488 nm laser, rather than the 532 nm and 640 nm lasers used for Cy3 and Cy5. In combination with a QuadView multi-channel simultaneous imaging setup, we can conduct the same tRNA-tRNA and tRNA-L11 FRET experiments done with 2 μM unlabeled EF-G, but with labeled EF-G that would reveal whether EF-G binding occurs before the tRNA arrives to the A-site to form the non-fluctuating intermediate state (supporting the model of EF-G driving the non-fluctuating intermediate state formation by binding to L7/L12 rather than the A-site, allosterically affecting the PRE complex tRNA geometry), or whether EF-G binding occurs after the tRNA arrives (supporting the model that EF-G binding immediately induces a chimeric ap/ap state as it “hands” the A-

site tRNA to the P-site, as described by Zhou et al. 2013) .

Since the 488 nm laser will excite not only the bodipy-FL-EF-G, that experiment would require alternating laser excitation during each frame between the 488 nm laser (which will indicate whether bodipy-FL-E-FG has bound to the ribosome on its emission channel), and the 532 nm laser (which will allow Cy3 and Cy5 emissions to be detected on their respective channels to measure FRET). Since there is no spectral overlap between the bodipy-FL-E-FG and Cy5, the frames illuminated by the 488 nm laser may also be illuminated by the 640 nm laser to have the benefits of ALEX to detect acceptor photobleaching without any further loss of time resolution.

5.2 Eukaryotic: Studying the mechanism of nonsense suppression drugs

In addition to these efforts to study the prokaryotic ribosome, we have developed an *in vitro* system for conducting tRNA-tRNA smFRET using ribosomes purified from brine shrimp (*Artemia*). There are many fundamental differences in prokaryotic and eukaryotic translation (which is the reason anti-ribosomal antibiotics are so specific for the target, rather than the host). Rather than using the elongation factors EF-Tu and EF-G, the eukaryotic ribosome uses eEF-1a and eEF-2. The 80S eukaryotic ribosome is also much larger than its prokaryotic component (4.2 MD vs 2.7 MD), with a higher percentage of protein (rather than rRNA) compared to prokaryotic ribosomes. The study of eukaryotic translation using smFRET is an important future direction for which we have accumulated substantial preliminary data.

Initiation of translation requires many more initiation factors in eukaryotes, which

is partly a result of differences in RNA processing. In prokaryotes, the 5′ end of mRNA is available to ribosomes immediately after it is transcribed. In eukaryotes, pre-mRNA must be processed and transported to the cytoplasm before translation can begin, which allows mRNA time to form complex secondary structures that must be unfolded by helicase initiation factors (ex eIF-4, which finds the 5' end via its end cap). *In vitro*, this complicated eukaryotic initiation process poses major challenges for reconstituting a functional system on a microscope slide with purified components. However, we were able to use a cricket paralysis virus (CrPV) internal ribosome entry site (IRES) to overcome this challenge. IRESs are RNA elements that allow translation initiation in an end-independent manner, and are often found in the 5' UTR of RNA viruses. The CrPV IRES forms a complex secondary and tertiary structure that resembles an initiator tRNA on the mRNA, thus allowing several steps in translation initiation to be skipped (Fig 4.1). By simplifying the initiation process, CrPV mRNAs allowed us to robustly carry out eukaryotic translation while measuring tRNA-tRNA smFRET.

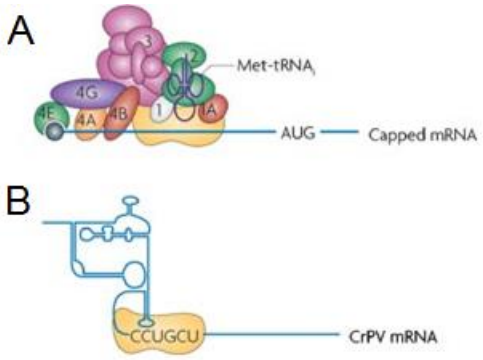

Figure 4.1: Eukaryotic initiation. (A) Schematic of canonical eukaryotic cap-dependent translation initiation displaying the many initiation factors required and (B) of the cricket paralysis virus (CrPV) IRES, which requires no additional initation factors. (Fraser and Doudna, 2007)

The mRNAs used in the prokaryotic experiments were designed to require Phe, Val, and Tyr tRNAs, as those were commercially available. Now having the capability to monitor eukaryotic ribosomes with smFRET while they synthesize polypeptide chains *in vitro*, we will use that system to study nonsense suppression by ataluren, a drug that allows a Trp tRNA to be incorporated in place of a nonsense stop codon. The mRNAs for that study (encoding either FKVRQWLM or FKVRQStopLM) required several tRNAs that were not commercially available. Fortunately, a collaborating group (Pan et al., 2009) developed a method to purify specific tRNAs from a bulk mixture using complimentary oligonucleotides affixed via biotin to streptavidin beads. Due to biotin contamination, those tRNAs were unsuitable for the functionalized slides used in smFRET; too many labeled tRNAs stuck to the microscope surface, rather than appropriately binding to the ribosome. For use with smFRET, we instead affixed the oligonucleotides to the beads using an NHS-ester-amine linkage, and subsequently purified, charged, and fluorescently labeled the necessary tRNAs for that study.

To study the ability of ataluren to suppress nonsense mutations by reading through aberrant stop codons, the most relevant codon in our mRNAs are those encoding either Trp or Stop at the same position. smFRET allows us to measure the tRNA-tRNA distance parameters and dwell times of any substates along the translation reaction coordinate. Thus by studying FRET between Trp-tRNA^{Trp} (Cy3) and either the preceding Arg-tRNA^{Arg}(Cy5) or subsequent Glu-tRNA^{Glu}(Cy5), we can test for any spatial or kinetic differences between when Trp-tRNA^{Trp} (Cy3) is correctly incorporated at a Trp codon, or when it is incorporated at a stop codon due to the effect of ataluren. Using this

approach, we can discern the step(s) along the elongation cycle at which the drug exerts its effect, as well as any structural changes in tRNA positioning that it may cause.

Our initial data was collected using FRET between Glu-tRNA^{Glu}(Cy5) in the ribosomal P-site, and Trp-tRNA^{Trp} (Cy3) in the ribosomal A-site. Before monitoring ongoing translation, we sought to first study the positions of the tRNAs while stalled. Thus, recordings of this complex were conducted in the absence of eEF-2, the eukaryotic analog to EF-G. Unlike in the prokaryotic ribosome, almost no classical-hybrid fluctuations were observed; instead, the eukaryotic PRE state occupied a single FRET state at approximately 0.4. We then added eEF-2 and GTP, which would catalyze a translocation from this stalled PRE state. Soon after injection, the tRNAs adopted a higher FRET state, presumably corresponding to the POST state, which persisted until E-site dissociation (Fig 4.2).

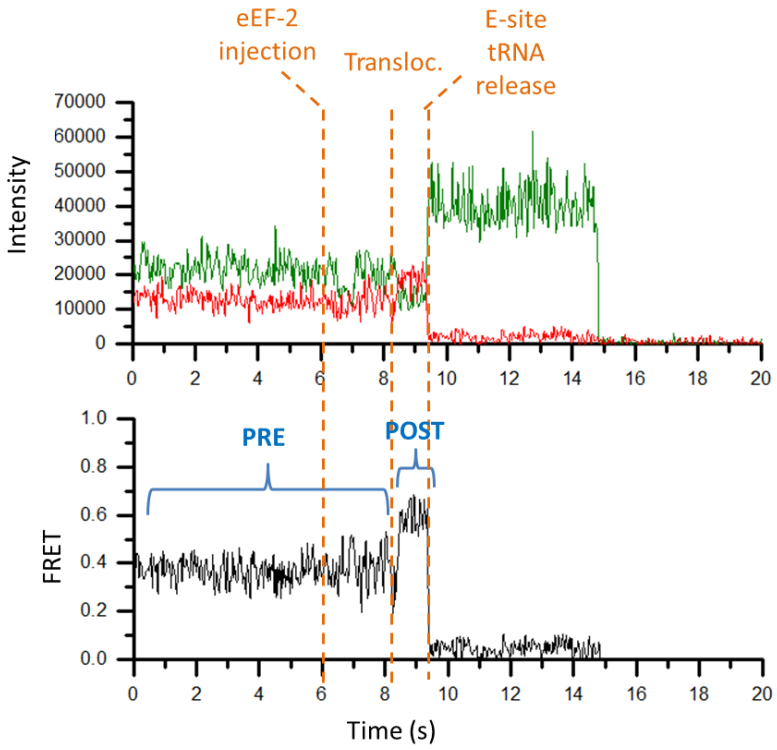

Figure 4.2: Eukaryotic translocation monitored by tRNA-tRNA smFRET. PRE state FRET between $tRNA^{Glu}$(Cy5) in the ribosomal P-site, and Trp-$tRNA^{Trp}$ (Cy3) in the ribosomal A-site converted from a value of ~0.4 to ~0.6 soon after injection of eEF-2. That higher FRET post state persisted until the E-site tRNA ($tRNA^{Glu}$(Cy5)) dissociated.

However, as we demonstrated in our studies of the prokaryotic ribosome, translation from a stalled ribosome may qualitatively different than ongoing translation in the constant presence of eEF-2. Thus before we can test the effect of ataluren on nonsense suppression, we will characterize the eukaryotic ribosome using these tRNA-tRNA FRET pairs during ongoing translation.

Appendix A. Deconvolution of camera instrument response functions

A.1. Abstract

Temporal sequences of fluorescence intensities in single molecule experiments are often obtained from stacks of camera images. The dwell times of different macromolecular structural or functional states, correlated to characteristic fluorescence intensities, are extracted from the images, combined into dwell time distributions which are fitted by kinetic functions to extract average rate constants. The frame rate of the camera limits the time resolution of the experiment and thus the fastest rate processes that can be reliably detected and quantified. However, including the influence of discrete sampling (framing) on the detected time series in the fitted model enables rate processes near to the frame rate to be reliably estimated. This influence, similar to the instrument response function (IRF) in other types of instruments, such as pulsed emission decay fluorimeters, is easily incorporated into the fitted model. The same concept applies to any temporal data that is low-pass filtered or decimated to improve signal to noise ratio.

A.2. Introduction

The development of highly sensitive cameras has made it possible to record single-molecule fluorescence for studying the structural dynamics, kinetics, and spatial positioning of macromolecular systems. Fluorescence measurements of individual molecules during activity (e.g., stepping of molecular motors (Yildiz et al., 2003), fluorescence resonance energy transfer (FRET) from dual-labeled samples (Roy et al.,

2008), nucleation and growth of protein binding zones on DNA strands (3) can provide unique mechanistic insights into transitions in complex processes that are inaccessible via ensemble measurements. With sufficient time resolution, discrete states can be resolved by examining characteristic amplitudes (i.e. fluorescence intensities) and dwell times, *t*, of individual reaction events. The underlying kinetic mechanisms and the characteristic reaction times, τ, can be determined by fitting kinetic models of these mechanisms to the distribution of dwell times, either by creating histograms of the data for fitting with least squares optimization or maximum entropy (Brochon, 1994), or by fitting un-binned data using maximum likelihood estimation (Bevington and Robinson, 2002).

Often the most appropriate models to fit such dwell time distributions are linear combinations of the exponential probability distribution function (pdf) *p*:

$$p(t,\tau) = \frac{1}{\tau} e^{-\frac{t}{\tau}} \quad \text{(Eq A. 1)}$$

This pdf describes the probability density of observing an event of duration *t*, which is terminated by a process occurring at an average rate of $1/\tau$ that does not depend on how long a particle has already occupied that state, i.e. it is "memoryless". Since nearly all experiments studying such events have a finite time resolution, limiting the minimum accessible event duration that can be observed, it becomes necessary to renormalize the pdf, so that total probability, e.g. the probability density integrated over the experimental range, is equal to one:

$$p(t,\tau,t_m) = \frac{\frac{1}{\tau}e^{-\frac{t}{\tau}}}{\int_{t_m}^{\infty}\frac{1}{\tau}e^{-\frac{t}{\tau}}dt} = \frac{1}{\tau}e^{-\frac{t-t_m}{\tau}} \quad \text{(Eq A. 2)}$$

where t_m is the minimum detectable dwell time. In this simple case, the best estimate for τ can be calculated directly from the dwell time data points, t_i, using the relation $\tau = \sum \frac{t_i}{N} - t_{min}$ (Supplement).

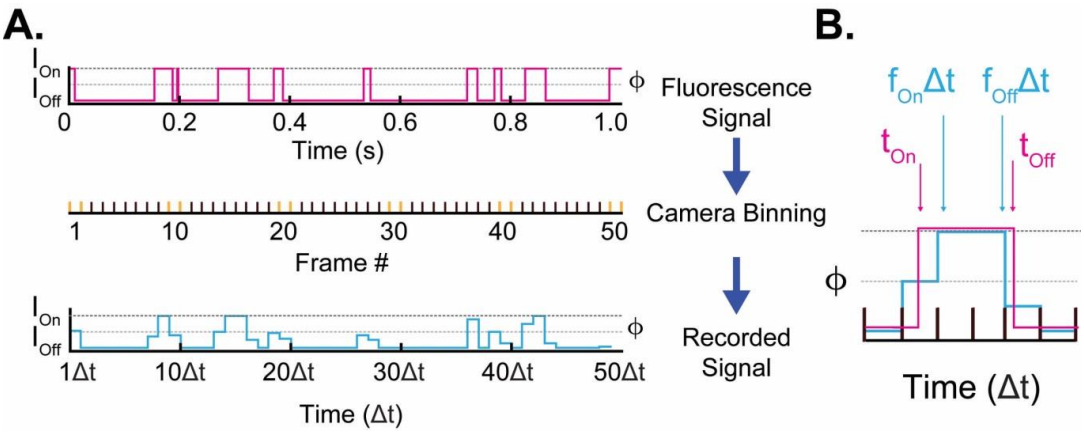

Figure A.1. Effect of camera binning when recording a fluorescence signal. **A.** A fluorescence signal repeatedly transitions, with rate $1/\tau$, between a maximum (I_{on}) and a minimum (I_{Off}) over time (*top*). Binning of intensity from recording frame-by-frame with a camera (*middle*) results in an output signal that is distorted (*bottom*) relative to the input (*top*). **B.** Collecting in discrete intervals obscures the true start (t_{on}) and end (t_{off}) of an event, indicated by crossing a threshold $\phi = 0.5$ ($I_{on} - I_{off}$). The recorded dwell time of an event, calculated from $f_{on}\Delta t$ and $f_{off}\Delta t$, can be greater or less than the true value. In this trace, the lifetime of the signal is τ = 40 ms, but is calculated from the recorded signal as τ_d=53ms, a 25% error in accuracy.

In a typical single molecule fluorescence experiment recorded on a video camera, the camera frame rate sets a limit on experimentally resolvable dwell times. Image sequences from a camera with frame interval Δt effectively bins signal photons into sets

of frame numbers (f_i) (Fig 1A). The detected duration of each event is restricted to integer multiples of Δt due to binning of the photons into each frame that results in a set of discrete dwell times $t_d = f_i \Delta t$ that form a distribution. Individual values of t_d may be shorter or longer than the actual times, t_i, depending on the stochastic start time of each event (Fig. A.1B) and depending on the length of Δt relative to t_i. This binning is a type of quantizing noise and distortion. The minimum detectable event, f_m, may be greater than one frame if noise in the signals causes uncertainty for very short events. If the average lifetimes, τ, of the relevant states are much greater than $f_m \Delta t$, the effects of losing the shortest events and the binning of photons are insignificant and the discrete distribution, t_d, can be approximated as continuous. In such cases, the characteristic lifetimes can be estimated by fitting combinations of the exponential pdfs given in equation 2 to the data.

Often, this approximation is not valid, though, since the frame interval, Δt, must be large enough to collect sufficient photons to provide a reliable intensity value. This requirement and the camera readout rate usually limit the time resolution to the millisecond range, while many biophysical processes often are in the millisecond to sub-millisecond range. As τ approaches $f_m \Delta t$, estimation of the lifetime becomes increasingly inaccurate since a large proportion of the events occupy only one or a few frames and their counts are unreliable.

Here we show that accounting for digitization by the camera enables estimation of the characteristic lifetime more reliably and without bias. This is accomplished by using modified probability functions which transform the continuous probability distributions into discrete functions, termed probability mass distributions, that account for the

discretizing of continuous dwell times into an integer number of camera frames, and for missed events shorter than the minimum reliably detectable dwell time. The probability functions are derived, and estimating lifetimes with these corrected distributions are compared to the more common method of using the continuous distribution.

A.3. Results and Discussion

Consider the case in which occupancy of a reaction state, an 'event', is detected by observing a significant change in fluorescence intensity (the ON state) relative to that of the background (the OFF state) (Fig A.1A). The frames defining the beginning and end of an event are detected when the fluorescence signal has crossed a threshold, ϕ, which is defined as the proportion of the difference between the ON and OFF state (i.e. when ϕ = 0.5, an event start is detected when the fluorescence has risen from the OFF state to half-way up to the expected ON fluorescence level).

Each dwell time is recorded as the difference between $f_{OFF}\Delta t$ and $f_{ON}\Delta t$ (Fig 1B). Although t_d values are measured in discrete units of time, the underlying process generating these dwell times is defined by the continuous exponential distribution p (Eq. A.1), which t_d therefore should also follow. However, since the t_d variable is discrete, the amplitude must be normalized by summation, rather than by integration, as was done for pdf p (Eq. A.2). In this case, 'missing' short dwell times are accounted for by limiting the range of the summation to $f = f_m, f_m+1 \ldots \infty$:

$$p_d(f, \Delta t, \tau, f_m) = \frac{e^{-\frac{f\Delta t}{\tau}}}{\sum_{f=f_m}^{\infty} e^{-\frac{f\Delta t}{\tau}}\Delta t} = \frac{1}{\Delta t}\left(1 - e^{-\frac{\Delta t}{\tau}}\right) e^{-\frac{\Delta t}{\tau}(f - f_m)} \quad \text{(Eq A. 3)}$$

where the summation can be solved exactly since it is a geometric series. This is the "camera probability mass distribution function" (cpmf) that should be fitted to the data f_i, to estimate τ. For the single exponential case, the most likely value of τ can be derived directly from $p_d(\tau)$:

$$\tau = \frac{\Delta t}{\ln\left(1 + \frac{1}{f_{av} - f_m}\right)} \quad \text{(Eq A. 4)}$$

where, $f_{av} = \sum \frac{f_i}{N}$ is the average number of frames measured for the event.

Even when $f_m = 1$, the thresholding of intensity for detection causes events shorter than $\phi\Delta t$ not to be reported, reducing the amplitude of the first bin. This leads to an error in calculation using Eqs. A.3 and A.4 that can be corrected by an additional scaling amplitude $A = 1 \Big/ \phi + \frac{\tau}{\Delta t}\left(1 - e^{-\frac{(1-\phi)\Delta t}{\tau}}\right)$. If $f_m > 1$ or $\phi = 1$, the value of ϕ drops out and Eqs. A.3 and A.4 are exact. Eq. A.4 also approaches $\tau = (f_{av} - f_m)\Delta t$ when $\tau >> f_m\Delta t$ or when $\phi = 0$. Both of these relationships for τ give much better estimates of τ than simply $f_{av}\Delta t$ (see Supplement for details).

Given that that the dwell time t_d is a discrete variable, Eq. 3 can alternatively be derived as a geometric distribution, the discrete form of the exponential distribution, defined as:

$$pmf_{geo} = p_1(1 - p_1)^k \quad \text{(Eq A. 5)}$$

The geometric distribution gives the probability of observing one 'success' (e.g. a coin landing on heads) after k trials (e.g. coin flips), when the probability of one successful trial is p_1. For dwell times, each trial, k, is the number of frames, f, over which t_d is recorded, whereas the probability of recording it in the first frame is given by $p_1 =$

$\left(1 - e^{\frac{-\Delta t}{\tau}}\right)$. Substituting these into pmf_{geo} (Eq. A.5), with the additional normalizing factor $1/\Delta t$, results in the expression given for p_d (Eq. A.3).

A.3.1 Higher order probability distribution functions

For systems containing more complex reaction schemes, models consisting of linear combinations of exponential pdfs can be fit to the data (see Supplement). For example, if a transition between two biochemical states can occur through two independent parallel pathways, each with characteristic lifetimes τ_1 and τ_2, the observed durations of the starting state is described by the sum of two single exponential pdfs:

$$p_2(\tau_1, \tau_2) = \frac{C\frac{1}{\tau_1}e^{-\frac{t}{\tau_1}} + (1-C)\frac{1}{\tau_2}e^{-\frac{t}{\tau_2}}}{Ce^{-\frac{t_m}{\tau_1}} + (1-C)e^{-\frac{t_m}{\tau_2}}} \quad \text{(Eq A. 6)}$$

where C and (1 - C) are the relative populations of the two states and the denominator renormalizes the pdf to account for the minimum detectable event length, t_m. As shown in the Supplement, the camera probability function of this distribution with minimum detectable frame number, f_m, is:

$$p_{d2}(\tau_1, \tau_2)$$

$$= \frac{1}{\Delta t}\frac{C\tau_1\left(1 - e^{-\frac{\Delta t}{\tau_1}}\right)^2 e^{-\frac{\Delta t}{\tau_1}(f-1)} + (1-C)\tau_2\left(1 - e^{-\frac{\Delta t}{\tau_2}}\right)^2 e^{-\frac{\Delta t}{\tau_2}(f-1)}}{C\tau_1\left(1 - e^{-\frac{\Delta t}{\tau_1}}\right)e^{-\frac{\Delta t}{\tau_1}(f_{min}-1)} + (1-C)\tau_2\left(1 - e^{-\frac{\Delta t}{\tau_2}}\right)e^{-\frac{\Delta t}{\tau_2}(f_{min}-1)}} \quad \text{(Eq A. 7)}$$

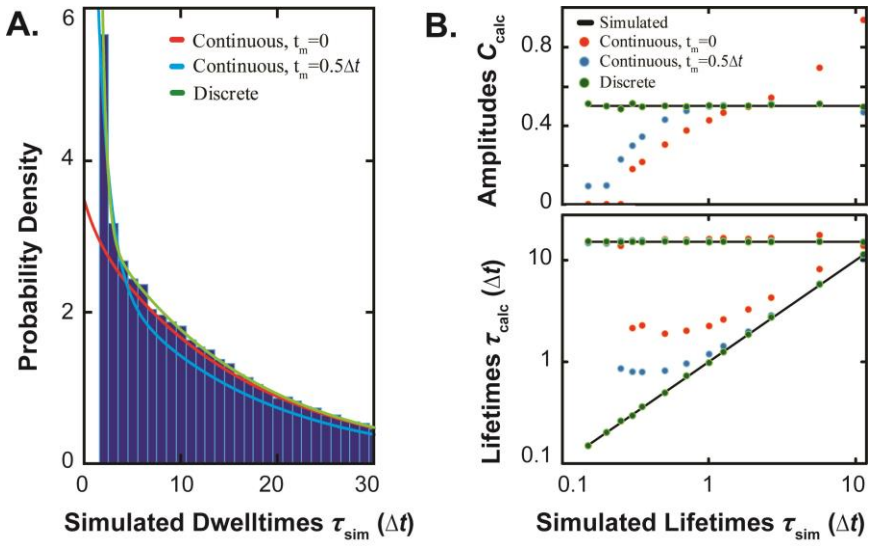

Figure A.2. Comparison of methods for fitting distributions of discrete dwell times. A. Distribution of discrete dwell times simulated with a fast component, τ_1 = 0.5Δt, a slow component, τ_2 = 15Δt, and amplitude C = 0.5, where Δt is the frame interval. This distribution was fitted by continuous pdf $p_2(\tau_1,\tau_2)$, with t_m = 0 (red) or t_m = 0.5Δt (blue), or by the camera pdf $p_{d2}(\tau_1,\tau_2)$ with f_m=2. The x-axis is plotted in units of Δt. **B.** Multiple simulations were performed with slow component τ_2 = 15Δt and fast components τ_1 over a range of 0.2Δt to 10Δt *and* C = 0.5. Green points are from $p_{d2}(\tau_1,\tau_2)$, f_m=2.

A.3.2 Evaluating the camera probability mass functions

Given the differences in the equations for the continuous pdf (Eqs. A.2 and A.6) and camera (discrete) pmfs (Eqs. A.3 and A.7), it is clear that they would fit distributions of dwell times differently. But to what extent do these functions deviate? Dwell time distributions were simulated by drawing two sets of random exponential numbers (based on pdf $p_2(\tau_1,\tau_2)$ with lifetimes τ_{sim1} and τ_{sim2} and C = 0.5), and digitizing these with ϕ = 0.5 and f_m = 2. N = 50,000 random numbers were generated for each set so as to test only the

accuracy of the distributions in returning the known lifetimes when fit to the camera-digitized data; precision is dealt with later. 13 different simulated distributions, with average lifetimes τ_{sim1} over a range of $0.2\Delta t$ to $10\Delta t$ and $\tau_{sim2} = 15\Delta t$, were fitted by $p_2(\tau_1,\tau_2)$ or $p_{d2}(\tau_1,\tau_2)$ (Eqns. A.6 or A.7) using maximum likelihood (MLE)-based optimization returning estimated values of the average lifetimes τ_{calc1} and τ_{calc2}, which are reported in units of the exposure time, Δt. An example of a simulated distribution for $\tau_{sim1} = 0.5\Delta t$ and $\tau_{sim2} = 15\Delta t$, fitted by pdfs $p_2(\tau_1,\tau_2)$ (t_m=0 or $\phi\Delta t$) or $p_{d2}(\tau_1,\tau_2)$ (f_m=2), is given in Fig. A.2A.

A.4 First order processes: extended derivations

A.4.1 Continuous exponential probability distribution functions for dwell time distributions

Descriptions of continuous exponential pdfs have been provided elsewhere (Bevington and Robinson, 2002; Colquhoun and Hawkes, 2009), but are described here in brief to serve as contrast to the discrete (camera) pmf. A continuous dwell time t of an event is calculated from its start and end times, t_{start} and t_{end}:

$$t = t_{end} - t_{start} \qquad \text{(Eq. A. S1)}$$

This is defined over the range of t=t_m…∞, where events that last less than some minimum time t_m are considered unreliable and excluded from the distribution. A distribution of dwell times of average lifetime τ is defined by the exponential probability function, P:

$$\mathrm{P} = Ae^{-\frac{\mathrm{t}}{\tau}} \qquad \text{(Eq. A. S2)}$$

Probabilities are expressed as some fraction of the total probability which conventionally is equal to one. Probability P can satisfy this by normalizing its amplitude A such that the

sum of all probabilities over the range of $t = t_m \ldots \infty$ equals 1, which for a continuous function is done by integration:

$$A \int_{t_m}^{\infty} e^{-\frac{t}{\tau}} dt = 1 \qquad \text{(Eq. A. S3)}$$

Solving for A and substituting it into Eq. A.S2 leads to:

$$p(t, \tau) = \frac{1}{\tau} e^{-\frac{t - t_m}{\tau}} \qquad \text{(Eq. A. S4)}$$

where $p(\tau)$ is the probability distribution function (pdf).

A.4.2 Discrete probability mass functions for dwell time distributions

A camera dwell time t_d, measured in integer (f) units of time (Δt), is a discrete form of the physical dwell time t described above. Dwell time t_d is defined over the range of $f = f_m, f_m+1 \ldots \infty$, where events that last less than some minimum number of frames $f_m \geq 1$ are considered unreliable and excluded from the distribution. Although discretized, these dwell times $t_d = f\Delta t$ are still expected to follow the exponential distribution (Eq. A.S2, and below):

$$P_d(\tau) = A_d e^{-\frac{f\Delta t}{\tau}} \qquad \text{(Eq. A. S5)}$$

Probability $P_d(\tau)$ is normalized to a probability mass function (pmf) $p_d(\tau)$ by calculating an amplitude A_d such that the sum of all probabilities over the range of $f = f_m \ldots \infty$ equals 1, which for a discrete function is done by summation:

$$A_d \sum_{f=f_m}^{\infty} e^{-\frac{f\Delta t}{\tau}} \Delta t = 1 \qquad \text{(Eq. A. S6a)}$$

This summation is a geometric series, so it can be calculated exactly using the relation:

$$\sum_{f=m}^{\infty} r^f = \frac{r^m}{1-r} \qquad \text{(Eq. A. S6b)}$$

where in this case $r = e^{-\frac{\Delta t}{\tau}}$. The amplitude A_d is then solved as:

$$A_d = \frac{1}{\left(\sum_{f=f_m}^{\infty} e^{-\frac{f\Delta t}{\tau}} \Delta t\right)} = \frac{1}{\Delta t}\left(1 - e^{-\frac{\Delta t}{\tau}}\right) e^{\frac{f_m \Delta t}{\tau}} \qquad \text{(Eq. A. S6c)}$$

Substituting A_d into P_d (Eq. A.S5) yields the pmf, p_d:

$$p_d(f, \tau) = \frac{1}{\Delta t}\left(1 - e^{-\frac{\Delta t}{\tau}}\right) e^{-\frac{\Delta t}{\tau}(f - f_m)} \quad \text{(Eq. A. S7)}$$

A.4.3 Derivation as a geometric distribution

Eq. A.S7 is in the form of a geometric distribution, which is the discrete version of the exponential distribution, sharing the memory-less property. The geometric distribution gives the probability of observing one 'success' (e.g. a coin landing on heads) after k trials (e.g. coin flips), when the probability of one successful trial is p_1. The probability mass function (the discrete equivalent of the pdf) of the geometric distribution is given by:

$$pmf_{geo} = p_1(1 - p_1)^k \quad \text{(Eq. A. S8)}$$

In the case of observing the duration of a fluorescence event with a camera, each frame may be considered one trial, and an event coming to an end within a frame may be considered a 'success' that occurs with probability, p_1. Eq. A.S4 above enables calculation of the probability that an event with a characteristic lifetime τ, will end during a frame of duration Δt, by integrating Eq. A.S4 from 0 to Δt yielding the probability, p_0:

$$p_0 = \left(1 - e^{\frac{-\Delta t}{\tau}}\right) \qquad \text{(Eq. A. S9)}$$

Using this probability of "success" for each trial in the geometric pmf (Eq. A.S8), a discrete distribution is obtained giving the probability that an event will be observed that lasts *f* frames

$$p_d(f,\tau) = \frac{1}{\Delta t}\left(1 - e^{-\frac{\Delta t}{\tau}}\right) e^{-\frac{\Delta t}{\tau}(f)} \qquad \text{(Eq. A. S10)}$$

where the pre-factor of $\frac{1}{\Delta t}$ is required for normalization in the conversion between from a pdf to a pmf. As mentioned before, requiring the total probability for experimentally observable frame numbers, f_i, to sum to 1.0 leads to normalizing Eq. A.S10 as in Eq. A.S7.

A.4.4 Discrete (camera) probability mass functions for dwell time distributions

Photon emission from a fluorophore increases linearly from an OFF state to an ON state. An event starting at time t_s is marked as starting in frame n_s when the number of photons go above some fractional threshold ϕ_s relative to the maximum ON intensity (Fig. S1). For a dwell time measured as $t_d = f\Delta t$, the event will end within frame $n_e = n_s + f$, marked by the number of photons going below threshold ϕ_e, defining the camera dwell time t_d as:

$$t_d = (n_e - n_s)\Delta t = f\Delta t \qquad \text{(Eq. A. S11)}$$

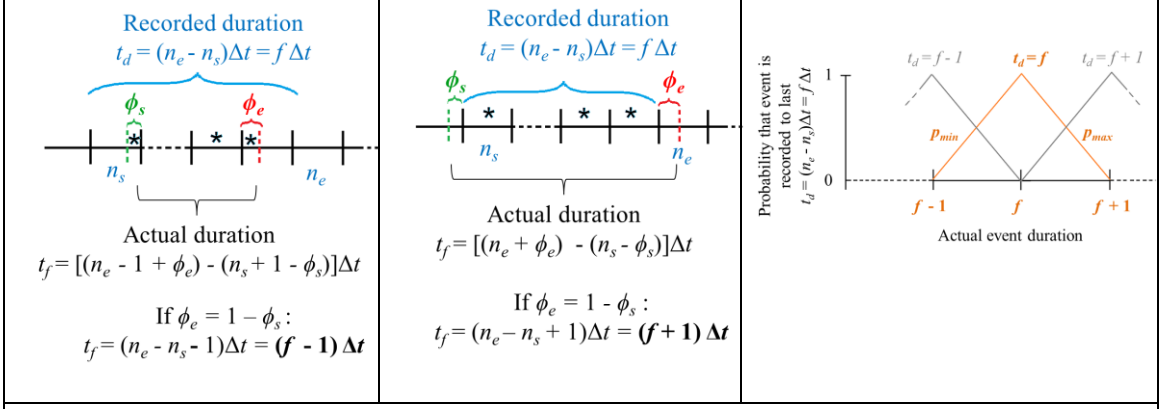

Figure A.S1. Camera frame binning. Minimum **(A)** and maximum **(B)** event durations that can be recorded as $t_d = (n_e - n_s)\Delta t = f\Delta t$. Stars indicate a frame being counted as part of the event. **(C)** Assuming $\phi_e = 1 - \phi_s$, the probability that an event is recorded to have duration $t_d = f\Delta t$ is non-zero in the range of actual event durations $f - 1$ to $f + 1$, with a maximum at f. Since the photon release rate is linear, this probability distribution forms a triangle in that range.

We are assuming that the thresholds are related such that $\phi_e = 1 - \phi_s$. Because an event has to last long enough to exceed the start threshold ϕ_s, events shorter than $t \leq \phi_s\Delta t$ are not detected. Start and end times of an event t_s and t_e, recorded in bins n_s and n_e, respectively, would be defined in the ranges:

$$t_s \in ((n_s - 1) - \phi_s)\Delta t \ \ldots \ (n_s - \phi_s)\Delta t \qquad \text{(Eq. A.S12)}$$

$$t_e \in ((n_e - 1) - \phi_s)\Delta t \ \ldots \ (n_e - \phi_s)\Delta t \qquad \text{(Eq. A.S13)}$$

From Eqs. S1 and S11-13, the dwell times t that can be recorded as $t_d = f\Delta t$ are defined over the range of $t_f \in (f - 1)\Delta t \ \ldots (f + 1)\Delta t$ (Fig. A.S1A, B). The probability of an event of dwell time t being measured as $f\Delta t$ is at a maximum when $t = f\Delta t$ and goes to zero as it approaches $(f - 1)\Delta t$ or $(f + 1)\Delta t$. This probability is related to the photon release rate, and is thus linear. The probability of dwell time t being measured as $f\Delta t$ is

then given by two, discontinuous linear pdfs, p_{min} and p_{max} (Figure A.S1C):

$$p_{min}(f,t) = \frac{1}{\Delta t^2}[t-(f-1)\Delta t] \qquad if\ \ (f-1)\Delta t \le t \le f\Delta t \qquad \text{(Eq. A.S14)}$$

$$p_{max}(f,t) = \frac{1}{\Delta t^2}[(f+1)\Delta t - t] \qquad if\ f\Delta t \le t \le (f+1)\Delta t \qquad \text{(Eq. A.S15)}$$

The probability of dwell time t, from a distribution defined by pdf $p(t,\tau)$ (Eq. A.S4), being measured by the camera as $t_d = f\Delta t$ can now be calculated from the integration of the joint probabilities $p_{min}\,(f,t)p(t,\tau)$ and $p_{max}\,(f,t)p(t,\tau)$ over their respective ranges (Eqs. A.S14 and A.S15). This integration can be greatly simplified by changing the range of p_{min} to be the same as that of p_{max} (i.e. $\Delta t \le t \le (f+1)$) (Fig. A.S1). Integrating the joint probabilities over this range gives an expression for the camera pmf, $p_d(f,\tau)$:

$$p_d = \Delta t \int_{f\Delta t}^{(f+1)\Delta t} (p_{max}\,(f,t) + p_{min}\,(f+1,t))p(t)dt \qquad \text{(Eq . A. S16)}$$

Noting that:

$$p_{max}\,(f,t) + p_{min}\,(f+1,t) = \frac{1}{\Delta t^2} \qquad \text{(Eq. A.S17)}$$

Eq. A.S16 is now transformed to the normalized camera pmf, $p_d(f,\tau)$:

$$p_d(f,\tau) = \frac{1}{\Delta t}\int_{f\Delta t}^{(f+1)\Delta t} \frac{1}{\tau} e^{-\frac{t}{\tau}}\,dt = \frac{1}{\Delta t}\left(1-e^{-\frac{\Delta t}{\tau}}\right)e^{-\frac{\Delta t}{\tau}(f-1)} \qquad \text{(Eq. A. S17)}$$

which is the same as pmf p_d in Eq. A.S7 for f_m = 1. Although this expression is independent of the threshold parameter ϕ_s, it does not fully address the missing dwell times $t<\phi_s\Delta t$ described above. Nonetheless, this expression accurately calculates τ for $f_m \ge 2$, but leads to a small error in the calculation of τ when f_m =1 (see Fig A.S3), as will be discussed further below.

A.4.5 Direct solution of τ for the 1st order discrete pmf, p_d

The direct solution of τ for the continuous function p(t,τ) (Eq. A.S4) is derived through the maximum likelihood optimization and has been shown to be:

$$\tau = t_{av} - t_m \qquad \text{(Eq. A. S19)}$$

where $t_{av} = \frac{\sum t}{N}$. The same can be done for the camera pmf $p_d(f,\tau)$ (Eq. A.S7) through its own likelihood function, which is the joint probability of all probabilities p_d for each camera dwell time $t_d = f\Delta t$:

$$L = \prod_{i=1}^{N} \frac{1}{\Delta t}\left(1 - e^{-\frac{\Delta t}{\tau}}\right) e^{-\frac{\Delta t}{\tau}(f_i - f_m)} \quad \text{(Eq. A. S20a)}$$

where the set of camera dwell times $f\Delta t$ is in the range $f = 1 \ldots N$. These probabilities tend to be very small, so the log likelihood, $LL = ln(L)$, is instead calculated. For the purpose of minimization, this function is made negative:

$$LL = -ln\left(\prod_{i=1}^{N} \frac{1}{\Delta t}\left(1 - e^{-\frac{\Delta t}{\tau}}\right) e^{-\frac{\Delta t}{\tau}(f_i - f_m)}\right)$$

$$= -\sum_{i=1}^{N} \ln\left(\frac{1}{\Delta t}\left(1 - e^{-\frac{\Delta t}{\tau}}\right) e^{-\frac{\Delta t}{\tau}(f_i - f_m)}\right) \quad \text{(Eq. A. S20b)}$$

The minimum is found for this by taking its derivative relative to τ and setting the resulting expression to zero:

$$\frac{d}{d\tau}\left(\sum_{i=1}^{N} \ln \frac{1}{\Delta t}\left(1 - e^{-\frac{\Delta t}{\tau}}\right) e^{-\frac{\Delta t}{\tau}(f_i - f_m)}\right) = 0 \qquad \text{(Eq. A. S20c)}$$

Solving this expression for τ leads to:

$$\tau = \frac{\Delta t}{\ln\left(1 + \frac{1}{f_{av} - f_m}\right)} \quad \text{(Eq. A. S21)}$$

where $f_{av} = \frac{\sum f}{N}$.

A.4.6 Addressing missing dwell times $t < \phi_s \Delta t$

As stated above, due to the threshold ϕ_s a certain number of dwell times will not be recorded, leading to a small error in calculation when f_m=1.

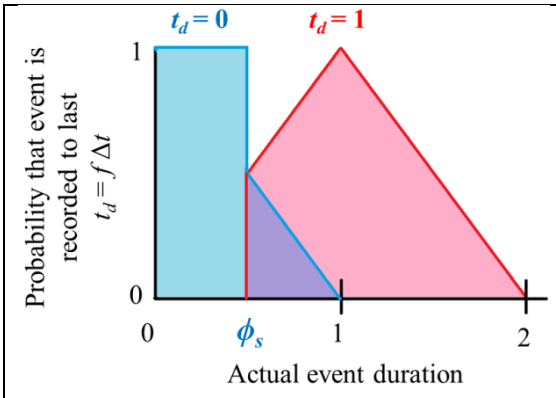

Figure A.S2: Probability functions for missing dwell times $t < \phi_s \Delta t$. Functions describing the probability of an event of dwell time t being measured as zero frames (i.e. undetected, blue) or one frame (red) are not simply triangles like those for two or more frames. Instead, they must be separately defined in a piece-wise function.

There is then a reduction in the number of dwell times recorded in the first frame (i.e. f=1) that must be considered when re-normalizing the probability mass function p_d (Eq. A.S7), done by calculating a new amplitude, A_d':

$$p_d'(f, \tau) = A_d' \frac{1}{\Delta t}\left(1 - e^{-\frac{\Delta t}{\tau}}\right) e^{-\frac{\Delta t}{\tau}(f-1)} \quad \text{(Eq. A. S22)}$$

where A_d', given in Eq. A.S6, is re-defined as:

$$A_d' = \frac{1}{\left(\sum_{f=1}^{\infty} \frac{1}{\Delta t}\left(1 - e^{-\frac{\Delta t}{\tau}}\right) e^{-\frac{\Delta t}{\tau}(f-1)}\,\Delta t\right) - \int_{\phi_s \Delta t}^{\Delta t} p_m(0, t)\, dt}$$

$$= \frac{1}{1 - \int_{\phi_s \Delta t}^{\Delta t} p_m(0, t) dt} \text{(Eq. A. S23)}$$

where $p_m(0,t)$ is the probability of an event not being recorded in frame f=1, meaning they are binned into f=0 (i.e., unrecorded) (Fig. S2). This probability is given by:

$$p_m(0,t) = p_{max}(0,t)\mathrm{p}(t,\tau) \qquad (\mathrm{Eq.\,A.\,S24})$$

where p_{max} and p (Eq. S15 and Eq. S4) are defined above. The digitizing effect of a camera recording events as an integer number of frames causes short events, $t < \phi_s \Delta t$, to not be detected (Fig. S2), meaning that the underlying pdf p (Eq. S4) is calculated using $t_m = \phi_s \Delta t$. Substituting this and p_{max} into Eqs. S23 and S24, the amplitude A_d' is then:

$$A_d' = \frac{1}{1 - \Delta t \int_{\phi_s \Delta t}^{\Delta t} \left(\frac{1}{\Delta t^2}[\Delta t - t]\right) \frac{1}{\tau} e^{-\frac{t - \phi_s \Delta t}{\tau}} dt} \qquad (\mathrm{Eq.\,A.\,S25})$$

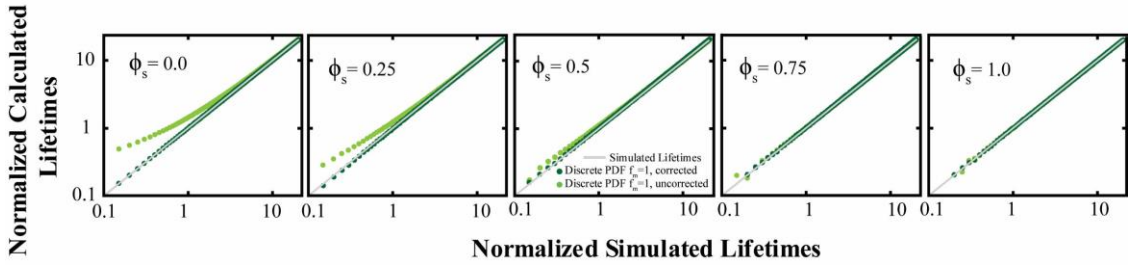

Figure A.S3. Corrections for errors in lifetime calculation when f_m=1. The calculation of τ using Eqs. A.S21 (uncorrected for f_m=1) andB. S27(corrected for f_m=1) on dwell times simulated over a range of t=0.2Δt-40Δt. Errors in calculation with S21 present themselves primarily for thresholds $\phi_s \leq 0.5$, which are well corrected by using Eq. B.S27 based on the re-normalized pmf, p_d'.

Evaluating Eq. A. S25 and substituting into p_d' gives:

$$p_d'(f,\tau) = \frac{1}{\Delta t} \frac{\left(1 - e^{-\frac{\Delta t}{\tau}}\right) e^{-\frac{\Delta t}{\tau}(f-1)}}{\phi_s + \frac{\tau}{\Delta t}\left(1 - e^{-\frac{(1-\phi_s)\Delta t}{\tau}}\right)} \qquad (\mathrm{Eq.\,A.\,S26})$$

Because of this equation's complexity, the direct solution needs to be calculated differently than for Eq. A.S7 described above (Eq. A.S21). This is done by noting that equation S26 reduces to Eq. S4 for $\phi_s = 0$ and Eq. S7 for $\phi_s = 1$, meaning that at these limits the direct solutions are given by Eqs. A.S19 and A.S21, respectively. It stands to reason that the direct solution for all ϕ_s could then be derived as a ϕ_s-dependent linear combination of these two solutions:

$$\tau = (1 - g(\phi_s)) \frac{\Delta t}{\ln\left(1 + \frac{1}{f_{av} - f_m}\right)} + g(\phi_s)(f_{av} - f_m)\Delta t \quad \text{(Eq. A. S27)}$$

A solution was found for this equation for $g(\phi_s) = (1-\phi_s)^2$. This solution was tested using simulated digitized dwell times (see below) over a range of $0.2\Delta t - 40\Delta t$ (Fig. S3), which are able to correct for the error introduced by calculating with p_d (Eq. A.S7) over the entire range of possible thresholds, $\phi_s = 0 \ldots 1$ (Fig. A.S3).

A.5 Higher order probability distribution functions

For systems containing more complex reactions schemes, the models consisting of linear combinations of exponential pdfs can be fit to the data. For example, if a transition between two biochemical states can occur through two independent and parallels pathways, each with characteristic lifetimes of τ_1 and τ_2, the observed durations of the starting state can be described by the sum of two single exponential pdfs, the most general form of which is given by:

$$p_2(t, \tau_1, \tau_2) = C \frac{1}{\tau_1} e^{-\frac{t}{\tau_1}} + (1 - C) \frac{1}{\tau_2} e^{-\frac{t}{\tau_2}} \qquad \text{(Eq. A. S28)}$$

Missing dwell times in a 2nd order distribution can be accounted for by re-normalizing $p_2(t,\tau_1,\tau_2)$ over the range of $t = t_m \ldots \infty$:

$$p_{2t} = \frac{\left(C\frac{1}{\tau_1}e^{-\frac{t}{\tau_1}} + (1-C)\frac{1}{\tau_2}e^{-\frac{t}{\tau_2}}\right)}{\int_{t_m}^{\infty} P_{2t}(t)\ dt} = \frac{\left(C\frac{1}{\tau_1}e^{-\frac{t}{\tau_1}} + (1-C)\frac{1}{\tau_2}e^{-\frac{t}{\tau_2}}\right)}{Ce^{-\frac{t_m}{\tau_1}} + (1-C)e^{-\frac{t_m}{\tau_2}}} \quad \text{(Eq. A. S29)}$$

Forming a 2nd order function for the camera pmf is done as a linear combination of two first order pmfs p_d (Eq. A.S7), similar to the operation performed for its continuous counterpart, p_2 (Eq. A.S28):

$$P_{d2} = A_{\mathrm{d1}}\frac{1}{\Delta t}\left(1-e^{-\frac{\Delta t}{\tau_1}}\right)e^{-\frac{\Delta t}{\tau_1}(f-1)} + A_{\mathrm{d2}}\frac{1}{\Delta t}\left(1-e^{-\frac{\Delta t}{\tau_2}}\right)e^{-\frac{\Delta t}{\tau_2}(f-1)} \quad \text{(Eq. A. S30)}$$

The relative fraction of events with average lifetimes τ_1 or τ_2 are represented by amplitudes A_{d1} and A_{d2}, which are related to the amplitudes (C and 1-C) of the underlying distribution, p_2. The difference in these amplitudes is directly related to the offset introduced by discretizing the lifetimes. This offset is the same as the offset between the amplitudes of the discrete (p_d, Eq. A.S7) and continuous (p, Eq. A.S4) single exponential pdfs. Therefore, the ratio of A_d to C is equal to that of the ratio of $\frac{1}{\tau}$ from p to $\frac{1}{\Delta t}\left(1-e^{-\frac{\Delta t}{\tau}}\right)$ from p_d, allowing the calculation of A_{d1} and A_{d2} in terms of the underlying continuous amplitude, C:

$$\frac{A_{\mathrm{d1}}}{C} = \frac{\left(1-e^{-\frac{\Delta t}{\tau_1}}\right)}{1/\tau_1} \quad ; \quad \frac{A_{\mathrm{d2}}}{(1-C)} = \frac{\left(1-e^{-\frac{\Delta t}{\tau_2}}\right)}{1/\tau_2} \quad \text{(Eq. A. S31)}$$

Substituting these into P_{d2} (Eq. A.S30):

$$P_{d2} = A_{\mathrm{d}}\frac{1}{\Delta t}\Bigg(C\tau_1\left(1-e^{-\frac{\Delta t}{\tau_1}}\right)^2 e^{-\frac{\Delta t}{\tau_1}(f-1)} + (1-C)\tau_2\left(1-e^{-\frac{\Delta t}{\tau_2}}\right)^2 e^{-\frac{\Delta t}{\tau_2}(f-1)}\Bigg) \quad \text{(Eq. A. S32)}$$

This can be normalized to a pmf, accounting for minimum frame length f_m, in the same manner as was done for the single exponential p_d (Eq. S7):

$$A_d = \frac{1}{\sum_{f=f_m}^{\infty} P_{d2}(f, \tau_1, \tau_2)\,\Delta t} \qquad \text{(Eq. A. S33)}$$

Substituting A_d into P_{d2} yields the 2nd order discrete exponential pdf:

$$p_{d2}(f, \tau_1, \tau_2)$$

$$= \frac{1}{\Delta t} \frac{C\tau_1\left(1 - e^{-\frac{\Delta t}{\tau_1}}\right)^2 e^{-\frac{\Delta t}{\tau_1}(f-1)} + (1-C)\tau_2\left(1 - e^{-\frac{\Delta t}{\tau_2}}\right)^2 e^{-\frac{\Delta t}{\tau_2}(f-1)}}{C\tau_1\left(1 - e^{-\frac{\Delta t}{\tau_1}}\right) e^{-\frac{\Delta t}{\tau_1}(f_{min}-1)} + (1-C)\tau_2\left(1 - e^{-\frac{\Delta t}{\tau_2}}\right) e^{-\frac{\Delta t}{\tau_2}(f_{min}-1)}} \qquad \text{(Eq. A. S34)}$$

References

Adio, S., Senyushkina, T., Peske, F., Fischer, N., Wintermeyer, W., and Rodnina, M. V (2015). Fluctuations between multiple EF-G-induced chimeric tRNA states during translocation on the ribosome. Nat. Commun. *6*, 7442.

Agirrezabala, X., Lei, J., Brunelle, J.L., Ortiz-Meoz, R.F., Green, R., and Frank, J. (2008). Visualization of the hybrid state of tRNA binding promoted by spontaneous ratcheting of the ribosome. Mol. Cell *32*, 190–197.

Allington, D.R., and Rivey, M.P. (2016). Quinupristin/dalfopristin: A therapeutic review. Clin. Ther. *23*, 24–44.

Ball, P. (2012). Nature's Color Tricks. Sci. Am. *306*, 74–79.

Ban, N., Nissen, P., Hansen, J., Moore, P.B., and Steitz, T.A. (2000). The complete atomic structure of the large ribosomal subunit at 2.4 A resolution. Science (80-.). *289*, 905–920.

Belardinelli, R., Sharma, H., Caliskan, N., Cunha, C.E., Peske, F., Wintermeyer, W., and Rodnina, M. V (2016). Choreography of molecular movements during ribosome progression along mRNA. Nat Struct Mol Biol *23*, 342–348.

Bethe, H.A. (1944). Theory of Diffraction by Small Holes. Phys. Rev. *66*, 163–182.

Betzig, E., and Chichester, R.J. (1993). Single Molecules Observed by Near-Field Scanning Optical Microscopy. Science (80-.). *262*, 1422–1425.

Bevington, P.R., and Robinson, D.K. (2002). Data Reduction and Error Analysis for the Physical Sciences (New York: McGraw-Hill).

Blanchard, S.C., Kim, H.D., Gonzalez, R.L., Puglisi, J.D., and Chu, S. (2004). tRNA dynamics on the ribosome during translation. Proc. Natl. Acad. Sci. U. S. A. *101*, 12893–12898.

Bordeira-Carriço, R., Pêgo, A.P., Santos, M., and Oliveira, C. (2012). Cancer syndromes

and therapy by stop-codon readthrough. Trends Mol. Med. *18*, 667–678.
Borovinskaya, M.A. (2007). Structural basis for aminoglycoside inhibition of bacterial ribosome recycling. Nat. Struct. Mol. Biol. *14*, 727–732.
Brierley, I. (1995). Review article Ribosomal frameshifting on viral RNAs. J. Gen. Virol. *76*, 1885–1892.
Brilot, A.F., Korostelev, A.A., Ermolenko, D.N., and Grigorieff, N. (2013). Structure of the ribosome with elongation factor G trapped in the pretranslocation state. Proc. Natl. Acad. Sci. *110*, 20994–20999.
Brochon, J.C. (1994). No Title. Methods Enzymol. *240*, 262–311.
Carter, A.P. (2001). Crystal structure of an initiation factor bound to the 30S ribosomal subunit. Science (80-.). *291*, 498–501.
Chen, C., Stevens, B., Kaur, J., Cabral, D., Liu, H., Wang, Y., Zhang, H., Rosenblum, G., Smilansky, Z., Goldman, Y.E., et al. (2011). Single-molecule fluorescence measurements of ribosomal translocation dynamics. Mol. Cell *42*, 367–377.
Chen, C., Greenberg, M.J., Laakso, J.M., Ostap, E.M., Goldman, Y.E., and Shuman, H. (2012). Kinetic schemes for post-synchronized single molecule dynamics. Biophys. J. *102*, L23-5.
Chen, C., Cui, X., Beausang, J.F., Zhang, H., Farrell, I., Cooperman, B.S., and Goldman, Y.E. (2016). Elongation factor G initiates translocation through a power stroke. Proc. Natl. Acad. Sci. *113*, 7515–7520.
Chen, J., Petrov, A., Tsai, A., O'Leary, S.E., and Puglisi, J.D. (2013). Coordinated conformational and compositional dynamics drive ribosome translocation. Nat Struct Mol Biol *20*, 718–727.
Colquhoun, D., and Hawkes, A.G. (2009). The Principles of the Stochastic Interpretation of Ion-Channel Mechanisms. In Single Channel Recording, B. Sakmann, and E. Neher, eds. (New York: Springer), pp. 397–479.
Connell, S.R., Topf, M., Qin, Y., Wilson, D.N., Mielke, T., Fucini, P., Nierhaus, K.H., and Spahn, C.M.T. (2008). A new tRNA intermediate revealed on the ribosome during EF4-mediated back-translocation. Nat Struct Mol Biol *15*, 910–915.
Copley, S.D., Smith, E., and Morowitz, H.J. (2007). The origin of the RNA world: Co-evolution of genes and metabolism. Bioorg. Chem. *35*, 430–443.
Cornish, P. V, Ermolenko, D.N., Staple, D.W., Hoang, L., Hickerson, R.P., Noller, H.F., and Ha, T. (2009a). Following movement of the L1 stalk between three functional states in single ribosomes. Proc. Natl. Acad. Sci. *106*, 2571–2576.
Cornish, P. V., Ermolenko, D.N., Noller, H.F., and Ha, T. (2009b). Spontaneous Intersubunit Rotation in Single Ribosomes. Mol. Cell *30*, 578–588.
Craighead, J.M.M.-M. and A.J.T. and K.T.S. and B.A.B. and H.G. (2007). Cell investigation of nanostructures: zero-mode waveguides for plasma membrane studies with single molecule resolution. Nanotechnology *18*, 195101.
Crick, F.H.C. (1968). The origin of the genetic code. J. Mol. Biol. *38*, 367–379.
Crick, F.H.C., and Watson, J.D. (1954). The Complementary Structure of Deoxyribonucleic Acid. Proc. R. Soc. London. Ser. A. Math. Phys. Sci. *223*, 80 LP-96.
Crick, F.H.C., Barnett, L., Brenner, S., and Watts-Tobin, R. (1961). General nature of the genetic code for proteins. Nature *192*, 1227–1232.
Cukras, A.R., Southworth, D.R., Brunelle, J.L., Culver, G.M., and Green, R. (2003). Ribosomal Proteins S12 and S13 Function as Control Elements for Translocation of the

mRNA:tRNA Complex. Mol. Cell *12*, 321–328.
Degiron, A., Lezec, H.J., Yamamoto, N., and Ebbesen, T.W. (2004). Optical transmission properties of a single subwavelength aperture in a real metal. Opt. Commun. *239*, 61–66.
Demeshkina, N., Jenner, L., Westhof, E., Yusupov, M., and Yusupova, G. (2012). A new understanding of the decoding principle on the ribosome. Nature *484*, 256–259.
Denk, W., Strickler, J.H., and Webb, W.W. (1990). Two-Photon Laser Scanning Fluorescence Microscopy. Science (80-.). *248*, 73–76.
Diaconu, M., Kothe, U., Schlünzen, F., Fischer, N., Harms, J.M., Tonevitsky, A.G., Stark, H., Rodnina, M. V, and Wahl, M.C. (2015). Structural Basis for the Function of the Ribosomal L7/12 Stalk in Factor Binding and GTPase Activation. Cell *121*, 991–1004.
Dorner, S., Brunelle, J.L., Sharma, D., and Green, R. (2006). The hybrid state of tRNA binding is an authentic translation elongation intermediate. Nat Struct Mol Biol *13*, 234–241.
Du, L., Damoiseaux, R., Nahas, S., Gao, K., Hu, H., Pollard, J.M., Goldstine, J., Jung, M.E., Henning, S.M., Bertoni, C., et al. (2009). Nonaminoglycoside compounds induce readthrough of nonsense mutations. J. Exp. Med. *206*, 2285 LP-2297.
Du, L., Jung, M.E., Damoiseaux, R., Completo, G., Fike, F., Ku, J.-M., Nahas, S., Piao, C., Hu, H., and Gatti, R.A. (2013). A New Series of Small Molecular Weight Compounds Induce Read Through of All Three Types of Nonsense Mutations in the ATM Gene. Mol. Ther. *21*, 1653–1660.
Ermolenko, D.N., Spiegel, P.C., Majumdar, Z.K., Hickerson, R.P., Clegg, R.M., and Noller, H.F. (2007). The antibiotic viomycin traps the ribosome in an intermediate state of translocation. Nat. Struct. Mol. Biol. *14*, 493–497.
Farabaugh, P.J. (1996). Programmed Translational Frameshifting. *60*, 103–134.
Fei, J., Kosuri, P., MacDougall, D.D., and Gonzalez, R.L. (2008). Coupling of ribosomal L1 stalk and tRNA dynamics during translation elongation. Mol. Cell *30*, 348–359.
Fei, J., Bronson, J.E., Hofman, J.M., Srinivas, R.L., Wiggins, C.H., and Gonzalez, R.L. (2009). Allosteric collaboration between elongation factor G and the ribosomal L1 stalk directs tRNA movements during translation. Proc. Natl. Acad. Sci. U. S. A. *106*, 15702–15707.
Fei, J., Richard, A.C., Bronson, J.E., and Gonzalez, R.L. (2011). Transfer RNA-mediated regulation of ribosome dynamics during protein synthesis. Nat. Struct. Mol. Biol. *18*, 1043–1051.
Fischer, N., Konevega, A.L., Wintermeyer, W., Rodnina, M. V, and Stark, H. (2010). Ribosome dynamics and tRNA movement by time-resolved electron cryomicroscopy. Nature *466*, 329–333.
Foquet, M., Samiee, K.T., Kong, X., Chauduri, B.P., and Lundquist, P.M. (2008). No Title. J. Appl. Phys. *103*, 34301.
Fore, S., Yuen, Y., Hesselink, L., and Huser, T. (2007). Pulsed-Interleaved Excitation FRET Measurements on Single Duplex DNA Molecules Inside C-Shaped Nanoapertures. Nano Lett. *7*, 1749–1756.
Frank, J., and Agrawal, R.K. (2000). A ratchet-like inter-subunit reorganization of the ribosome during translocation. Nature *406*, 318–322.
Frank, J., and Gonzalez, R.L. (2010). Structure and Dynamics of a Processive Brownian Motor: The Translating Ribosome. Annu. Rev. Biochem. *79*, 381–412.
Fraser, C.S., and Doudna, J.A. (2007). Structural and mechanistic insights into hepatitis C

viral translation initiation. Nat Rev Micro *5*, 29–38.
Fredrick, K., and Noller, H.F. (2003). Catalysis of Ribosomal Translocation by Sparsomycin. Sci. *300*, 1159–1162.
Gao, Y.-G., Selmer, M., Dunham, C.M., Weixlbaumer, A., Kelley, A.C., and Ramakrishnan, V. (2009). The Structure of the Ribosome with Elongation Factor G Trapped in the Posttranslocational State. Sci. *326*, 694–699.
Gavrilova, L.P., and Spirin, A.S. (1971). Stimulation of "non-enzymic" translocation in ribosomes by p-chloromercuribenzoate. FEBS Lett. *17*, 324–326.
Gavrilova, L.P., Kostiashkina, O.E., Koteliansky, V.E., Rutkevitch, N.M., and Spirin, A.S. (1976). Factor-free ("Non-enzymic") and factor-dependent systems of translation of polyuridylic acid by Escherichia coli ribosomes. J. Mol. Biol. *101*, 537–552.
Geggier, P., Dave, R., Feldman, M.B., Terry, D.S., Altman, R.B., Munro, J.B., and Blanchard, S.C. (2010). Conformational sampling of aminoacyl-tRNA during selection on the bacterial ribosome. J. Mol. Biol. *399*, 576–595.
Genet, C., and Ebbesen, T.W. (2007). Light in tiny holes. Nature *445*, 39–46.
Gilbert, W. (1986). Origin of life: The RNA world. Nature *319*, 618.
Gonzalez-Hilarion, S., Beghyn, T., Jia, J., Debreuck, N., Berte, G., Mamchaoui, K., Mouly, V., Gruenert, D.C., Déprez, B., and Lejeune, F. (2012). Rescue of nonsense mutations by amlexanox in human cells. Orphanet J. Rare Dis. *7*, 1–14.
Goode, B.L., and Eck, M.J. (2007). Mechanism and Function of Formins in the Control of Actin Assembly. Annu. Rev. Biochem. *76*, 593–627.
Griffiths, D. (2012). Introduction to Electrodynamics (Pearson).
Guerrier-Takada, C., Gardiner, K., Marsh, T., Pace, N., and Altman, S. (1983). The RNA moiety of ribonuclease P is the catalytic subunit of the enzyme. Cell *35*, 849–857.
Guttfreund, H. (1995). Kinetics for the life sciences: receptors, transmitters, and catalysts (Cambridge: Cambridge University Press).
Ha, T., Ting, A.Y., Liang, J., Caldwell, W.B., Deniz, A.A., Chemla, D.S., Schultz, P.G., and Weiss, S. (1999). Single-molecule fluorescence spectroscopy of enzyme conformational dynamics and cleavage mechanism. Proc. Natl. Acad. Sci. U. S. A. *96*, 893–898.
Halder, G. (2014). Introduction to Chemical Engineering Thermodynamics (Delhi: PHI Learning Private Limited).
Harms, J. (2001). High resolution structure of the large ribosomal subunit from a mesophilic eubacterium. Cell *107*, 679–688.
Hell, S.W., and Wichmann, J. (1994). Breaking the diffraction resolution limit by stimulated-emission-depletion fluorescence microscopy. Opt. Lett. *19*, 780–782.
Hirashima, A., and Kaji, A. (1973). Role of elongation factor G and a protein factor on the release of ribosomes from messenger ribonucleic acid. J. Biol. Chem. *248*, 7580–7587.
Holtkamp, W., Cunha, C.E., Peske, F., Konevega, A.L., Wintermeyer, W., and Rodnina, M. V (2014). GTP hydrolysis by EF-G synchronizes tRNA movement on small and large ribosomal subunits. EMBO J. *33*, 1073 LP-1085.
Houston, W., and Moore, G. (1928). Transmission and Reflection of Gold and Silver Films. J. Opt. Soc. Am. *16*, 174.
Ibba, M., and Söll, D. (2000). Aminoacyl-tRNA Synthesis. Annu. Rev. Biochem. *69*, 617–650.

Itoh, Y., Sekine, S., Suetsugu, S., and Yokoyama, S. (2013). Tertiary structure of bacterial selenocysteine tRNA. Nucleic Acids Res. *41*, 6729–6738.
Jackson, J.D. (1999). Classical Electrodynamics (New York, NY, USA: John Wiley & Sons).
Jahn, M., Rogers, M.J., and Soll, D. (1991). Anticodon and acceptor stem nucleotides in tRNAGln are major recognition elements for E. coli glutaminyl-tRNA synthetase. Nature *352*, 258–260.
Jenner, L., Demeshkina, N., Yusupova, G., and Yusupov, M. (2010). Structural rearrangements of the ribosome at the tRNA proofreading step. Nat Struct Mol Biol *17*, 1072–1078.
Julián, P., Konevega, A.L., Scheres, S.H.W., Lázaro, M., Gil, D., Wintermeyer, W., Rodnina, M. V, and Valle, M. (2008). Structure of ratcheted ribosomes with tRNAs in hybrid states. Proc. Natl. Acad. Sci. *105*, 16924–16927.
Kaur, J., Raj, M., and Cooperman, B.S. (2011). Fluorescent labeling of tRNA dihydrouridine residues : Mechanism and distribution. 1393–1400.
Keeling, K.M., Xue, X., Gunn, G., and Bedwell, D.M. (2014). Therapeutics Based on Stop Codon Readthrough. Annu. Rev. Genomics Hum. Genet. *15*, 371–394.
Kim, H.D., Puglisi, J.D., and Chu, S. (2007). Fluctuations of Transfer RNAs between Classical and Hybrid States. Biophys. J. *93*, 3575–3582.
Kinz-Thompson, C.D., Palma, M., Pulukkunat, D.K., Chenet, D., Hone, J., Wind, S.J., and Gonzalez, R.L. (2013). Robustly Passivated, Gold Nanoaperture Arrays for Single-Molecule Fluorescence Microscopy. ACS Nano *7*, 8158–8166.
Korlach, J., Marks, P.J., Cicero, R.L., Gray, J.J., Murphy, D.L., Roitman, D.B., Pham, T.T., Otto, G.A., Foquet, M., and Turner, S.W. (2008). Selective aluminum passivation for targeted immobilization of single DNA polymerase molecules in zero-mode waveguide nanostructures. Proc. Natl. Acad. Sci. U. S. A. *105*, 1176–1181.
Korostelev, A. (2008). Crystal structure of a translation termination complex formed with release factor RF2. Proc. Natl Acad. Sci. USA *105*, 19684–19689.
Kothe, U., Wieden, H.-J., Mohr, D., and Rodnina, M. V. (2004). Interaction of Helix D of Elongation Factor Tu with Helices 4 and 5 of Protein L7/12 on the Ribosome. J. Mol. Biol. *336*, 1011–1021.
Kruger, K., Grabowski, P.J., Zaug, A.J., Sands, J., Gottschling, D.E., and Cech, T.R. (1982). Self-splicing RNA: Autoexcision and autocyclization of the ribosomal RNA intervening sequence of tetrahymena. Cell *31*, 147–157.
Lathi, B.P. (2004). Linear Signals and Systems (Oxford University Press).
Laurberg, M. (2008). Structural basis for translation termination on the 70S ribosome. Nature *454*, 852–857.
Leutenegger, M., Gösch, M., Perentes, A., Hoffmann, P., Martin, O.J.F., and Lasser, T. (2006). Confining the sampling volume for Fluorescence Correlation Spectroscopy using a sub-wavelength sized aperture. Opt. Express *14*, 956–969.
Levene, M.J., Korlach, J., Turner, S.W., Foquet, M., Craighead, H.G., and Webb, W.W. (2003). Zero-Mode Waveguides for Single-Molecule Analysis at High Concentrations. Science (80-.). *299*, 682–686.
Liao, D., Galajda, P., Riehn, R., Ilic, R., and Puchalla, J.L. (2008). No Title. Opt. Express *16*, 10077.
Lin, J., Gagnon, M.G., Bulkley, D., and Steitz, T.A. (2015). Conformational Changes of

Elongation Factor G on the Ribosome during tRNA Translocation. Cell *160*, 219–227.
Liu, T., Kaplan, A., Alexander, L., Yan, S., Wen, J.-D., Lancaster, L., Wickersham, C.E., Fredrick, K., Noller, H., Tinoco, I., et al. (2014). Direct measurement of the mechanical work during translocation by the ribosome. Elife *3*.
Loudon, J.A. (2013). Ataluren-time for a "no–nonsense" approach to haematological malignancies. Hematol. Leuk. *1*.
MacBeath, G., and Schreiber, S.L. (2000). No Title. Science (80-.). *289*, 1760.
Mazzei, T., Mini, E., Novelli, A., and Periti, P. (1993). Chemistry and mode of action of macrolides. J. Antimicrob. Chemother. *31*, 1–9.
McCann, J.J., Choi, U.B., Zheng, L., Weninger, K., and Bowen, M.E. (2010). Optimizing Methods to Recover Absolute FRET Efficiency from Immobilized Single Molecules. Biophys. J. *99*, 961–970.
McCloskey, J.A., and Nishimura, S. (1977). Modified nucleosides in transfer RNA. Acc. Chem. Res. *10*, 403–410.
McKinney, S.A., Joo, C., and Ha, T. (2006). Analysis of Single-Molecule FRET Trajectories Using Hidden Markov Modeling. Biophys. J. *91*, 1941–1951.
Mingeot-Leclercq, M.-P., Glupczynski, Y., and Tulkens, P.M. (1999). Aminoglycosides: Activity and Resistance. Antimicrob. Agents Chemother. *43*, 727–737.
Miyaki, M., Iijima, T., Yasuno, M., Kita, Y., Hishima, T., Kuroki, T., and Mori, T. (2002). High incidence of protein-truncating mutations of the p53 gene in liver metastases of colorectal carcinomas. Oncogene *21*, 6689–6693.
Moazed, D., and Noller, H.F. (1989). Intermediate states in the movement of transfer RNA in the ribosome. Nature *342*, 142–148.
Moran-Mirabal, J.M., and Craighead, H.G. (2008). Zero-mode waveguides: sub-wavelength nanostructures for single molecule studies at high concentrations. Methods *46*, 11–17.
Munro, J.B., Altman, R.B., O'Connor, N., and Blanchard, S.C. (2007a). Identification of two distinct hybrid state intermediates on the ribosome. Mol. Cell *25*, 505–517.
Munro, J.B., Altman, R.B., O/'Connor, N., and Blanchard, S.C. (2007b). Identification of two distinct hybrid state intermediates on the ribosome. Mol. Cell *25*, 505–517.
Munro, J.B., Altman, R.B., Tung, C.-S., Sanbonmatsu, K.Y., and Blanchard, S.C. (2010a). A fast dynamic mode of the EF-G-bound ribosome. EMBO J. *29*, 770–781.
Munro, J.B., Altman, R.B., Tung, C.-S., Cate, J.H.D., Sanbonmatsu, K.Y., and Blanchard, S.C. (2010b). Spontaneous formation of the unlocked state of the ribosome is a multistep process. Proc. Natl. Acad. Sci. *107*, 709–714.
Neveu, M., Kim, H.-J., and Benner, S.A. (2013). The "Strong" RNA World Hypothesis: Fifty Years Old. Astrobiology *13*, 391–403.
Ning, W., Fei, J., and Gonzalez, R.L. (2014). The ribosome uses cooperative conformational changes to maximize and regulate the efficiency of translation. Proc. Natl. Acad. Sci. U. S. A. *111*, 12073–12078.
Nirenberg, M.W., and Matthaei, J.H. (1961). THE DEPENDENCE OF CELL- FREE PROTEIN SYNTHESIS IN E. COLI UPON NATURALLY OCCURRING OR SYNTHETIC POLYRIBONUCLEOTIDES. Proc. Natl. Acad. Sci. U. S. A. *47*, 1588–1602.
Oishi, N., Duscha, S., Boukari, H., Meyer, M., Xie, J., Wei, G., Schrepfer, T., Roschitzki, B., Boettger, E.C., and Schacht, J. (2015). XBP1 mitigates aminoglycoside-induced

endoplasmic reticulum stress and neuronal cell death. Cell Death Dis. *6*, e1763.
Orgel, L.E. (1968). Evolution of the genetic apparatus. J. Mol. Biol. *38*, 381–393.
Pace, N.R., and Marsh, T.L. (1985). Rna catalysis and the origin of life. Orig. Life Evol. Biosph. *16*, 97–116.
Palade, G.E. (1955). A SMALL PARTICULATE COMPONENT OF THE CYTOPLASM. J. Biophys. Biochem. Cytol. *1*, 59–68.
Pan, D., Kirillov, S. V, and Cooperman, B.S. (2007). Kinetically competent intermediates in the translocation step of protein synthesis. Mol. Cell *25*, 519–529.
Pan, D., Qin, H., and Cooperman, B.S. (2009). Synthesis and functional activity of tRNAs labeled with fluorescent hydrazides in the D-loop. RNA *15*, 346–354.
Pape, T., Wintermeyer, W., and Rodnina, M. V (1998). Complete kinetic mechanism of elongation factor Tu-dependent binding of aminoacyl-tRNA to the A site of the E. coli ribosome. EMBO J. *17*, 7490–7497.
Peltz, S.W., Morsy, M., Welch, E.M., and Jacobson, A. (2013). Ataluren as an Agent for Therapeutic Nonsense Suppression. Annu. Rev. Med. *64*, 407–425.
Peng, K., Zhang, M., Lu, A., Wong, N.-B., Zhang, R., and Lee, S.-T. (2007). Ordered silicon nanowire arrays via nanosphere lithography and metal-induced etching. Appl. Phys. Lett. *90*.
Perentes, A., and et al. (2005). Fabrication of arrays of sub-wavelength nano-apertures in an optically thick gold layer on glass slides for optical studies. Nanotechnology *16*, S273.
Pestka, S. (1969). Studies on the Formation of Transfer Ribonucleic Acid-Ribosome Complexes: VI. Oligopeptide synthesis and translocation on ribosomes in the presence and absence of soluble transfer factors. J. Biol. Chem. *244*, 1533–1539.
Plant, E.P., and Dinman, J.D. (2006). Comparative study of the effects of heptameric slippery site composition on -1 frameshifting among different eukaryotic systems. RNA *12*, 666–673.
Qin, H., Grigoriadou, C., and Cooperman, B.S. (2009). Interaction of IF2 with the Ribosomal GTPase-Associated Center during 70S Initiation Complex Formation. Biochemistry *48*, 4699–4706.
Ramrath, D.J.F., Lancaster, L., Sprink, T., Mielke, T., Loerke, J., Noller, H.F., and Spahn, C.M.T. (2013). Visualization of two transfer RNAs trapped in transit during elongation factor G-mediated translocation. Proc. Natl. Acad. Sci. *110*, 20964–20969.
Ratje, A.H., Loerke, J., Mikolajka, A., Brünner, M., Hildebrand, P.W., Starosta, A.L., Dönhöfer, A., Connell, S.R., Fucini, P., Mielke, T., et al. (2010). Head swivel on the ribosome facilitates translocation by means of intra-subunit tRNA hybrid sites. Nature *468*, 713–716.
Reece, J.B., and Campbell, N.A. (2011). Biology (Boston: Benjamin Cummings / Pearson).
Rieger, J. The glass transition temperature of polystyrene. J. Therm. Anal. *46*, 965–972.
Rigneault, H., Capoulade, J., Dintinger, J., Wenger, J., Bonod, N., Popov, E., Ebbesen, T.W., and Lenne, P.-F. (2005). Enhancement of Single-Molecule Fluorescence Detection in Subwavelength Apertures. Phys. Rev. Lett. *95*, 117401.
Roberts, R.B. (1958). Introduction to Microsomal Particles and Protein Synthesis (New York: Pergamon Press).
Robertson, M.P., and Joyce, G.F. (2012). The Origins of the RNA World. Cold Spring Harb. Perspect. Biol. *4*.

Root-Bernstein, M., and Root-Bernstein, R. (2015). The ribosome as a missing link in the evolution of life. J. Theor. Biol. *367*, 130–158.
Rosenblum, G., Chen, C., Kaur, J., Cui, X., Zhang, H., Asahara, H., Chong, S., Smilansky, Z., Goldman, Y.E., and Cooperman, B.S. (2013). Quantifying elongation rhythm during full-length protein synthesis. J. Am. Chem. Soc. *135*, 11322–11329.
Roy, R., Hohng, S., and Ha, T. (2008). A practical guide to single-molecule FRET. Nat Meth *5*, 507–516.
Samiee, K.T., Foquet, M., Guo, L., Cox, E.C., and Craighead, H.G. (2005). λ-Repressor Oligomerization Kinetics at High Concentrations Using Fluorescence Correlation Spectroscopy in Zero-Mode Waveguides. Biophys. J. *88*, 2145–2153.
Samiee, K.T., Moran-Mirabal, J.M., Cheung, Y.K., and Craighead, H.G. (2006). Zero mode waveguides for single-molecule spectroscopy on lipid membranes. Biophys. J. *90*, 3288–3299.
Savelsbergh, A., Katunin, V.I., Mohr, D., Peske, F., Rodnina, M. V, and Wintermeyer, W. (2003). An elongation factor G-induced ribosome rearrangement precedes tRNA-mRNA translocation. Mol. Cell *11*, 1517–1523.
Schluenzen, F., Tocilj, A., Zarivach, R., Harms, J., Gluehmann, M., Janell, D., Bashan, A., Bartels, H., Agmon, I., Franceschi, F., et al. (2000). Structure of Functionally Activated Small Ribosomal Subunit at 3.3 Å Resolution. Cell *102*, 615–623.
Schlunzen, F., Zarivach, R., Harms, J., Bashan, A., Tocilj, A., Albrecht, R., Yonath, A., and Franceschi, F. (2001). Structural basis for the interaction of antibiotics with the peptidyl transferase centre in eubacteria. Nature *413*, 814–821.
Schmeing, T.M., and Ramakrishnan, V. (2009). What recent ribosome structures have revealed about the mechanism of translation. Nature *461*, 1234–1242.
Schrödinger, E. (1943). What Is Life? the Physical Aspect of the Living Cell and Mind (Dublin).
Schuwirth, B.S., Borovinskaya, M. a, Hau, C.W., Zhang, W., Vila-Sanjurjo, A., Holton, J.M., and Cate, J.H.D. (2005). Structures of the bacterial ribosome at 3.5 A resolution. Science *310*, 827–834.
Selmer, M., Dunham, C.M., Murphy, F. V, Weixlbaumer, A., Petry, S., Kelley, A.C., Weir, J.R., and Ramakrishnan, V. (2006). Structure of the 70S ribosome complexed with mRNA and tRNA. Science *313*, 1935–1942.
Seo, H.-S., Abedin, S., Kamp, D., Wilson, D.N., Nierhaus, K.H., and Cooperman, B.S. (2006). EF-G-Dependent GTPase on the Ribosome. Conformational Change and Fusidic Acid Inhibition†. Biochemistry *45*, 2504–2514.
Shalev, M., and Baasov, T. (2014). When Proteins Start to Make Sense: Fine-tuning Aminoglycosides for PTC Suppression Therapy. Medchemcomm *5*, 1092–1105.
Sharma, A.K., and Chowdhury, D. (2011). Distribution of dwell times of a ribosome: effects of infidelity, kinetic proofreading and ribosome crowding. Phys. Biol. *8*, 26005.
Sharma, H., Adio, S., Senyushkina, T., Belardinelli, R., Peske, F., and Rodnina, M.V. (2016). Kinetics of Spontaneous and EF-G-Accelerated Rotation of Ribosomal Subunits. Cell Rep. *16*, 2187–2196.
Sharp, P.A. (1985). On the origin of RNA splicing and introns. Cell *42*, 397–400.
Shi, H., and Moore, P.B. (2000). The crystal structure of yeast phenylalanine tRNA at 1.93 A resolution: a classic structure revisited. RNA *6*, 1091–1105.
Sprinzl, M., and Cramer, F. (1979). No Title. Prog. Nucleic Acids Res. Mol. Biol. *22*.

Swaney, S.M., Aoki, H., Ganoza, M.C., and Shinabarger, D.L. (1998). The Oxazolidinone Linezolid Inhibits Initiation of Protein Synthesis in Bacteria. Antimicrob. Agents Chemother. *42*, 3251–3255.
Takahashi, S., Tsuji, K., Ueda, T., and Okahata, Y. (2012). Traveling Time of a Translating Ribosome along Messenger RNA Monitored Directly on a Quartz Crystal Microbalance. J. Am. Chem. Soc. *134*, 6793–6800.
Tinoco, I., and Gonzalez, R.L. (2011). Biological mechanisms, one molecule at a time. Genes Dev. *25*, 1205–1231.
Tourigny, D.S., Fernández, I.S., Kelley, A.C., and Ramakrishnan, V. (2013). Elongation Factor G Bound to the Ribosome in an Intermediate State of Translocation. Sci. *340*.
Townsend, M.L., Pound, M.W., and Drew, R.H. (2007). Tigecycline in the treatment of complicated intra-abdominal and complicated skin and skin structure infections. Ther. Clin. Risk Manag. *3*, 1059–1070.
Uemura, S., Aitken, C.E., Korlach, J., Flusberg, B.A., Turner, S.W., and Puglisi, J.D. (2010). Real-time tRNA transit on single translating ribosomes at codon resolution. Nature *464*, 1012–1017.
Underwood, K.A., Swartz, J.R., and Puglisi, J.D. (2005). Quantitative polysome analysis identifies limitations in bacterial cell-free protein synthesis. Biotechnol. Bioeng. *91*, 425–435.
Valle, M., Zavialov, A., Sengupta, J., Rawat, U., Ehrenberg, M., and Frank, J. (2003). Locking and Unlocking of Ribosomal Motions. Cell *114*, 123–134.
Verschoor, A., Frank, J., Wagenknecht, T., and Boublik, M. (1986). Computer-averaged views of the 70 S monosome from Escherichia coli. J. Mol. Biol. *187*, 581–590.
Voorhees, R.M., Weixlbaumer, A., Loakes, D., Kelley, A.C., and Ramakrishnan, V. (2009). Insights into substrate stabilization from snapshots of the peptidyl transferase center of the intact 70S ribosome. Nat. Struct. Mol. Biol. *16*, 528–533.
Vukusic, P., and Sambles, J.R. (2003). Photonic structures in biology. Nature *424*, 852–855.
Wang, C.L.C. and R.J.N. and C.E.R. and T.F. (2006). Fabrication of nanopillars by nanosphere lithography. Nanotechnology *17*, 1339.
Wang, B., Ho, J., Fei, J., Gonzalez, R.L., and Lin, Q. (2011). A Microfluidic Approach for Investigating the Temperature Dependence of Biomolecular Activity with Single-Molecule Resolution. Lab Chip *11*, 274–281.
Wang, L., Pulk, A., Wasserman, M.R., Feldman, M.B., Altman, R.B., Cate, J.H.D., and Blanchard, S.C. (2012). Allosteric control of the ribosome by small-molecule antibiotics. Nat. Struct. Mol. Biol. *19*, 957–963.
Wang, Y., Qin, H., Kudaravalli, R.D., Kirillov, S. V, Dempsey, G.T., Pan, D., Cooperman, B.S., and Goldman, Y.E. (2007). Single-molecule structural dynamics of EF-G--ribosome interaction during translocation. Biochemistry *46*, 10767–10775.
Wasserman, M.R., Alejo, J.L., Altman, R.B., and Blanchard, S.C. (2016). Multiperspective smFRET reveals rate-determining late intermediates of ribosomal translocation. Nat Struct Mol Biol *23*, 333–341.
Weisstein, E.W. (2002). CRC Concise Encyclopedia of Mathematics (Boca Raton: CRC Press).
Weixlbaumer, A. (2008). Insights into translational termination from the structure of RF2 bound to the ribosome. Science (80-.). *322*, 953–956.

Wenger, J., Gérard, D., Lenne, P.-F., Rigneault, H., and Dintinger, J. (2006). No Title. Opt. Express *14*, 12206.
Wimberly, B.T. (2000). Structure of the 30S ribosomal subunit. Nature *407*, 327–339.
Woese, C. (1967). The genetic code (New York: Harper and Row).
Woody, M.S., Lewis, J.H., Greenberg, M.J., Goldman, Y.E., and Ostap, E.M. (2016). MEMLET: An Easy-to-Use Tool for Data Fitting and Model Comparison Using Maximum-Likelihood Estimation. Biophys. J. *111*, 273–282.
Xie, X.S., and Dunn, R.C. (1994). Probing Single Molecule Dynamics. Science (80-.). *265*, 361–364.
Yildiz, A., Forkey, J.N., McKinney, S.A., Ha, T., Goldman, Y.E., and Selvin, P.R. (2003). Myosin V Walks Hand-Over-Hand: Single Fluorophore Imaging with 1.5-nm Localization. Science (80-.). *300*, 2061–2065.
Yusupov, M.M. (2001). Crystal structure of the ribosome at 5.5 A resolution. Science (80-.). *292*, 883–896.
Zavialov, A. V, Mora, L., Buckingham, R.H., and Ehrenberg, M. (2002). Release of peptide promoted by the GGQ motif of class 1 release factors regulates the GTPase activity of RF3. Mol. Cell *10*, 789–798.
Zhao, Y., Chen, D., Yue, H., Spiering, M.M., Zhao, C., Benkovic, S.J., and Huang, T.J. (2014). Dark-Field Illumination on Zero-Mode Waveguide/Microfluidic Hybrid Chip Reveals T4 Replisomal Protein Interactions. Nano Lett. *14*, 1952–1960.
Zhou, J., Lancaster, L., Donohue, J.P., and Noller, H.F. (2014). How the ribosome hands the A-site tRNA to the P site during EF-G–catalyzed translocation. Sci. *345*, 1188–1191.